AD_____

Award Number:  DAMD17-99-1-9022

TITLE:  Periscopic Spine Surgery

PRINCIPAL INVESTIGATOR:  Kevin R. Cleary, Ph.D.

CONTRACTING ORGANIZATION:  Georgetown University
                          Washington, DC  20057

REPORT DATE:  March 2005

TYPE OF REPORT:  Final

PREPARED FOR:  U.S. Army Medical Research and Materiel Command
               Fort Detrick, Maryland  21702-5012

DISTRIBUTION STATEMENT: Approved for Public Release;
                        Distribution Unlimited

20050621 075

# REPORT DOCUMENTATION PAGE

| 1. AGENCY USE ONLY (Leave blank) | 2. REPORT DATE | 3. REPORT TYPE AND DATES COVERED |
|---|---|---|
| | March 2005 | Final (15 Jan 99 - 1 Feb 05) |

**4. TITLE AND SUBTITLE**
Periscopic Spine Surgery

**5. FUNDING NUMBERS**
DAMD17-99-1-9022

**6. AUTHOR(S)**
Kevin R. Cleary, Ph.D.

**7. PERFORMING ORGANIZATION NAME(S) AND ADDRESS(ES)**
Georgetown University
Washington, DC 20057

**E-Mail:** cleary@georgetown.edu

**8. PERFORMING ORGANIZATION REPORT NUMBER**

**9. SPONSORING / MONITORING AGENCY NAME(S) AND ADDRESS(ES)**

U.S. Army Medical Research and Materiel Command
Fort Detrick, Maryland 21702-5012

**10. SPONSORING / MONITORING AGENCY REPORT NUMBER**

**11. SUPPLEMENTARY NOTES**

**12a. DISTRIBUTION / AVAILABILITY STATEMENT**
Approved for Public Release; Distribution Unlimited

**12b. DISTRIBUTION CODE**

**13. ABSTRACT (Maximum 200 Words)**

The Periscopic Spine Surgery project was envisioned to lay the ground work for developing the physician assist systems of the future. These systems will incorporate robotics, tracking, and visualization to improve the precision of instrument placement and manipulation in minimally invasive procedures. This project has enabled the Georgetown team to become a world leader in the emerging fields of computer aided surgery and medical robotics. Our goal will continue to be to develop systems to add the physician in these demanding minimally invasive procedures with the ultimate aim of improving patient care.
Key research accomplishments included:
1. Received FDA approval to conduct a clinical trial for robotically assisted spinal blocks and completed twenty patients
2. Completed a feasibility demonstration of robotically assisted lung biopsy using frame-grabbed CT fluoroscopy images and a respiratory motion phantom
3. Completed an initial set of approved animal studies demonstrating the feasibility of electromagnetic position sensing for image guidance in the interventional suite
4. Gathered skin motion data on four patients during CyberKnife stereotactic radiosurgery treatments under an IRB-approved protocol
5. Developed a respiratory motion simulator consisting of two 3 degree of freedom platforms to evaluate CyberKnife treatments which compensate for internal organ motion

**14. SUBJECT TERMS**
Minimally invasive procedures, technology development, medical robotics, electromagnetic tracking, stereotactic radiosurgery

**15. NUMBER OF PAGES**
91

**16. PRICE CODE**

| 17. SECURITY CLASSIFICATION OF REPORT | 18. SECURITY CLASSIFICATION OF THIS PAGE | 19. SECURITY CLASSIFICATION OF ABSTRACT | 20. LIMITATION OF ABSTRACT |
|---|---|---|---|
| Unclassified | Unclassified | Unclassified | Unlimited |

# Table of Contents

## Appendices (Copies of published papers)

# List of Figures

# 2 Introduction

This project is aimed at improving the state of the art of image-guided and minimally invasive procedures by developing a new generation of clinical techniques along with the computer-based hardware and software needed for their implementation. The focus of the project is to develop physician assist systems incorporating robotics, tracking, and visualization to improve the precision of instrument placement and manipulation in minimally invasive procedures. The project is led by the Imaging Sciences and Information Systems (ISIS) Center of the Department of Radiology at Georgetown University. Project collaborators include the Department of Radiation Medicine at Georgetown, the Urology Robotics Group at Johns Hopkins Medical Institutions, the NSF sponsored Engineering Research Center for Computer Integrated Surgical Systems and Technology at Johns Hopkins University, and the Engineering School at the Catholic University of America, as well as several commercial partners.

# 3 Report Body

This section describes the research accomplishments associated with each task in the statement of work. This is the final report and includes research performed from January 15, 1999 – February 1, 2005. Since annual reports have been provided every year and included detailed progress updates, this report will focus on the work done over the past year from February 1, 2004 to February 1, 2005 (although reference will also be made to previous work in some places). The award number is DAMD17-99-1-9022.

## 3.1 Task 1: Program Planning and Management

Throughout the award period, program planning and management focuses on maintaining project direction as well as developing strong partnerships with project collaborators. Project planning and review meetings are held monthly at the ISIS Center. In the 2004 calendar year major progress was made on several projects including fluoroscopy servoing for the needle driver robot, electromagnetic tracking of guidewires for image guidance, rehabilitation robotics, and three-dimensional visualization. We also organized an extremely successful workshop titled "OR2020: The Operating Room of the Future".

The group continues to be very active in presenting their work at national and international conferences. Dr. Cleary is now the co-chair for the "Image-guided Procedures, Visualization, and Display" track of the SPIE Medical Imaging meeting, which is held every February in San Diego. The group demonstrated several of their prototypes at the Computer Aided Radiology and Surgery Conference (CARS) in June 2004 in Chicago. Dr. Cleary is also currently organizing medical robotics workshops for the April 2005 IEEE Robotics and Automation Conference and the June 2005 CARS conference.

## 3.2 Task 2: Spinal Robotics

One of the key outcomes of this project has been the development of a needle driver robot in collaboration with the Urology Robotics Program at Johns Hopkins University (Dan Stoianovici, PhD). Precision placement of instruments such as needles could be enhanced by medical robotics and we have become an international leader in this area. As detailed in the last annual report, the initial clinical trial of 20 patients using the needle driver robot for spinal blocks was conducted at Georgetown University from August 2002 to December 2002. A picture of the robot is shown in Figure 1 and a picture of the first patient is shown in Figure 2. The clinical trial showed that is feasible to use a joystick controlled robot for nerve and facet blocks. Based on the success of this initial trial, we applied to the FDA to continue the clinical trial with an additional 80 patients. We have now received FDA approval for as well as approval from the Georgetown and Army IRB boards. We have completed a few new patients under this revised protocol, but have not yet gathered enough new data to report any more conclusions.
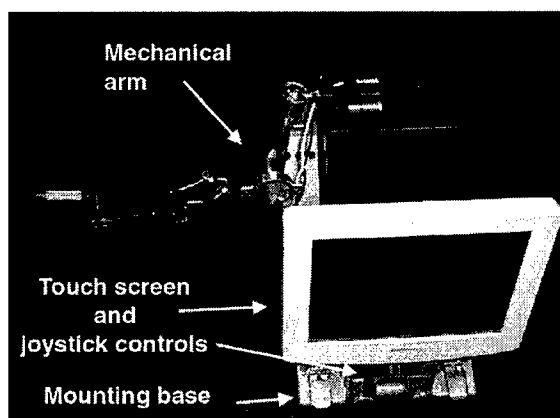


**Figure 1: Robotic device showing mechanical arm and joystick control**
(courtesy of Dan Stoianovici, PhD, Johns Hopkins Urology Robotics)
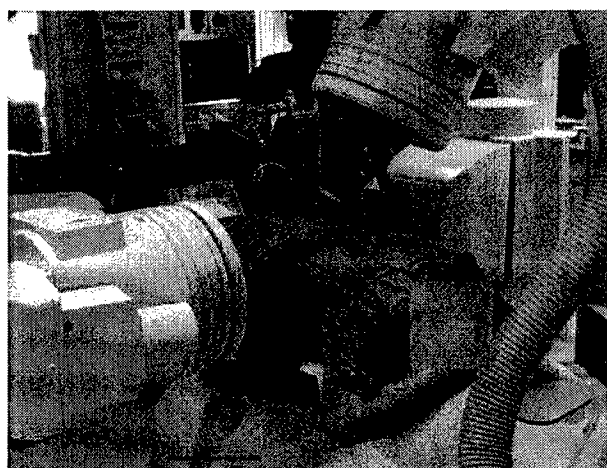


**Figure 2: Clinical trial of robotic device for nerve and facet blocks at Georgetown University (interventional radiologist is Vance Watson, MD)**

This work is also being continued through two additional tasks which will now be described:

Section 5.2.1: fluoroscopy servoing for needle alignment
Section 5.2.2: robotically assisted lung biopsy

## 3.2.1 Fluoroscopy Servoing for Needle Alignment

In the clinical trial described in Section 5.2, the first step in placing the needle using the robot is to align the needle toward the target to be reached. By capturing the fluoroscopy images on the computer and rapidly processing them, it is possible to automatically align the needle for the physician. This automatic needle alignment is a first step towards further automating the procedure and an initial step towards the completely automatic biopsy systems of the future. The alignment technique is "fluoroscopy servoing" and has been explored by just a few researchers.

Our recent work in this area is detailed in [Mihaescu 2005] and just a summary will be given here. The whole process consists of two phases: translation and alignment. The translation process will place the tip of the needle on the line of sight that passes through the target. The alignment stage will orient the needle until it is parallel to the line of sight between the anatomical target and the projection of the target on the fluoroscopic image. The positions of the needle tip in the image plane are found by segmenting the needle from the fluoroscopic images. A typical fluoroscopic image is presented in Figure 3, where the needle appears to overlap a section of the patient's spine.



| Figure 3. Fluoroscopic input image | Figure 4. Flow diagram of the segmentation method and needle tip position estimation |
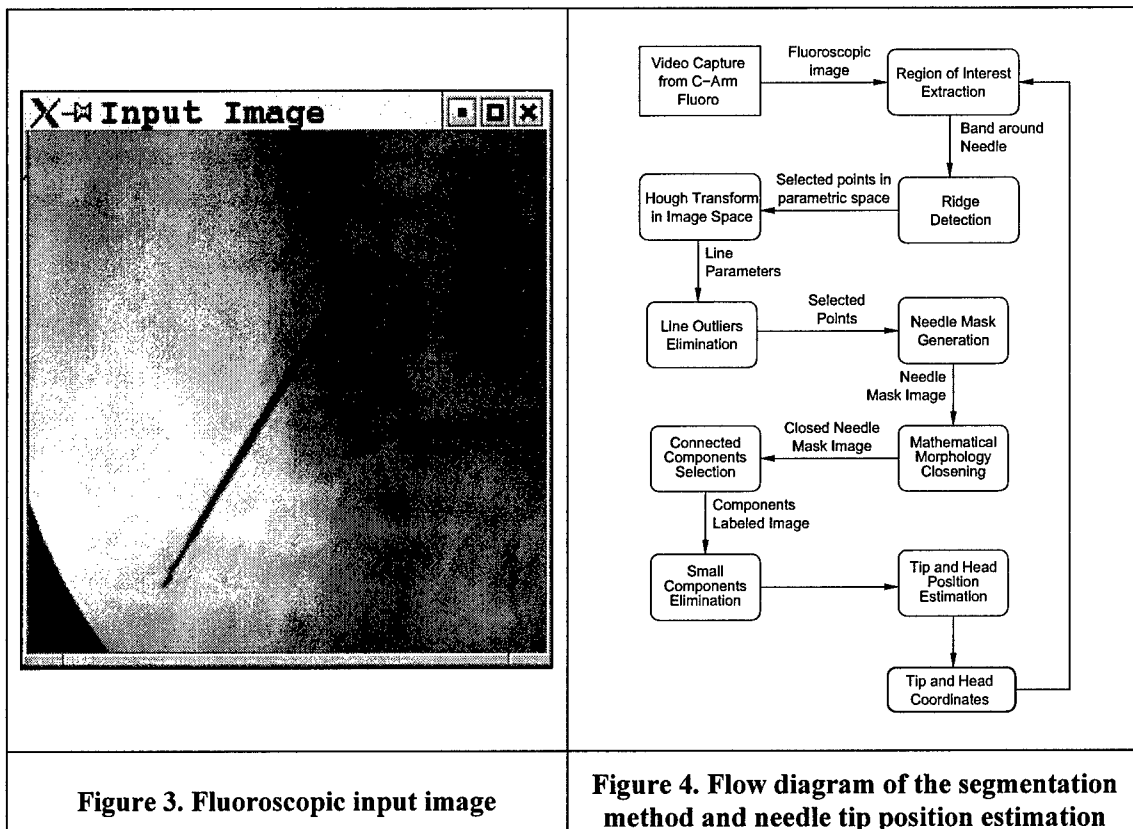
The process used for segmenting the needle is illustrated in Figure 4. The essential aspect of this segmentation process is the detection of intensity ridge points on the fluoroscopic image. For details please refer to the paper in the appendix [Mihaescu 2005].

## 3.2.2 Robotically Assisted Lung Biopsy

Based on our initial work in needle placement for spinal procedures using x-ray fluoroscopy, we expanded into needle placement for lung biopsy under CT fluoroscopy. This work has also been partially supported by an NCI/NIH grant.

The first phase of this project has been completed and a paper has been submitted to Academic Radiology [Cleary 2004]. The goal of this phase was to evaluate using a joystick-controlled robotic needle driver for lung biopsy in a phantom study.

A respiratory motion phantom incorporating cranial-caudal motion of a foam liver phantom was developed. Synthetic lesions of about 1.5 mm in diameter were created using an agar mix. CT fluoroscopy was used to visualize the motion of a lesion in and out of the scan plane. The phantom could be paused on demand for up to 30 seconds to simulate a breath hold. A joystick-controlled robotic needle driver was used by a radiologist experienced in lung biopsy to drive an 18 gauge needle on the scan plane toward the lesion. The experimental setup is shown in Figure 5.
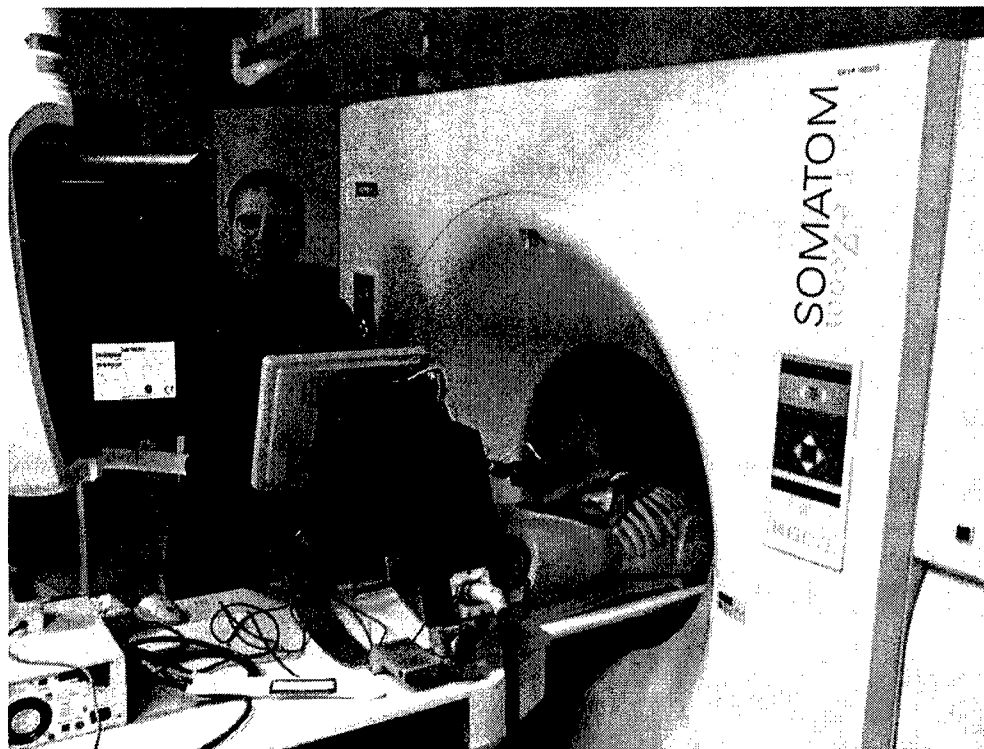


**Figure 5: Phantom study of robotically assisted lung biopsy under CT fluoroscopy at Georgetown University (interventional radiologist is Charles White, MD)**

The radiologist was able to hit the lesion on all 20 attempts. A CT image of the needle in the lesion is shown in Figure 6. The average time to drive the needle was 12.1 seconds with a standard deviation of 3.1 seconds. The average tube current-time product was 955 mAs with a standard deviation of 180 mAs. The average dose-length product was 92.5 mGycm with a standard deviation of 42 mGycm.

The conclusion was that a joystick-controlled robotic needle driver can be used to accurately target lesions in a respiring phantom under CT fluoroscopy. This technique may allow the radiologist to more precisely manipulate the needle with much less radiation exposure. Additional studies are planned to further automate this process and to investigate the role of robotic systems for lung biopsy in the clinical area.



**Figure 6: Axial CT image of needle in lung lesion**

## 3.3 Task 3: Liver Respiratory Motion Simulator and Internal Organ Tracking

The goal of this task is to investigate the use of electromagnetic tracking for precisely locating internal organs such as the liver during interventional procedures. This is an ongoing collaboration with Northern Digital (Waterloo, Canada) and Traxtal Technologies (Bellaire, Texas). Northern Digital has developed the AURORA™ electromagnetic tracking system, which enables instruments that are fitted with a sensing coil to be tracked and overlaid on an image of the anatomy. Our research group at Georgetown served as a beta test site and was one of the first research groups worldwide to receive this equipment. The system has recently been released as a commercial product as shown in Figure 7.
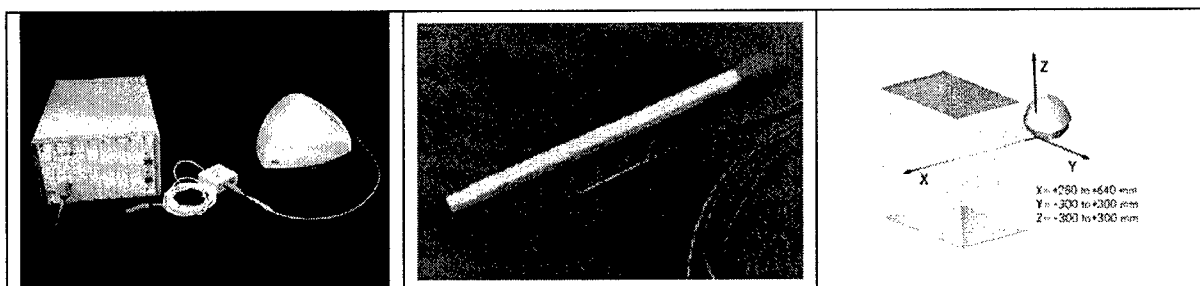
**Figure 7: AURORA™ sensors, electromagnetic tracking system components, and measurement volume**
The left picture shows (from left to right) the control unit, sensor interface device, and electromagnetic field generator. The middle picture shows the sensor coils along with the electrical wires protruding from the coil, compared to a match. The right picture shows the measurement volume in mm relative to the location of the field generator. (Photos courtesy of Northern Digital, Inc.)

As part of this research, we have developed an image-guided surgery system incorporating electromagnetic tracking. Figure 8 shows the tracking system as recently used in an approved swine study in the interventional suite. Electromagnetic tracking of instruments in the interventional suite enables image overlay of preoperative CT scans and provides multimodality guidance while decreasing x-ray dose. In the study described here, an electromagnetically tracked guidewire was manipulated in a swine model with co-display of CT and angiographic images [Wood 2004].
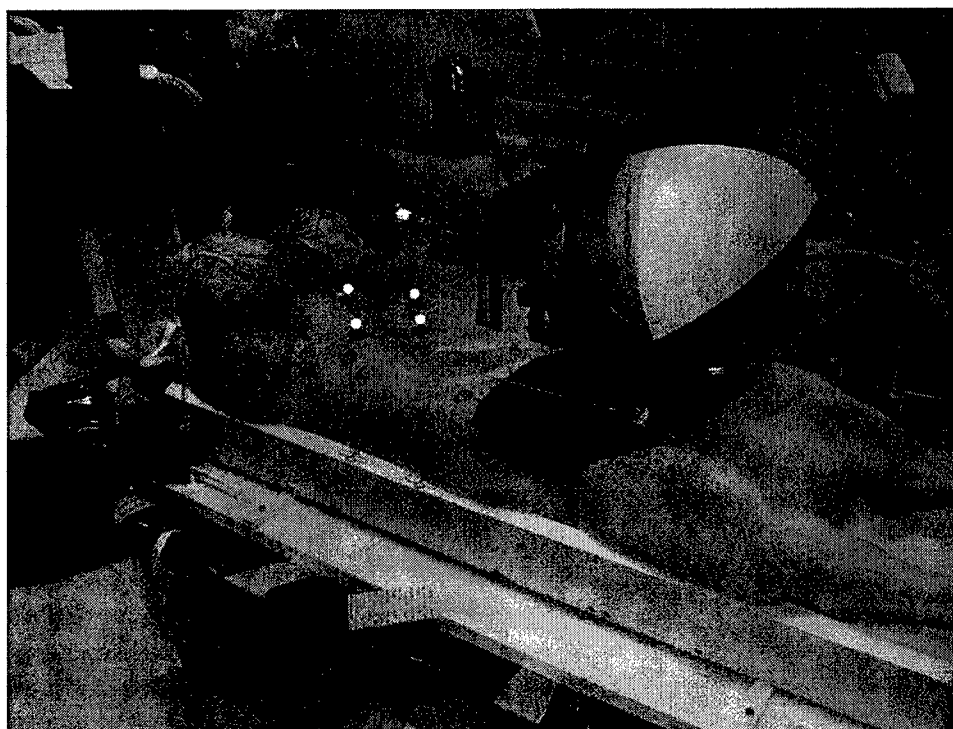


**Figure 8: Swine study in the interventional suite**

An enhanced CT scan of a swine chest and abdomen was obtained. A rigid body registration was carried out by identifying the points on the CT scan and in electromagnetic space. The guidewire was then initially moved in free air over the abdominal area of the swine to verify that the registration software was working and that is could be tracked.

The internal jugular vein and right carotid artery were percutaneously accessed using ultrasound guidance and modified Seldinger technique with a 21 gauge needle and an .018 inch guidewire. As the guidewire was advanced down the aorta, the corresponding axial CT scan was displayed simultaneously with the real-time angiographic x-ray image. The system provided good qualitative agreement in the opinion of the experienced interventional radiologist manipulating the guidewire. As the guidewire was advanced into the selected vessel, the image-guided system was able to actively track the guidewire and display axial, coronal, and sagittal CT scans at the same level, using the electromagnetically tracked sensor position to select the slice location. The resulting display is shown in Figure 9.
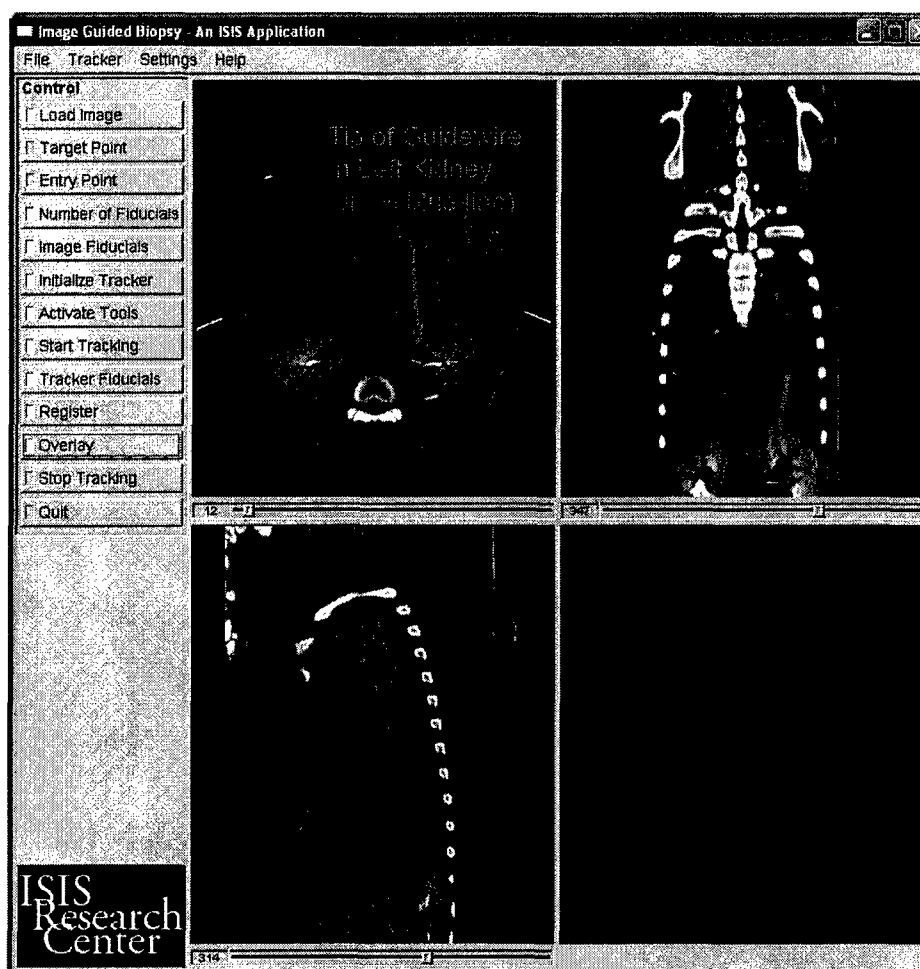


**Figure 9: Axial, sagittal, and coronal image overlay of electromagnetically tracked guidewire**

## 3.4 Task 4: Radiation Treatment (Stereotactic Radiosurgery)

Organs in the abdomen and thorax move and deform during respiration, and these changes place a severe limitation on the effectiveness of radiation medicine in the lungs, liver, and pancreas. Georgetown University Medical Center is an emerging leader in a new form of radiosurgery for these types of tumors. These treatments are enabled by two key technologies: (1) the Cyberknife, a precision radiosurgery machine based around a compact linac and a robotic positioning arm, and (2) Synchrony, a system for optically tracking respiratory motion and steering the radiation beam to follow a moving tumor. This research is being carried out in conjunction with the Radiation Medicine Department at Medstar Georgetown University Hospital.
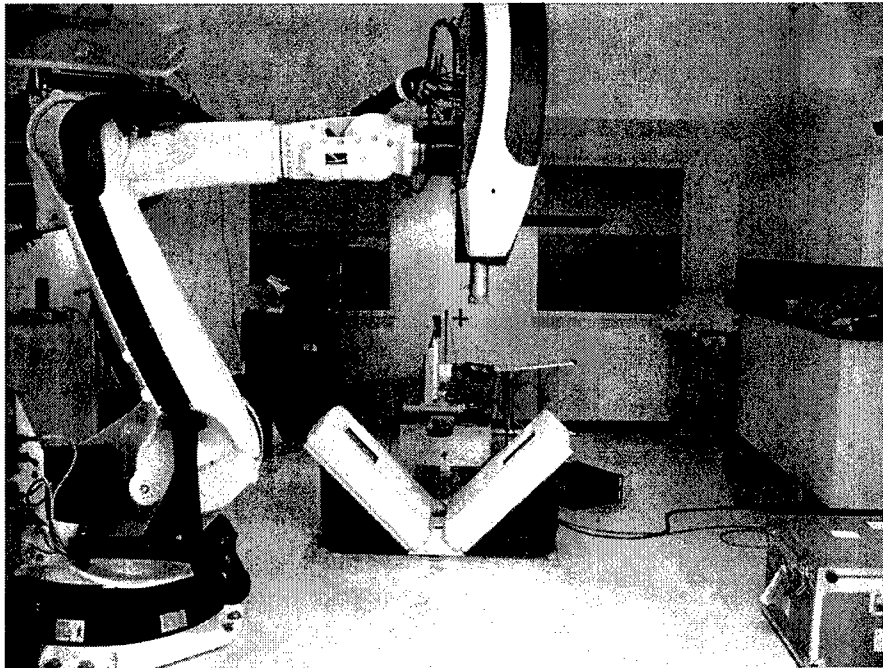


**Figure 10: Photograph of Cyberknife Stereotactic Radiosurgery System**
**(Accuray, Sunnyvale, CA)**

A key development in the past year has been the refinement of our motion simulator (Figure 11, Figure 12) and our continuing efforts to develop realistic respiratory motion models. The simulator was redesigned to make it more robust and to match a change in the Cyberknife system geometry [Zhou 2004]. We have also refined the control software to provide a graphical user interface for the program and the ability to graphically preview motion files. This work builds on our previous efforts to measure and characterize respiratory motion. The motion simulator is capable of playing back almost any type of respiratory motion, from simple sinusoidal movements to irregular patterns based on recorded human data. Thus, with this simulator, we can 'play back' an individual patient's breathing pattern and use it as a test bed for different motion compensation strategies. Furthermore, because it has two independent platforms, it can produce skin motion that is different from internal organ motion, which is a more realistic simulation that could be produced by a single platform simulator.
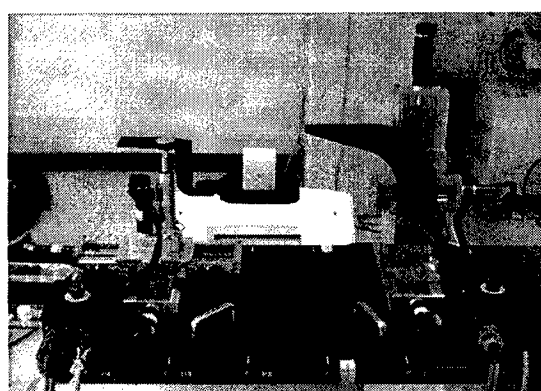
| | |
|---|---|
| **Figure 11: Detail photo of the respiratory motion simulator. Stage on the left simulates internal organ motion, stage on the right simulates skin motion** | **Figure 12: Respiratory motion simulator in use during Cyberknife experiment. Synchrony optical beacons are attached to the skin motion stage for tracking** |
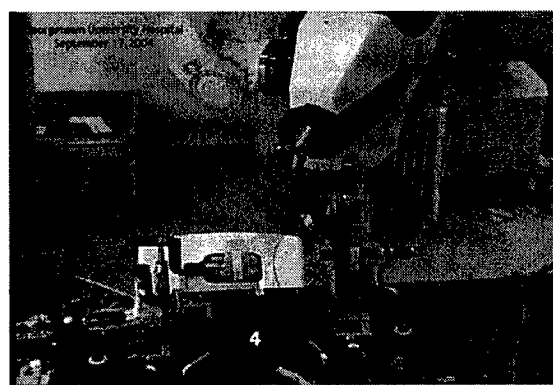
Patient respiratory motion patterns are drawn from several sources. One of these is magnetic resonance imaging (MRI). Using dynamic MRI, we are able to capture snapshots of the anatomy during respiration (Figure 13) and use these to build a numerical model of how internal organs move. We use both coronal and axial imaging slices, because the coronal orientation more clearly shows internal organ motion (which is largely along the superior-inferior axis) and the axial slices more clearly show the skin motion. MRI therefore allows us to determine for an individual patient how the skin motion translates to the motion of an internal organ; these data can then be used as input for the motion simulator [Wong 2004a, 2004b, 2005].



**Figure 13: Dynamic MRI images of patients acquired during free breathing. The imaging sequence used is trueFISP, which is fast enough to "freeze" the respiratory motion.**

Another method for creating motion simulator patterns is to examine the treatment logs from patients undergoing standard Cyberknife/Synchrony treatments. During Synchrony treatments, patients wear a tight fitting fabric vest to which small LEDs can be attached. These LEDs are observed by a Flashpoint optical tracker (Boulder Innovation Group, Boulder, CO, USA) which measures their 3D position several times per second. The patient is also periodically imaged with a stereo pair of x-ray tubes and detectors. Image

analysis software automatically segments the x-ray images and extracts the location of internal metallic fiducials that have been percutaneously implanted in the tissue around the tumor or in a nearby bony structure. The fiducials are placed before treatment planning and thus have a known geometric relationship to the center of the treatment target. The combination of these data therefore provide simultaneous measurement of an internal target position and an external skin position.

We are also investigating the use of electromagnetic tracking in the Cyberknife environment. This technology has the advantage of being able to provide direct motion tracking of internal organs, thereby eliminating potential uncertainties associated with skin motion tracking. The test was conducted in the CyberKnife suite at Georgetown as shown in Figure 14. The equipment consisted of the Aurora system, the CyberKnife, and the needle driver robot, used here as a precise positioner. The needle driver robot is holding an 18 gauge needle that has an Aurora sensor inside its tip. With some modifications, these needles might be used for tumor tracking in the abdomen or could be repackaged into other forms.

Test data was gathered by moving the robot in a pre-specified pattern, which was a rectangular volume of 200 by 40 by 50 mm. A total of 34 points were defined within this volume. At each measurement point the robot stops and the control computer calls the Aurora system to gather 100 readings which are then stored in a file. Aurora position data were collected with the CyberKnife LINAC at two different distances – 1000 mm and 500 mm from the tracking sensors – and with the LINAC beam on and off at each distance, for a total of four data sets.
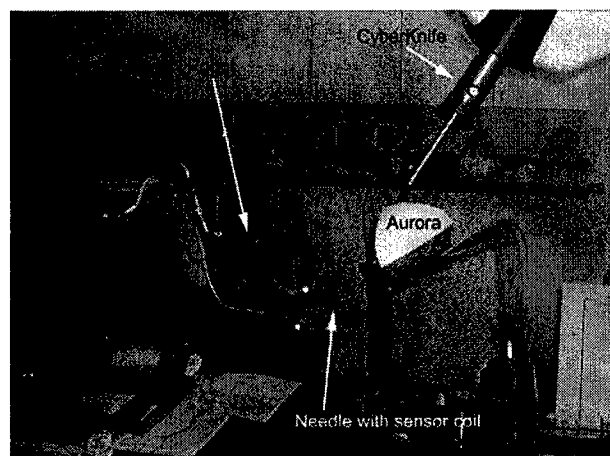


**Figure 14: Test setup showing CyberKnife, Aurora system, and robot positioner holding electromagnetically tracked needle.**

As can be seen in the table below, the average error was between 1.1 and 1.2 mm for all four tests with maximum errors of 4.1 to 4.3 mm. Based on this data, there appears to be no significant effect on Aurora accuracy from turning the CyberKnife beam on. The system error also appears to be acceptable for clinical use. However, this would need to be further validated in future studies.

| Test Set | Beam | Distance From Linac | Minimum Error | Maximum Error | Average Error | Standard Deviation |
|---|---|---|---|---|---|---|
| 1 | OFF | 1000 | 0.0007 | 4.2966 | 1.1501 | 0.8762 |
| 2 | ON | 1000 | 0.0049 | 4.1068 | 1.1031 | 0.8298 |
| 3 | ON | 500 | 0.0005 | 4.1683 | 1.1876 | 0.8698 |
| 4 | OFF | 500 | 0.0010 | 4.1458 | 1.1757 | 0.8710 |

**Table 1: Error and standard deviation of measurements (all numbers in mm)**

The primary disadvantage of this technology is that the markers cannot yet be made wireless, so patients would need to have wires emerging from their skin in order to read the data from the tracked fiducial.

# 3.5 Task 5: Rehabilitation Robotics

The primary goal of this effort is to develop robotic systems for assessment and physical therapy. The secondary goal is to expand this capability to the internet. We currently have seven ongoing projects in rehabilitation robotics spanning three robotic testbeds which are each described briefly below. We will continue to expand our activities in this area through ongoing collaborations with the National Rehabilitation Hospital, the University of Maryland, the Center of Excellence for Remote and Medically Under Served Areas (CERMUSA), and Interactive Motion Technologies. As some of these devices may be controlled through the Internet, a systematic study of information assurance and vulnerabilities will be an integral part of this effort.

## 3.5.1 InMotion2 Robot

The ISIS Center operaties a telerehabilitation testbed consisting of a pair of InMotion2 (IM2) robots from Interactive Motion Technology, Inc. (see Figure 15). The specific aims of our research are twofold: to enable a clinician to assess the physical condition of a patient's arm using metrics such as strength, dexterity, range of motion, and spasticity; and to help a clinician perform cooperative rehabilitative tasks with a patient using a virtual environment intended to simulate active daily living (ADL) tasks.

The IM2 Robot has direct-drive motors at the base which transmit forces to the handle through a four-bar linkage as shown in see Figure 16. The handle moves within a rectangle of dimension 90 x 60 cm just above the surface of the table. The maximum continuous force output of the robot at the handle is approximately 30 N in each direction. The handle is pinned to the end of the last link providing a third, unactuated degree of freedom. The IM2 robot is FDA-approved as both an evaluation device and therapy device with device listings R043555 and B004584, respectively.

We are currently using the IM2 testbed for four different projects, all of which will culminate in clinical trials to be conducted over the internet. Two projects are specifically aimed at developing protocols for stroke therapy. One project is to perform

neuroscience experiments for Parkinsonian patients over the internet. The remaining project is to develop cooperative, functional rehabilitation for populations with neurological deficits by using virtual reality technologies. These projects are described in more detail below [Carignan 2004a, 2004b, 2004c].
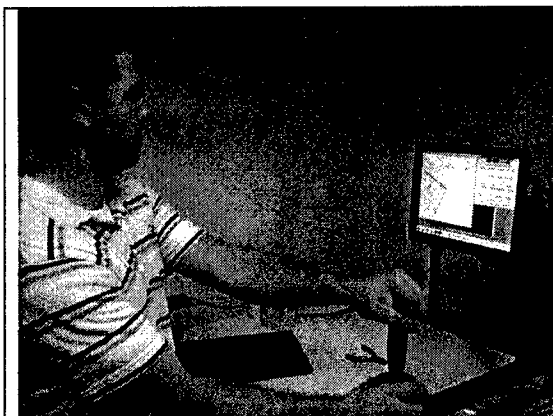


| Figure 15: An InMotion2 Robot undergoing systems checkout during installation | Figure 16: Top view of InMotion2 workstation showing 4-bar linkage, direct drive motors, and flat panel display |
| --- | --- |
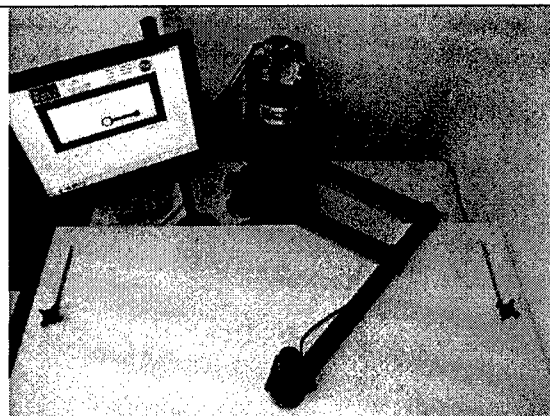
### 3.5.1.1 Stroke Rehabilitation

We are working with the National Rehabilitation Hospital and Morgan State University to develop robotic protocols for stroke therapy. The case study we are developing is to convert "skateboard" therapy currently being done manually into a protocol for the IM2 robot. When the therapy is conducted manually, the patient rests their elbow on a cart called a "skateboard" which moves along a table top as their hand moves in straight line directions. Since the IM2 is a planar, tabletop device, this was an ideal candidate for transfer to robotic therapy.

Our eventual goal is to conduct a pilot study to treat NRH patients over the internet using stroke doctor at Georgetown. The prototype software has been developed, but is currently being modified to provide force inputs to assist the patient during the task. The operator interface for the clinician is shown in Figure 17 and a sample shape traced out by the patient is shown in Figure 18.
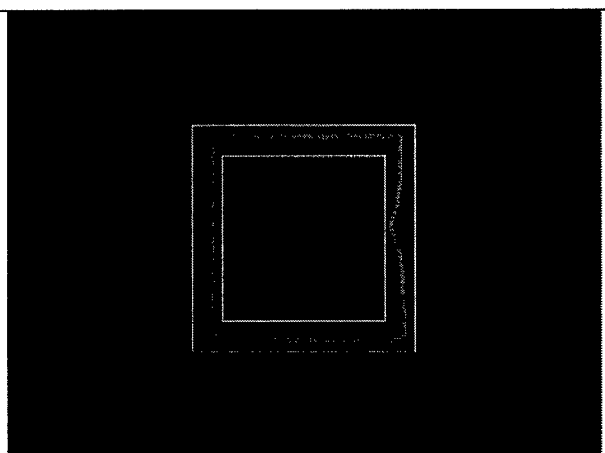
| | |
|---|---|
|  |  |
| **Figure 17: Graphical interface used by clinician in skateboard therapy protocol** | **Figure 18: A sample figure used in skateboard therapy. The bold line is the path traced out by the patient.** |

The second stroke therapy effort we are engaged in is with the John P. Murtha Neuroscience and Pain Institute in Johnston, PA. We are working with personnel from the institute and CERMUSA to broaden a pilot study done at the Helen Hayes Hospital which varied center of workspace for IM2 therapy (see Figure 19). The goal is to enlarge database and give CERMUSA experience with robotic therapy. The protocol has been written and the IRB application is currently being prepared.

## 3.5.1.2 Sensorimotor Adaptation

This neuroscience investigation is a joint project being conducted with the Department of Kinesiology at the University of Maryland. It is a pilot study to examine the feasibility of using robotic platforms to develop large-scale computational models of sensorimotor function of healthy subjects. This research is an intermediate step towards (a) understanding, validating and testing brain model-machine interfaces, and (b) eventually developing robotic interventions for treating patients with neural disorders such as Parkinsons Disease and stroke hemiplagia.

By using the FDA-approved InMotion2 robot to apply either kinematic distortions or small force perturbations to the hand, we will study the changes in the kinematics of movement as a function of practice. From this data, large-scale computer models of neural circuits can be developed to help elucidate not only the biological principles underlying adaptive cognitive-motor behavior, but also to integrate and advance our understanding of multi-modal brain data. By doing this study with healthy subjects, we hope to establish a baseline model which can then be compared with future studies involving patients with neural disorders.

The protocol for this trial has been approved by both Georgetown University and the U.S. Army. Approval by the University of Maryland IRB is currently pending. The basic setup for this study is shown in Figure 20. We expect the trial to be underway shortly.

| Figure 19: InMotion2 robot at CERMUSA to be used in stroke therapy clinical trial | Figure 20: Operator interface for proposed sensorimotor clinical trial |
|---|---|
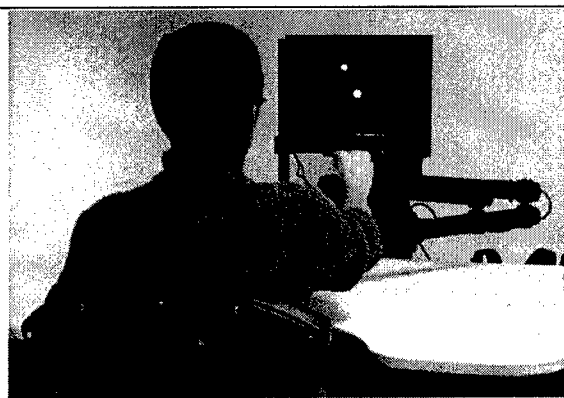
## 3.5.1.3 Tele-Rehabilitation

The tele-rehabilitation testbed is being used to study the feasibility of conducting remote assessment and therapy over the internet. The specific aims of our research are twofold: to enable a clinician to assess the physical condition of a patient's arm using metrics such as strength, dexterity, range of motion, and spasticity; and to help a clinician perform cooperative rehabilitative tasks with a patient using a virtual environment intended to simulate active daily living (ADL) tasks. The system architecture for connecting the two robots over the internet is shown in Figure 21.

To-date, we have successfully conducted a cooperative beam task between Georgetown University and Interactive Motion Technology in Cambridge, Massachusetts. Internet delays of up to 110 ms were observed which caused borderline stability without compensation. The wave-variable controller was found to be robust to variations in time-delay, and performance degraded only gradually with increasing delay. The degradation manifests itself as a higher perceived inertia at the handle which was still quite manageable even with artificially induced delays of over 1 sec.

Current work is focused on generating more realistic 3D tasks created using Open Inventor Toolkit and rendered on a head mounted display (see Figure 22). A head tracker is used to track orientation of the subject's head for changing viewing. Future work will focus on generating additional cooperative tasks over the internet aimed at improving recovery from stroke paralysis and other neurological disorders.

| Figure 21: System architecture for cooperative rehabilitation over the internet | Figure 22: Cooperative beam task using robot haptic interface and VR goggles |
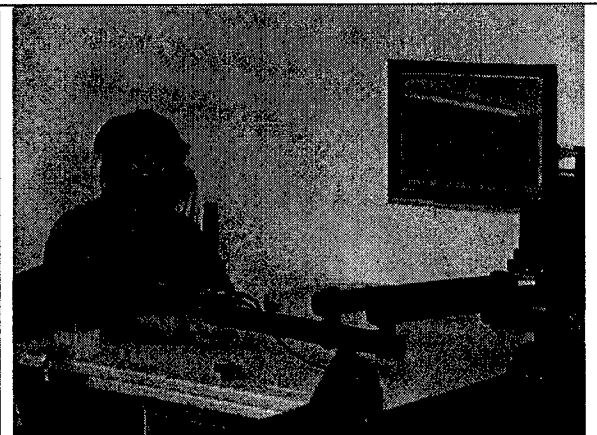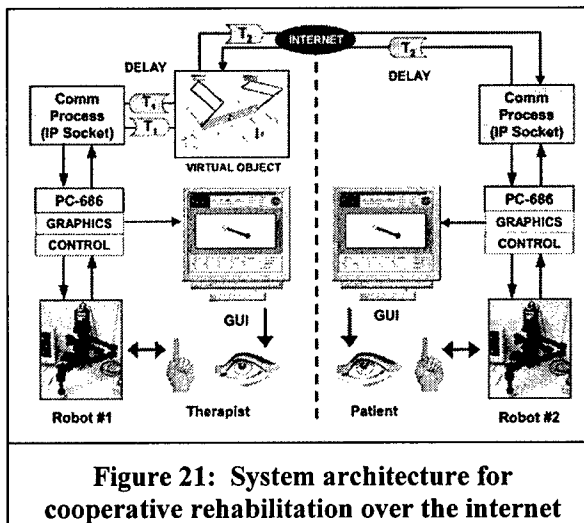
## 3.5.2 MGA Exoskeleton

The Maryland-Georgetown-Army (MGA) Exoskeleton is an upper arm robotic exoskeleton being developed for assessment and rehabilitation of shoulder pathology. There are five degrees of freedom: three joints for shoulder rotation, one for elbow flexion/extension, and one for scapula elevation/depression (see prototype in Figure 23). The exoskeleton will be used to assess arm strength, speed, and range of motion using onboard sensors, and function as both a resistance trainer and virtual reality tool for rehabilitation. Operation of the device will be monitored by a computer-controlled safety system based on an architecture developed for a NASA robotic flight experiment.

This project is a joint venture between the Georgetown University Imaging Science and Information Systems (ISIS) Center and the Space Systems Laboratory (SSL). The robotic hardware will be built, tested, and integrated by the SSL robotics group, and the ISIS Center will lead the controls effort and assist with the kinematic design, electronics, and operations. The hardware for the exoskeleton is currently in fabrication (see CAD drawing in Figure 24), and assembly and integration will commence in the spring.



| Figure 23: Exoskeleton prototype being test fitted on human subject | Figure 24: CAD drawing of complete MGA exoskeleton |
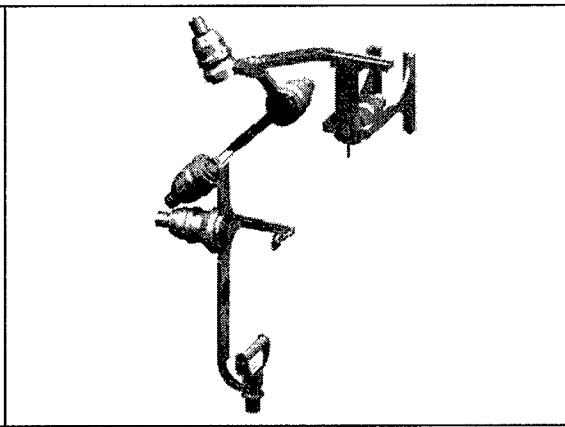
### 3.5.3 Keiser Arm Curl Machine

We are currently developing a powered exercise machine that can be used for physical therapy. A Keiser arm curl machine was retrofitted with a linear actuator (see Figure 25), and an onboard microprocessor controls the motor based on feedback from a position and force sensor. Resistance laws are programmed on a PC and an admittance controller outputs commands to the motor. The experimental setup is shown in Figure 26. Preliminary results for simulating free weight and viscoelastic resistances were encouraging. Future work will include building an analog filter and using shielded cable for the load cell to help suppress noise in the force signal. After these hardware issues are addressed, we will begin testing new resistance laws that change over the course of a repetition.
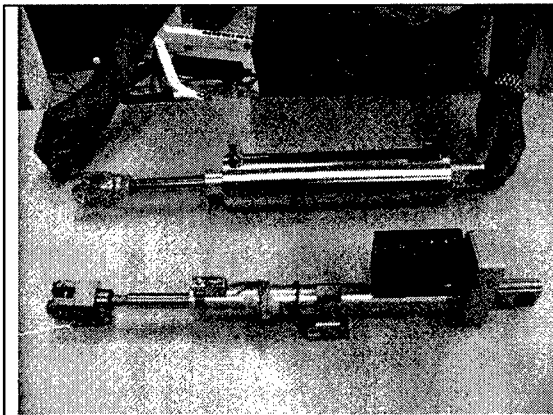


| Figure 25: Ultramotion Smart Motor beside the Keiser pneumatic piston. | Figure 26: Keiser Arm Curl 250 retrofitted with the Smart Motor actuator. |

## 3.6 Task 6: Surgical Planning and 3D Visualization

The goal of this task is to develop a surgical planning capability that allows integration of innovative surgical techniques such as image processing and visualization for neurosurgery, vascular surgery, and interventional radiology applications. We have two major thursts:

1. image-guided transbronchial biopsy (clinical lead, Eric Anderson, MD, pulmonology)
2. skull-base subtraction (clinical lead, Dan Nguyen, MD, neuroradiology).

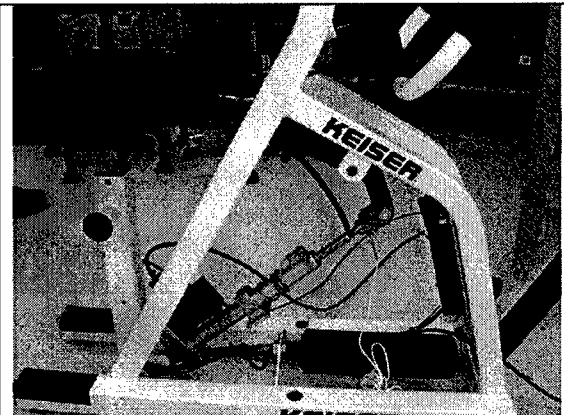### 3.6.1 Image-guided Transbronchial Biopsy

In conventional transbronchial biopsy, the planning is very simple. Pulmonologists look at the pre-operative CT scan, specify the target biopsy location, and estimate the biopsy location. During the operation, pulmonologists manipulate the bronchoscope to the estimated biopsy location and take a biopsy sample. However, the failure rate is quite high as bronchoscope video is the only tool used to determine the biopsy location. By providing transparent virtual bronchoscopic images, doctors are able to see the target lymph nodes through the mucosa wall, which can result in enhanced biopsy accuracy. We are currently developing a system to provide these capability. To date, we have

developed some of the software components including transparent visualization, registration and tracking. Figure 27 shows the components and workflow for this system.
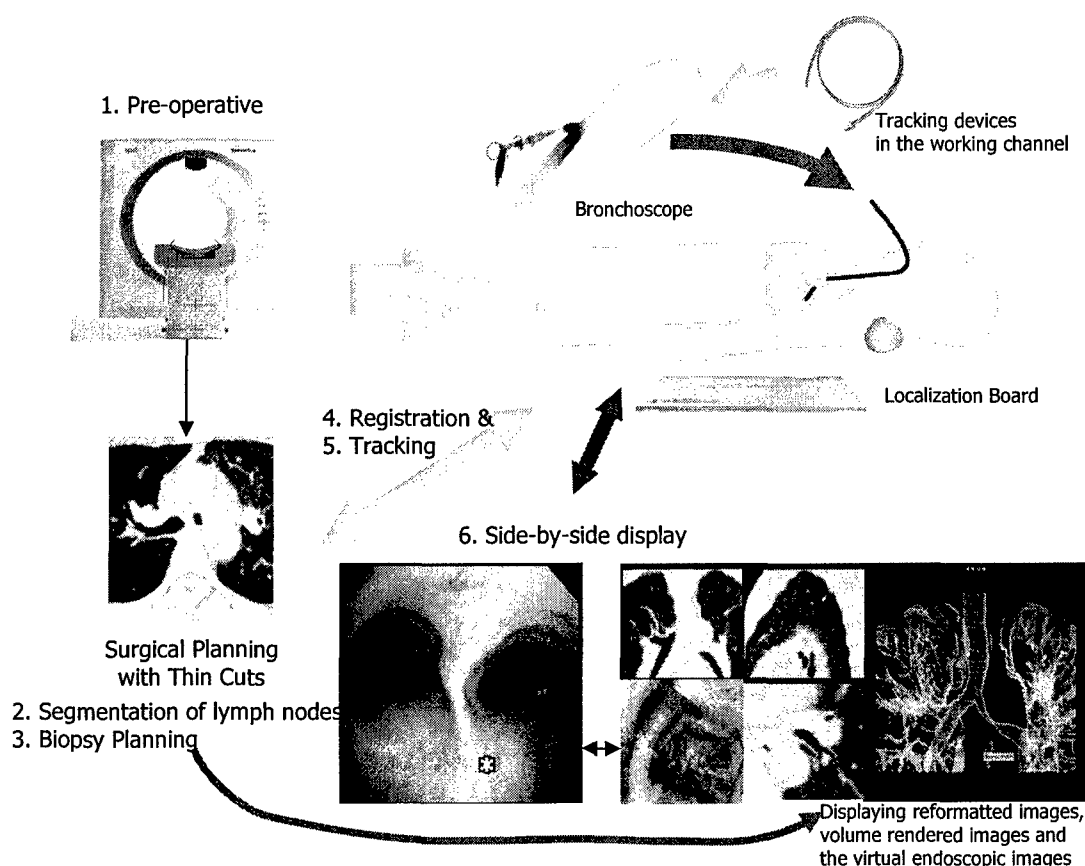


**Figure 27. System overview of image-guided transbronchial biopsy**

## 3.6.2 Skull-base Subtraction

The goal of this research project is to develop an optimal skull base subtraction method to assist neuroradiologists in interpreting high-resolution CT angiography images. We hypothesize that combining

    1) appropriate CT scans before and after injecting the contrast agent; and

    2) appropriate registration and subtraction methods between the two scans

may significantly improve the detection of aneurysms and their quantitative analysis such as their location, size and shape. An FDA approved workstation (TeraRecon, San Mateo, California, USA) was used for volumetric rendering as shown in Figure 28(a). The result was then compared to traditional digital subtraction angiography (DSA), the current gold standard, and 3D rotational DSA (rDSA) for image correlation (Figure 28(b)). The aneurysm morphology such as overall size, neck origin, and neck size is better seen when a skull base subtraction technique is applied to intracranial CTA. These important parameters show similar image correlation on skull base subtraction CTA images as they do on the 3D rotational DSA images.

(a)                                          (b)
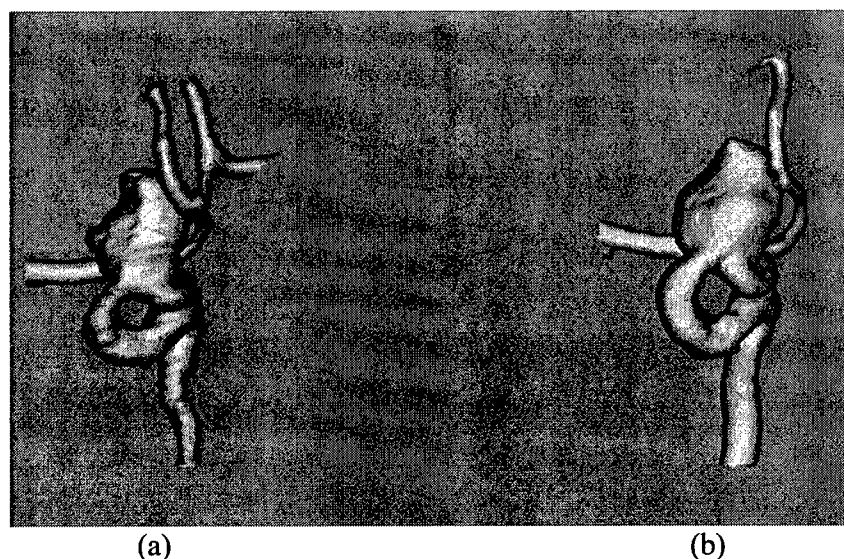
**Figure 28: (a) Bone subtraction angiography and
(b) rotational digital subtraction angiography**

From these studies, we found that traditional CTA is limited at the level of skull base where osseous structures are the predominant factor. The skull base subtraction technique enhances visualization of vascular pathology within this level. This subtraction technique is operator non-dependent, and requires little additional post-processing effort. Most importantly, it adds additional diagnostic certainty to our noninvasive CTA armamentarium. We have submitted this result to the ASNR (American Society of NeuroRadiology) 2005 annual conference [Choi 2005].

# 4 Key Research Outcomes

This section provides a bulleted list of key research accomplishments during the entire project:

- Received FDA approval to conduct a clinical trial for robotically assisted spinal blocks and completed twenty patients

- Completed a feasibility demonstration of robotically assisted lung biopsy using frame-grabbed CT fluoroscopy images and a respiratory motion phantom

- Completed an initial set of approved animal studies demonstrating the feasibility of electromagnetic position sensing for image guidance in the interventional suite

- Gathered skin motion data on four patients during CyberKnife stereotactic radiosurgery treatments under an IRB-approved protocol

- Developed a respiratory motion simulator consisting of two 3 degree of freedom platforms to evaluate CyberKnife treatments which compensate for internal organ motion

# 5 Reportable Outcomes

This section provides a list of reportable outcomes.

The major product of this year is the list of papers given in Section 9, References. Copies of these documents are provided in the appendix.

In addition, several proposals to the National Institutes of Health were submitted based on this work. A grant was received from NIH/NCI to develop robotically assisted lung biopsy. Several small business grants were received with company partners, including one on electromagnetic tracking and one on open source software.

A graduate student from Catholic University and a graduate student from Johns Hopkins University were supported to assist in software development for the robotic needle driver. The research group at Georgetown continued to take a lead in the Washington Area Computer Aided Surgery Society (www.washcas.org), which was formed in 2000 to promote research in the field.

# 6 Conclusions

The Periscopic Spine Surgery project has continued to lay the ground work for developing the physician assist systems of the future. These systems will incorporate robotics, tracking, and visualization to improve the precision of instrument placement and manipulation in minimally invasive procedures. The world's first clinical trial of robotically assisted needle placement for spinal nerve blocks was begun and twenty patients were enrolled. The feasibility of electromagnetic position sensing and image overlay was demonstrated in an animal study. A respiratory motion simulator was developed to evaluate CyberKnife treatments which compensate for internal organ motion. This project has enabled the Georgetown team to become a world leader in the emerging fields of computer aided surgery and medical robotics. Our goal will continue to be to develop systems to add the physician in these demanding minimally invasive procedures with the ultimate aim of improving patient care.

# 7 References

[Carignan 2004a]      Craig R. Carignan and Pontus A. Olsson, "Cooperative Control of Virtual Objects over the Internet using Force-Reflecting Master Arms," *Proceedings of the 2004 IEEE Int. Conf. on Robotics & Automation*, pages 1221-1226.

[Carignan 2004b]      Pontus A. Olsson, Craig R. Carignan, and Jonathan Tang, "Cooperative Control of Virtual Objects using Haptic Teleoperation over the Internet," *Proceedings of the 5$^{th}$ Int. Conf. on Disability, Virtual Reality and Assoc. Technologies*, Sept. 2004, Oxford, pages 149-156.

[Carignan 2004c]      Craig Carignan, Pontus A. Olsson, and Jonathan Tang, "Robotic Rehabilitation over the Internet," *SPIE International Technical Group Newsletter*, October 2004, Volume 13, Number 2, pages 3 and 9.

[Choi 2005]      Jae Choi, Dan Nguyen, and Kevin Cleary, "Bone Subtraction CTA Techniques for Skull Base Vascular Related Pathology: Initial Clinical Experience," abstract submitted to *American Society of Neuroradiology* annual meeting, Toronto, Canada, May 2005.

[Cleary 2004]      Kevin Cleary, Filip Banovac, David Lindisch, Dan Stoianovici, Alexandru Patriciu, Dumitru Mazilu, Sheng Xu, Gabor Fichtinger, Russell Taylor, and Charles White, "Robotically Assisted Lung Biopsy under CT Fluoroscopy: Concept and Phantom Study," submitted to *Academic Radiology* in November 2004.

[Mihaescu 2005]      Christian Mihaescu, Luis Ibanez, Mihai Mocanu, and Kevin Cleary, "Needle Targeting under C-Arm Fluoroscopy Servoing," presented at the S*PIE Medical Imaging Symposium* and to be published in the *Visualization, Image-Guided Procedures, and Display track*, San Diego, CA, 2005.

[Wong 2005]      Kenneth H. Wong, Jonathan Tang, Hui Zhang, Emmanuel Varghese, and Kevin Cleary, "Prediction of 3D Internal Organ Position From Skin Surface Motion: Results from Electromagnetic Tracking Studies," presented at the *SPIE Medical Imaging Symposium* and to be published in the *Visualization, Image-Guided Procedures, and Display track*, San Diego, CA, 2005.

[Wong 2004a]      Kenneth H. Wong, Jonathan Tang, Sonja Dieterich, Hui Zhang, Tong Zhou, and Kevin Cleary, "Respiratory Motion Compensation Studies Using a 3D Robotic Motion Simulator and Optical/Electromagnetic Tracking Technologies," presented at the *2004 IEEE Nuclear Science Symposium and Medical Imaging Conference*, Rome, Italy, 2004.

[Wong 2004b]          Kenneth H. Wong, John W. VanMeter, Stanley T. Fricke, Calvin
                      R. Maurer Jr., and Kevin Cleary, "MRI for modeling of liver and
                      skin respiratory motion." in *Computer Assisted Radiology and
                      Surgery (CARS)* 2004, Proceedings of the *18th Annual Congress
                      and Exhibition*, Chicago, IL, 2004, Elsevier, pages 747-752.

[Wood 2004]           Bradford Wood, Dave Lindisch, Sohan Ranjan, Neil Glossip, and
                      Kevin Cleary, "Electromagnetically tracked guidewires for
                      interventional procedures," in *Computer Assisted Radiology and
                      Surgery (CARS)* 2004, Proceedings of the *18th Annual Congress
                      and Exhibition*, Chicago, IL, 2004, Elsevier, page 1309.

[Zhou 2004]           Tong Zhou, Jonathan Tang, Sonja Dieterich, and Kevin Cleary, "A
                      robotic 3-D motion simulator for enhanced accuracy in CyberKnife
                      stereotactic radiosurgery." in *Computer Assisted Radiology and
                      Surgery (CARS)* 2004, Proceedings of the *18th Annual Congress
                      and Exhibition*, Chicago, IL, 2004, Elsevier, pages 323-328.

# Cooperative Control of Virtual Objects over the Internet using Force-Reflecting Master Arms

Craig R. Carignan *                     Pontus A. Olsson [†]

Imaging Science and Information Systems (ISIS) Center
Department of Radiology
Georgetown University
Washington, DC 20007

## Abstract

*Force-reflecting master arms are explored for use as haptic displays in physical therapy interventions over the internet. Rehabilitation tasks can be constructed in which both the patient and therapist can interact with a common object from distant locations. Each haptic master exerts "forces" on a virtual object which, in response, generates desired velocities for the master arm to track. A novel cooperative control architecture based on wave variables is implemented to counter the destabilizing effect of internet time-delay. The control scheme is validated experimentally using a pair of InMotion2 robots in a virtual beam manipulation task between remote sites.*

## 1 Introduction

The Imaging Science and Information Systems (ISIS) Center at Georgetown University is currently engaged in an effort to develop robotics for tele-rehabilitation. One of the chief goals of this project is to connect physiotherapy robots in remote locations for clinical assessment and treatment of patients with neuromuscular disorders. A pair of InMotion2 (IM2) robots from Interactive Motion Technologies has recently been integrated into a testbed at the ISIS Center to facilitate this effort [10].

The IM2 "robot" is a direct-drive, four-bar linkage with a planar workspace of 90 × 60 cm and maximum continuous force output of 30 N in each direction (see Figure 1). The handle is pinned to the distal end of the outboard link providing a third, unactuated degree of freedom. The linkages result in an apparent stiffness of 6000 N/m and inertia of 1.33 kg at the handle.

---

*Research Associate Professor, Dept. of Radiology, crc32@georgetown.edu

[†]Senior Undergraduate, Department of Electrical Engineering, Royal Institute of Technology (KTH), Stockholm, Sweden, pontuso@kth.se

The low inherent dynamics of the IM2 robot makes it ideally suited for incorporating haptic virtual reality (VR) into our strategy for physical therapy over the internet. This will allow the clinician to remotely assess the patient's condition as well as assist the patient perform rehabilitation tasks. Implementing force-feedback in the presence of time-delay will be a key factor in realizing this technology over the internet and is a cornerstone of the control architecture presented here.
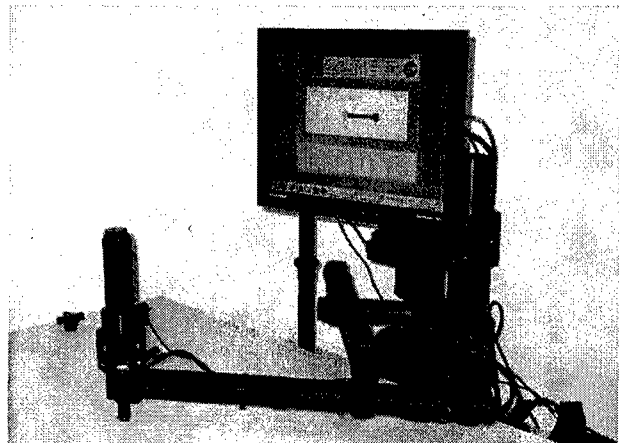


Figure 1: Four-bar linkage InMotion2 Robot with graphic display of virtual beam task.

This article begins with a brief review of previous work on cooperative haptics and time-delay compensation in Section 2. A cooperative beam handling task using admittance control for low-order (processing) time delays is considered in Section 3. A control architecture based on wave variables is introduced in Section 4 for handling larger (internet) time-delays. Experimental results on the IM2 testbed for both types of controllers are presented in Section 5 for a virtual beam manipulation task. Conclusions on the implementation of this approach are given in Section 6 along with some directions for future research.

## 2 Previous Work

Simultaneous application of multiple haptic devices has been attempted on several VR platforms. A pair of 2-DOF master manipulators was used to simulate thumb and index fingertip contact with an object during a peg-in-hole insertion task [8, 2]. Dual-arm contact with a steering wheel was simulated using a pair of 6-DOF PHANToM devices for arm motor control training [6]. NASA researchers are using a pair of Charlotte IVA robots to simulate large satellites during astronaut training [15, 3]. A pair of 6-DOF, parallel force displays was used at the University of Tsukuba for performing interactive patient-therapist tasks over the internet [16]. Predictive displays were used to help operators adjust for up to 3 sec delays, but time-delay compensation was not implemented.

Several investigators have incorporated explicit time-delay compensation in the force-feedback loops of haptic systems. NASDA used a straightforward approach whereby damping was increased in the PD control loop to maintain stability during ground-based teleoperation of the Japanese ETS-VII experiment in 1997 [9]. Scattering theory was explored by [11] to produce passive communications during teleoperation of a metal block. Wave variables were introduced by [14] for a variety of master/slave scenarios with widely varying time delay. More recently, [1] considered time-delay in their passivity control formulation of stable interaction with virtual environments. However, none of the investigations cited considered time-delay compensation in the context of multiple haptic displays.

## 3 Admittance Control for Low Time-Delay

The system block diagram for a cooperative virtual object manipulation task is shown in Figure 2. Each haptic master is outputting a set of desired forces to a virtual object generator (VOG) via their force/torque sensor readings and in response receiving a set of desired velocity commands to track from the virtual object. For processing delays under approximately 10 msec, this strategy produces acceptable behavior. But when the delays are on the order of 100 msec, instability is easily induced in the system.

The control block diagram for the master arm is shown in Figure 3. This is a classical admittance control implementation in which the haptic master is using force input to generate a set of desired velocity commands ([7],[4]). The velocity commands are then tracked using a PD controller implemented in Cartesian space using the control law given by

$$F_c = B_m(\dot{x}_{md} - \dot{x}_m) + K_m(x_{md} - x_m) \qquad (1)$$

where $B_m$ and $K_m$ are diagonal damping and stiffness gains, respectively, and $F_c$ is the commanded force represented in Cartesian "operational" space.
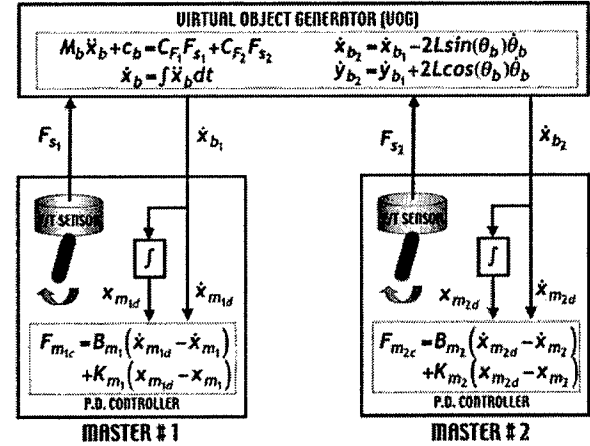


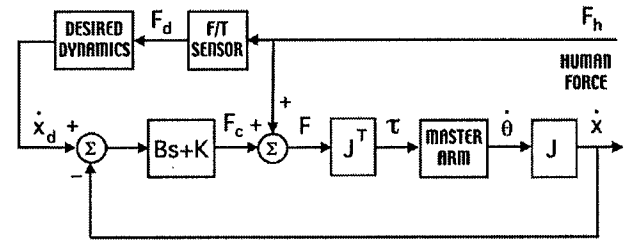Figure 2: System block diagram showing haptic master impedance controller and virtual object generator.



Figure 3: Admittance controller block diagram.

The master arm dynamics in operational space are computed from

$$M_x \ddot{x}_m + c_x(x_m, \dot{x}_m) + g_x(x_m) = F_c + F_h \qquad (2)$$

where $F_h$ is the force applied by the human operator at the handle [5]. For haptic devices in general, the inertial $M_x$ and Coriolis/centripetal forces $c_x$ on the left side of (2) are low. In addition, the gravitational force $g_x$ for the IM2 robot is zero since the planar workspace is perpendicular to the gravity vector. Therefore, the force applied by the human $F_h$ is approximately equal but opposite the commanded force $F_c$.

The VOG calculates the dynamics of the virtual object being manipulated by the master arm. In the cooperative beam manipulation task in Figure 4, each haptic master is grasping one end of a beam and lifting it against gravity. The grasp point is the handle pinned at the distal end of the last link, and the simulated gravity vector is pointed in the sagittal plane of the operator so that s/he is pushing away when lifting the beam (toward the screen in Figure 1).

The position of the left end of the beam is $(x_{b_1}, y_{b_1})$ and the right side is $(x_{b_2}, y_{b_2})$. The orientation of the beam with respect to the $x_0$-axis is given by $\theta_b$. The total length of the beam is $2L$ so that the relationship between the left and right position is given by
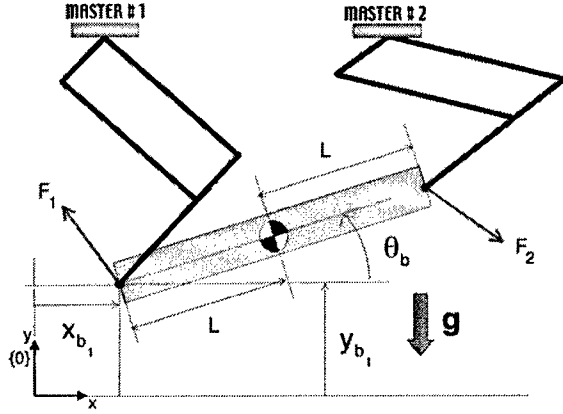
Figure 4: Cooperative beam manipulation task.

$$x_{b_2} = x_{b_1} + 2L\cos(\theta_b) \tag{3}$$
$$y_{b_2} = y_{b_1} + 2L\sin(\theta_b)$$

The center of mass of the beam (CM) is chosen to be at the geometric center, and the beam is assumed to be a uniform slender rod so that the inertia about its center of mass is given by $i_b = \frac{1}{3}m_b L^2$.

The resulting beam dynamics are given by

$$M_b(x_b)\ddot{x}_b + c_b(x_b, \dot{x}_b) = C_{F_1}F_1 + C_{F_2}F_2 + m_b a_g \tag{4}$$

where

$$M_b(x_b) = \begin{bmatrix} m_b & 0 & -m_b L s_b \\ 0 & m_b & m_b L c_b \\ -m_b L s_b & m_b L c_b & i_b + m_b L^2 \end{bmatrix}$$

$$\ddot{x}_b = \begin{bmatrix} \ddot{x}_{b_1} \\ \ddot{y}_{b_1} \\ \ddot{\theta}_b \end{bmatrix}, \quad c(x_b, \dot{x}_b) = \begin{bmatrix} m_b L c_b \\ m_b L s_b \\ 0 \end{bmatrix}$$

$$C_{F_1} = \begin{bmatrix} 1 & 0 & 0 \\ 0 & 1 & 0 \\ 0 & 0 & 1 \end{bmatrix}, \quad F_1 = \begin{bmatrix} f_{1x} \\ f_{1y} \\ n_{1z} \end{bmatrix}$$

$$C_{F_2} = \begin{bmatrix} 1 & 0 & 0 \\ 0 & 1 & 0 \\ -2L s_b & 2L c_b & 1 \end{bmatrix}, \quad F_2 = \begin{bmatrix} f_{2x} \\ f_{2y} \\ n_{2z} \end{bmatrix}$$

where $c_b \equiv \cos(\theta_b)$, $s_b \equiv \sin(\theta_b)$, and $a_g^T = [0 \ -g \ 0]$ is the gravitational acceleration vector.

## 4  Wave Variable Control

There are many approaches for dealing with instability caused by time delay, but the wave variable approach seems to produce a natural interface for manipulating objects over the internet [13, 14]. Instead of sending a direct velocity or force command, an impedance "wave" command is issued by the master, and then an impedance "wave" is reflected by the slave. How much of the push wave is reflected depends upon the impedance on the slave side. A soft, spring-like environment has a low impedance so will not reflect the incoming wave as greatly as a rigid environment. In addition to its impedance/admittance analog, the performance of the wave variable controller degrades only gradually with increasing time delay and so is well-suited to the environment of the internet.

When using the wave variable approach, it is important to distinguish between which object(s) is the "master" and which is the "slave". In our application, the virtual object is regarded as the "slave" and is acted upon by virtual forces from the two IM2 robots which are the "masters". Each of these "applied" forces are computed from the transmitted wave variable from the master as follows

$$F_s = -b\dot{x}_s + \sqrt{2b}u_s \tag{5}$$

The VOG then computes its outgoing wave variable using

$$v_s = \frac{b\dot{x}_s - F_s}{\sqrt{2b}} \tag{6}$$

The incoming wave to the master is then $v_m(t) = v_m(t - T)$.

The desired master velocity, $x_{md}$, is computed from the master force and return wave variable $v_m$ as follows:

$$u_m = \frac{b\dot{x}_{md} + F_m}{\sqrt{2b}} \tag{7}$$

The incoming wave to the slave is then given by $u_s(t) = u_m(t - T)$. If the master force command $F_c$ is used to compute the master force in (7), $F_m = -F_c$ and (1) and (7) form a recursive loop. Substituting (1) into (7) and solving for $\dot{x}_{md}$ gives

$$\dot{x}_{md} = \frac{\sqrt{2b}v_m + B_m\dot{x}_m + K_m(x_m - x_{md})}{B_m + b} \tag{8}$$

$$x_{md} = \int_0^t \dot{x}_{md}(\tau)d\tau$$

The control architecture for the cooperative task using a wave variable implementation is shown in Figure 5. In this scenario, each haptic master is independently interacting with the virtual object which is considered the "slave". The virtual object process then decodes the wave variables from the masters into a set of force commands to be imparted on the slave. The virtual object generator calculates the resultant motion at each of the "contact" points and transmits it via wave variable back to the master. Each master control process then decodes the slave wave variables into desired velocities at its "contact" point. The desired velocity vector (along with the integrated value) is then input to the master's PD tracking controller.
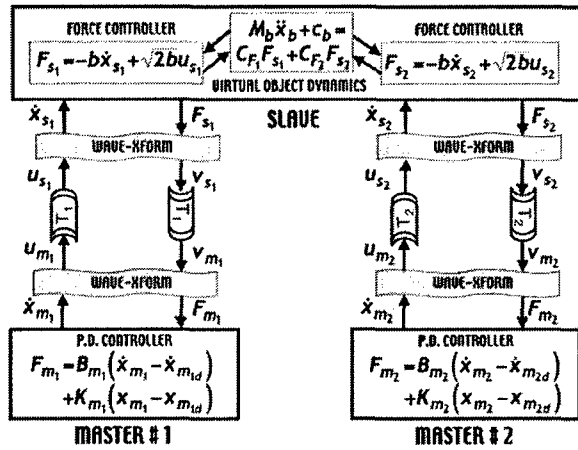
Figure 5: Wave variable control architecture.

The virtual object dynamics are calculated via a separate process on one of the master arm computers. $T_1$ and $T_2$ are time delays caused by either internet transit or computational processing. If the beam dynamics are being calculated on the master 1 computer, then $T_1$ is primarily the computational delay for the beam dynamics process (essentially zero), and $T_2$ is the internet time delay for a signal to reach master 1 from master 2. However, to maintain a truly cooperative task, the two time delays should be matched. Therefore, an artificial time delay based on a moving average of the internet time delay is applied to the master control computer hosting the virtual object process.

The effect of an increase in time delay on the wave variable implementation is to decrease the system's natural frequency. This communications "stiffness" $K_{comm}$ is given by $b/T$. Thus $b$ should be increased in proportion to the time delay to maintain the stiffness in the system [12]. For a processing time delay of 0.075 msec, $b=5$ was found to produce good tracking performance. For roundtrip time delays of 50-100 msec, $b=40$ was required to maintain similar performance.

# 5 Dual-Arm Beam Manipulation Experiment

The architecture of the IM2 rehabilitation testbed is shown in Figure 6. Each operator receives both visual (GUI) and haptic input (IM2) from the system which is being driven by an AMD XP1800 PC with Athlon 686 processor running at 1533 MHz. The control process was implemented in RT-Linux and uses approximately 1.2% of the CPU time at a rate of 200 Hz. Fast internet communication between robots was achieved using UDP protocol which enabled transfer rates of 100 Hz for typical tests. The time delay for the therapist's computer, $T_1$, was set equal to the internet time delay $T$ to maintain symmetry in the force

interaction between the VOG and two robots.

Two sets of experiments were performed to illustrate the cooperative beam manipulation task over the internet: admittance control under just processing delay, and wave variable control in the presence of internet time delay. In all tests, the master controller had a bandwidth of 30 rad/sec and was critically damped yielding gains of $K_m=900$ N/m and $B_m=60$ N/m/s. The beam parameters were $m_b=10$ kg, $L=0.15$ m, and $i_b=0.075$ kg-m$^2$. A reduced gravitational acceleration of $g=3$ m/s$^2$ was used in order not to exceed the force capacity of the robot. Parameters could be changed by the operator using the graphical user interface shown previously in Figure 1.
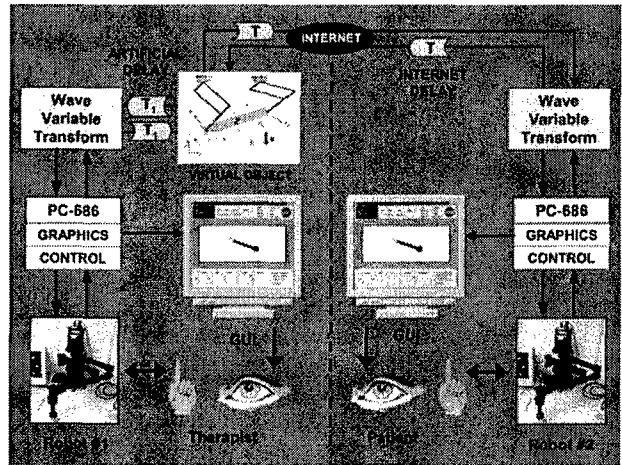


Figure 6: Hardware configuration of the system.

In the first set of tests, the impedance control scheme of Figure 2 was used. The control and communication rates were 200 Hz, and the time delay within our own IP domain was only 0.15 msec. The beam starts out horizontally and then is lifted by the haptic master on the left until it reaches the vertical position. Then the second haptic master raises the right side of the beam until it is again horizontal. The plot of the beam angle $\theta_b$ versus time is shown in Figure 7.

The plots of the commanded vertical forces on the beam (sensed master forces) are shown in Figure 8. $F_y$ for haptic master 1 is seen to go to zero when the beam reaches a vertical position while haptic master 2 sustains the full load of the beam. After master 2 raises its side of the beam, the force becomes equally distributed again. The desired versus actual velocities are shown in Figure 9 for master 1 and indicate very good tracking by the PD controller.

In the second set of tests, the wave variable control scheme of Figure 5 was used. The controller rate was decreased to 100 Hz due to the bandwidth limitation of the communication process, and the wave impedance parameter $b$ was increased to 40 to compensate for the additional delay. An artificial communication time delay of approximately 50 msec was introduced between the therapist's commands and the virtual object to
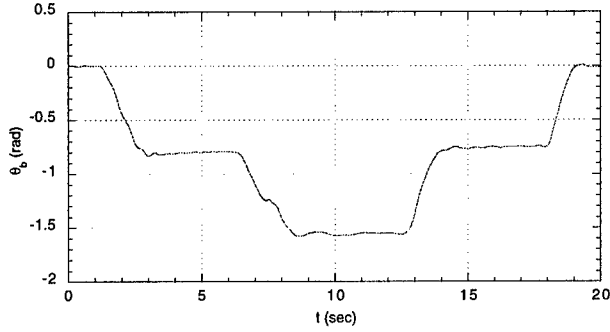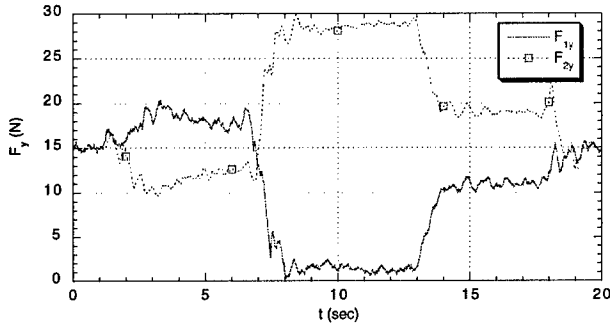
Figure 7: Beam angle under admittance control.



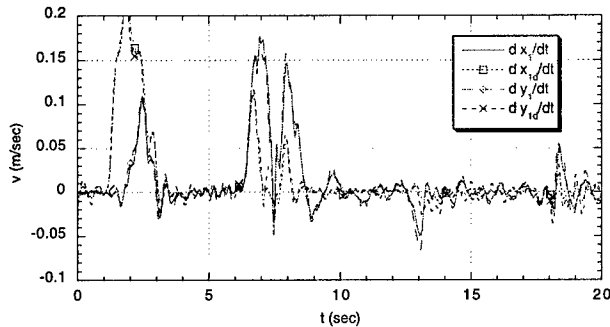Figure 8: Y-contact forces under admittance control.



Figure 9: Desired and actual velocity of master 1 under admittance control.



Figure 10: Beam angle under wave variable control.
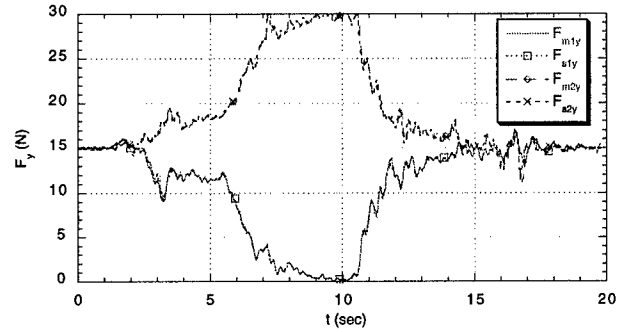


Figure 11: Y-contact forces under wave variable control.
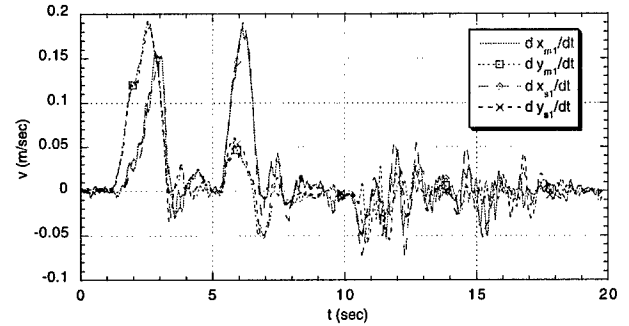


Figure 12: Desired and actual velocity of master 1 under wave variable control.

balance the internet communication delay between the two computers.

The beam was manipulated in the same manner as before yielding the beam angle $\theta_b$ shown in Figure 10. The commanded master and slave forces in the $y$-direction for the two haptic masters are shown in Figure 11. $F_y$ for both masters starts out equal and then goes to zero for master 1 when the beam reaches a vertical position and master 2 sustains the full load of the beam. The desired versus actual velocities for haptic master 1 shown in Figure 12 indicate very good tracking by the wave controller.

The roundtrip internet time delay between Georgetown University and Cambridge, Mass. for this test is shown in Figure 13. The time delay varied between 35 and 110 msec and averaged about 50 msec. A 10 sec

window was used to compute a moving average for the artificial delay $T_1$ to be applied to master 1.

# 6 Conclusion

This paper has outlined a strategy for cooperative, force-feedback control of virtual objects over the internet based on using impedance control for low time-delay and wave variables for large time delay. Experiments indicate that the impedance control approach is stable for round trip time delays under about 90 msec but degrades rapidly thereafter. Above 100 msec delay, the robot handle must be grasped firmly or any imparted forces produce rapidly divergent behavior.

Figure 13: Internet roundtrip time delay.

By contrast, the wave variable approach was stable for a wide range of time delays tested, including artificial delays of over 1 sec. The commanded force must be used to generate the wave variables because the sensed force (which neglects the haptic dynamics) violates passivity. Very good tracking of the desired dynamics was achieved in an actual task performed over the internet for time delays varying between 35 and 110 msec. However, the time-dela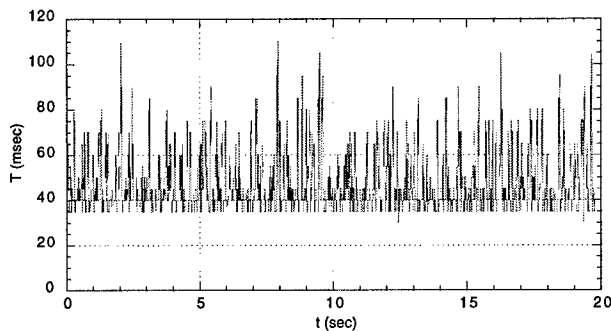y compensation comes at the cost of perceived heavier inertia and damping at the handle due to the increased wave impedance.

Future work will focus on generating additional cooperative tasks and experimenting with longer time delays that are more characteristic of broadband systems (T1 lines used in these tests). In addition, the wave impedance approach will be modified to account for the variable time delay [14], and methods of countering the effects of increased wave impedance will be investigated. Use of high bandwidth force sensing is currently being incorporated into the controller to increase the fidelity of the haptic interface.

## Acknowledgements

## References

[1] Richard J. Adams and Blake Hannaford. Stable haptic interaction with virtual environments. *IEEE Trans. on Robotics and Automation*, 15(3):465–474, June 1999.

[2] Grigore C. Burdea. *Force And Touch Feedback For Virtual Reality*. John Wiley and Sons, New York, 1996.

[3] C. Carignan and D. Akin. Using robots for astronaut training. *IEEE Control Systems Magazine*, 23(2):46–59, April 2003.

[4] C.R. Carignan and K.R. Cleary. Closed-loop force control for haptic simulation of virtual environments. *The Electronic Journal of Haptics Research (http://www.haptics-e.org)*, 1(2), February 2000.

[5] John Craig. *Introduction to Robotics: Mechanics and Control, 2nd ed.* Addison-Wesley, Reading, Mass., 1989.

[6] I. Goncharenko, M. Svinin, S. Matsumoto, S. Hosoe, and Y. Kanou. Design and implementation of rehabilitation haptic simulators. In *Proc. Int. Workshop on Virtual Rehabiliation*, pages 33–39, 2003.

[7] Neville Hogan. Impedance control: An approach to manipulation. *J. of Dynamics Systems, Measurement, and Control*, pages 1–24, March 1985.

[8] R. Howe and D. Kontarinis. Task performance with a dextrous teleoperated hand system. In *Proc. of SPIE*, volume 1833, pages 199–207, 1992.

[9] T. Imaida, Y. Yokokohji, and T. Doi. Ground-space bilateral teleoperation experiment using ets-vaa robot arm with direct kinesthetic coupling. In *Proc. IEEE Int. Conf. on Robotics and Automation*, pages 1031–1038, 2001.

[10] H. I. Krebs, N. Hogan, W. Hening, S. Adamovich, and H. Poizner. Procedural motor learning in parkinsons disease. *Experimental Brain Research*, (141):425–437, 2001.

[11] C. A. Lawn and B. Hannaford. Performance testing of passive communication and control in teleoperation with time delay. In *Proc. IEEE Int. Conf. on Robotics and Automation*, pages 776–783, 1993.

[12] G. Niemeyer and J.-J. Slotine. Designing force reflecting teleoperators with large time delays to appear as virtual tools. In *Proc. IEEE Int. Conf. on Robotics and Automation*, pages 2212–2218, 1997.

[13] G. Niemeyer and J.-J. Slotine. Using wave variables for system analysis and robot control. In *Proc. IEEE Int. Conf. on Robotics and Automation*, pages 1619–1625, 1997.

[14] G. Niemeyer and J.-J. Slotine. Towards force-reflecting teleoperation over the internet. In *Proc. IEEE Int. Conf. on Robotics and Automation*, pages 1909–1915, 1998.

[15] Patrick Swaim, C. Thompson, and P. Campbell. The Charlotte intra-vehicular robot. Technical Report N95-23703, NASA, 1995.

[16] H. Yano and H. Iwata. Cooperative work in virtual environment with force feedback. In *Proc. 7th Int. Conference on Artificial Reality and Tele-existence (ICAT'97)*, pages 203–210, 1995.

# Cooperative control of virtual objects using haptic teleoperation over the internet

A P Olsson[1], C R Carignan[2] and J Tang[3]

[1]Department of Electrical Engineering, Royal Institute of Technology,
Valhallavägen 79, Stockholm, SWEDEN

[2,3]Imaging Science and Information Systems Center, Georgetown University,
2115 Wisconsin Ave. NW, Suite 603, Washington, DC, USA

[1]*pontuso@kth.se*, [2]*crc32@georgetown.edu*, [3]*jt96@georgetown.edu*

*www.visualization.georgetown.edu/inmotion2.htm*

## ABSTRACT

The feasibility of performing remote assessment and therapy of patients over the internet using robotic devices is explored. Using a force feedback device, the therapist can assess the range of motion, flexibility, strength, and spasticity of the patient's arm grasping a similar robotic device at a remote location. In addition, cooperative rehabilitation strategies can be developed whereby both the patient and therapist cooperatively perform tasks in a virtual environment. To counter the destabilizing effects of time delay in the force feedback loop, a passive wave variable architecture is used to encode velocity and force information. The control scheme is validated experimentally over the internet using a pair of InMotion2 robots located 500 miles apart.

## 1. INTRODUCTION

Robots have been explored as possible rehabilitation aids in laboratory settings for well over a decade. These investigations have recently expanded into the field of "teletherapy" whereby a clinician can interact with patients in remote locations using robotic devices. However, time delays encountered in the force feedback loop can cause instability in the system. Compensating for the time delay will be key to realizing this technology over the internet and is a cornerstone of the control architecture presented here.

The specific aims of our research are twofold: to enable a clinician to assess the physical condition of a patient's arm using metrics such as strength, dexterity, range of motion, and spasticity; and to help a clinician perform cooperative rehabilitative tasks with a patient using a virtual environment intended to simulate active daily living (ADL) tasks. The use of a "haptic" (force-feedback) device in conjunction with a video display will allow the clinician to remotely assess the patient's condition as well as assist the patient while performing rehabilitation tasks. The ISIS Center at Georgetown University Medical Center has recently assembled a robot rehabilitation test bed consisting of a pair of InMotion2 (IM2) robots from Interactive Motion Technology, Inc. (Krebs et al, 2001). The IM2 Robot is a direct-drive, four-bar linkage with a planar workspace of 90 x 60 cm and maximum continuous force output of 30 N in each direction (see Figure 1). The handle is pinned to the distal end of the outboard link providing a third, unactuated degree of freedom. The apparent mass at the handle is only 1.33 kg making it well-suited to our dual purposes.

This article begins with a brief review of previous work on internet therapy and cooperative haptics in Section 2. The tele-assessment and cooperative rehabilitation modes are described in Section 3. The haptic controller and time-delay compensation using wave variables are outlined in Section 4. Experimental results for both operational modes implemented on the IM2 test bed are presented in Section 5. Conclusions and future research are discussed in Section 6.

## 2. PREVIOUS WORK

Telemedicine has already seen several successful demonstrations of rehabilitation robotics. A "java therapy" application was enabled using a commercial, force-feedback joystick connected to an orthopaedic splint

(Reinkensmeyer, 2001). Patients log into the website "javatherapy.com" and a physical or occupational therapist will guide them through a repetitive movement regimen intended to improve their sensorimotor skills. Such therapy has been demonstrated to be useful even several years following hemiplegic stroke.

The Rutgers Haptic Master II (RMII) was used to increase hand strength in stroke patients using teletherapy (Popescu, 2000). When the patient picks up an object such as the chess piece seen on a computer screen in Figure 2, the computer actuates the piezoelectric servo valves on the hand exoskeleton to provide resistive "grasp" forces to the hand. The remote therapist can modify this resistance during the sessions to increase the patient's strength and also design an increasing complex array of virtual tasks for the patient to perform to further challenge their motor skills. Pilot clinical trials on post-stroke patients have indicated hand mechanical work increase using the RMII (Burdea, 2001).
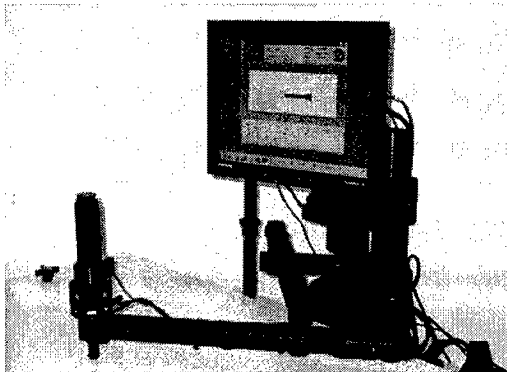


**Figure 1.** *InMotion2 Robot with graphic display of virtual beam task.*

**Figure 2.** *Rutgers Haptic Master being used to reflect grasp force during virtual chess match.*

Cooperative control using haptic devices has been attempted on several virtual reality platforms. A pair of 2-DOF master manipulators was used to simulate thumb and index fingertip contact with an object during a peg-in-hole insertion task (Howe and Kontarinis, 1992; Burdea, 1996). Dual-arm contact with a steering wheel was simulated using a pair of 6-DOF PHANToM devices for arm motor control training (Goncharenko et al, 2003). Yano and Iwata (1995) used a pair of 6-DOF, parallel mechanism force displays to perform interactive patient-therapist tasks over the internet. Although predictive displays were used to help operators adjust for up to 3 sec delays, explicit time-delay compensation was not implemented.

Several investigators have incorporated explicit time-delay compensation in the force-feedback loops of haptic systems. Scattering theory was explored by Lawn and Hannaford (1993) to produce passive communications during teleoperation of a metal block. Wave variables were introduced by Niemeyer and Slotine (1997) for a variety of master/slave scenarios with widely varying time delay. Adams and Hannaford (1999) also considered time-delay in their passivity control formulation of stable interaction with virtual environments. However, none of the investigations we encountered considered time-delay compensation in the context of multiple haptic displays.

## 3. OPERATING MODES

The robot test bed has two operating modes: Tele-Assessment and Cooperative Rehabilitation. In Tele-Assessment Mode, the clinician attempts to evaluate various properties of the patient's arm through bilateral manipulation over the internet. In Cooperative Rehabilitation Mode, the patient and therapist cooperatively manipulate common objects over the internet by moving their robot handles to accomplish a therapeutic task. Both modes are described in detail below.

### 3.1 Tele-Assessment Mode

In this mode, the robot handle that is being grasped by the subject mirrors movements made by the clinician's robot and vice versa. A force sensor on the patient's robot relays forces exerted by the subject back to the clinician's robot where the force pattern will be "displayed" on the haptic interface. This position-based "force-reflection" is commonly used today in robot-assisted surgery.

The system block diagram for assessment mode is shown in Figure 3 and is similar to the bilateral force feedback architecture used in master/slave teleoperation. Both the master and slave are under Cartesian PD control where the position of the master becomes the desired position of the slave, and the position of the

slave becomes the desired position of the master (same holds for velocity). The position and velocity data for each robot is "packetized", sent across the internet using an internet socket, and picked up by a communication process at the other side where it is unpacked and used by the local controller.

Since the PD controller filters out high frequency content from the patient's arm that might be useful for patient assessment, a force-sensor capable of picking up high frequency phenomena such as hand tremor was used to augment the haptic display. The force sensor output is high-pass filtered and transferred alongside the position/velocity data to the therapist's robot where it is amplified by a gain k and added to the PD control input. The high pass filter is necessary to remove bias readings normally present in the force sensor that would otherwise cause a position offset (Murphy, 1994).
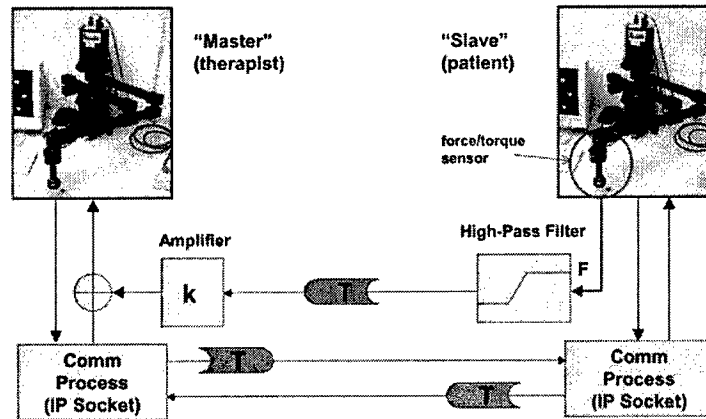
**Figure 3.** *Bilateral Tele-Assessment Mode Architecture.*

### 3.2 Cooperative Rehabilitation Mode

The control architecture for the cooperative task is shown in Figure 4. In this scenario, both the therapist and patient robots are considered "masters" which are independently interacting with the virtual object which is considered the "slave". The virtual object generator (VOG) applies the sensed "interaction" forces from the masters and then calculates the resultant motion of the object. The motion of the object at each "contact" point is then transmitted back to each master where it is tracked by a controller.

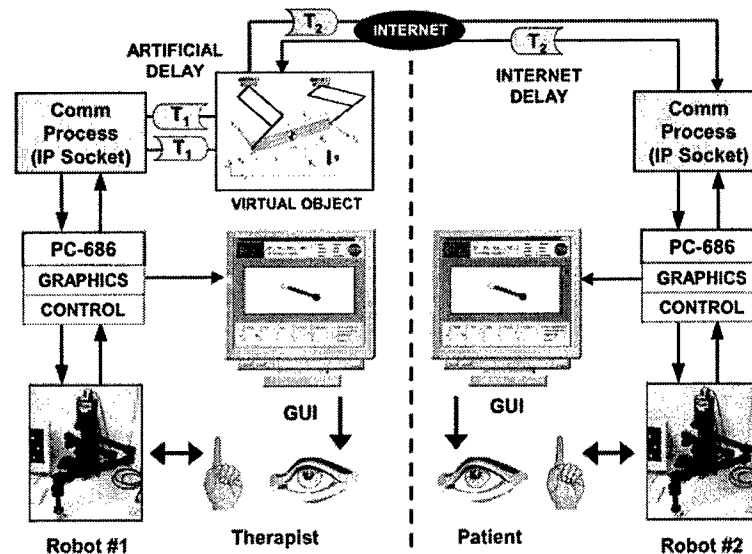**Figure 4.** *Hardware configuration for Cooperative Rehabilitation Mode.*

The virtual object dynamics are calculated via a separate process on one of the master arm computers. $T_1$ and $T_2$ are time delays caused by either internet transit or computational processing. If the object dynamics are being calculated on the master 1 computer, then $T_1$ is primarily the computational delay for the VOG process

(essentially zero), and $T_2$ is the internet time delay for a signal to reach master 1 from master 2. However, to maintain a truly cooperative task, the two time delays should be matched. Therefore, an artificial time delay based on a moving average of the internet time delay is applied to the master control computer hosting the virtual object process (master 1 in this case).

## 4. HAPTIC CONTROL AND TIME DELAY COMPENSATION

In both operating modes, the core of the haptic controller is a Cartesian PD controller that servos on the position and velocity of the handle

$$F_c = B_m(\dot{x}_{md} - \dot{x}_m) + K_m(x_{md} - x_m) \qquad (1)$$

where $x_m$ is the position of the handle, $F_c$ is the commanded Cartesian force, and $B_m$ and $K_m$ are diagonal damping and stiffness gains, respectively. For the cooperative mode, an additional force loop wraps around the servo loop as shown in Figure 5 to provide compliance (Carignan and Cleary, 2000). For the cooperative mode realization shown in Figure 6, the "sensed" human forces applied at each handle are used as the force inputs to the virtual object dynamics to generate the motion command inputs to each master.
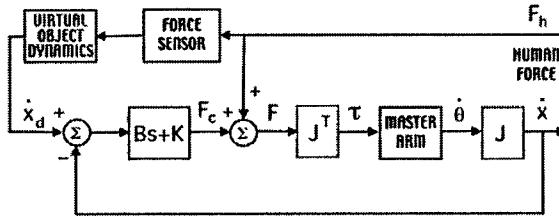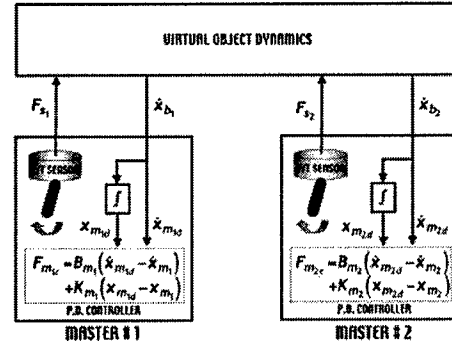


**Figure 5.** *Admittance controller block diagram (above).*

**Figure 6.** *Cooperative Rehabilitation Mode architecture using admittance control (right).*

The haptic controller works well for the interconnected robot configurations shown in Figures 3 and 4 as long as the roundtrip time delay is under about 100 msec. As the time delay starts to exceed 100 msec, the passivity of the controller becomes severely compromised and can drive the system unstable. To restore passivity in the system, compensation using wave variables emerged as the most natural approach for performing cooperative tasks over the internet (Niemeyer and Slotine, 1998).

The wave variable architecture for the cooperative mode is shown in Figure 7. The strategy is similar for tele-assessment mode except that the second master, rather than the virtual object, is the "slave". Instead of using the sensed force to impart force commands to the slave, force and velocity data are used by the master to generate an impedance "wave" command that is transmitted and decoded by the slave side into a force command for cooperative rehabilitation mode or a velocity command for tele-assessment mode. Part of the incoming wave is subsequently reflected back to the master. How much of the wave is reflected depends upon the impedance of the slave; a yielding environment will not reflect the incoming wave as greatly as a rigid wall. The wave impedance b is a tuning parameter used to trade-off speed and force; a high b produces an inertially dominant system, and a low b presents a more rigid interface (Niemeyer and Slotine, 1997b).

Each force to be "applied" to the slave is computed from the transmitted wave variable from the master using

$$F_s = -b\dot{x}_s + \sqrt{2b}\,u_s \qquad (2)$$

where the incoming wave to the slave $u_s(t)$ is the delayed output wave from the master, $u_m(t-T)$. After the virtual object dynamics are computed, the virtual object generator emits its outgoing wave variable using

$$v_s = \frac{b\dot{x}_s - F_s}{\sqrt{2b}} \qquad (3)$$

where the incoming wave to the master $v_m(t)$ is the delayed output wave from the slave, $v_s(t-T)$.

The desired master velocity, $dx_{md}/dt$, is computed from the master force $F_m$ and return wave variable $v_m$ as follows. The outgoing wave from the master is

$$u_m = \frac{b\dot{x}_{md} + F_m}{\sqrt{2b}} \tag{4}$$

If the master force command $F_c$ is used to compute the master force in (4), then $F_c = -F_m$ and Eq (1) and Eq (4) form a recursive loop (Niemeyer and Slotine, 1997). Substituting Eq (1) into Eq (4) and solving for $dx_{md}/dt$ gives

$$\dot{x}_{md} = \frac{\sqrt{2}bv_m + B_m\dot{x}_m + K_m(x_m - x_{md})}{B_m + b}$$

$$x_{md} = \int_0^1 \dot{x}_{md}(\tau)d\tau \tag{5}$$

Note that the wave impedance for both masters was chosen to be the same since the time delays were matched and the devices were identical.

The effect of an increase in time delay on the wave variable implementation is to decrease the system's natural frequency. The "communications stiffness" $K_{comm}$ is given by $b/T_{delay}$, thus the wave impedance should be increased in proportion to the time delay to maintain system bandwidth (Niemeyer and Slotine, 1997). However, the time delay also introduces an apparent mass proportional to delay, $M_{comm} = bT_{delay}$, which produces a heavier feel at the handle as the time delay (or wave impedance) increases. Thus, a trade-off exists in wave impedance between maintaining high system bandwidth and low inertia at the handle.
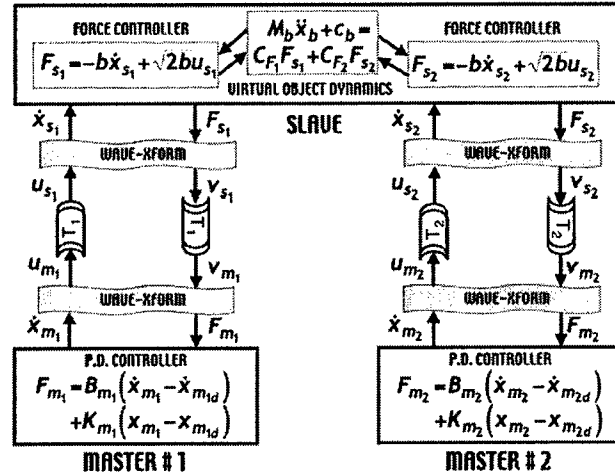


**Figure 7.** *Wave variable control architecture.*

## 5. EXPERIMENTAL RESULTS

The control station and haptic controller operate on an AMD XP1800 PC with Athlon 686 processor running at 1533 MHz. The control process was implemented in RT-Linux and uses approximately 1.2% of the CPU time at a rate of 200 Hz. Fast internet communication between robots was achieved using UDP protocol which enabled transfer rates of 100 Hz for 16 byte datasets. A 3rd-order Butterworth filter with a 5 Hz cut-off was used for the high-pass filter in the assessment tests (Fisher, 1999). The time delay for the therapist's computer, $T_1$, was set equal to the internet time delay $T_2$ in the rehabilitation tests to maintain symmetry between the VOG and each robot.

### 5.1 Tele-Assessment

As a demonstration of the utility of the high bandwidth force feedback in assessment mode, an experiment was conducted in which an operator used the master robot to move the slave robot along the vertical edge of a spiral bound notebook as shown in Figure 8. The operator tried to maintain a constant normal force as the handle moved along the edge. Figure 9 shows the total force command for the master robot in the x-direction, $F_c$, superposed on just the PD control input force for a force gain of k=5. The ripple in $F_c$ was due to the force sensor picking up the "tremor" caused by the spiral edge which was totally missed by the PD controller which had a bandwidth of approximately 5 Hz.
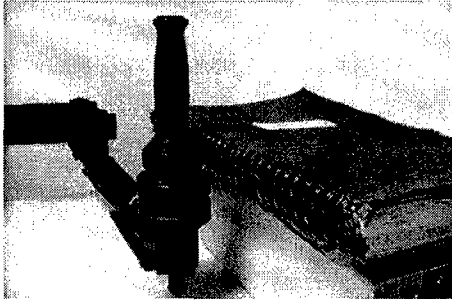
**Figure 8.** *Detecting the rough edge of a spiral notebook during tele-assessment test.*
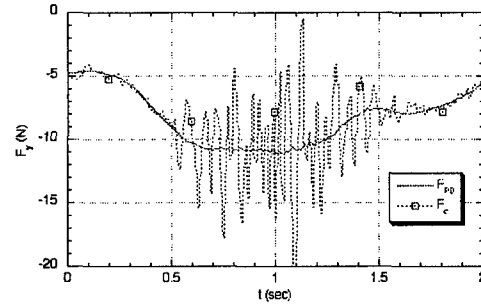


**Figure 9.** *Total force command (F_c) and PD component (F_{PD}) in x-direction for gain of k=5.*

## 5.2 Cooperative Rehabilitation

An example of a cooperative rehabilitation task is depicted in Figure 10. The patient and therapist "pick up" opposite ends of a virtual beam by grasping the handle which coincides with the end of the beam. Object parameters such as mass, length, and inertia can be adjusted to correspond to real-life objects using a Graphical User Interface (GUI) on the therapist's computer. The gravity vector points in the sagital plane of the operator so that s/he is pushing away when lifting the beam (toward the screen in Figure 1). As the object is "lifted", the side that is lower will begin to feel more of the weight thus stimulating the participants to maintain the beam in a horizontal position. Also, if one side tugs on the object, the other side feels it thus encouraging a cooperative strategy to lift the object.

The VOG calculates the dynamics of the virtual object being manipulated by the master arms. The centre of mass of the beam is chosen to be at the geometric centre, and the beam is assumed to be a uniform slender rod so that the inertia about its centre of mass is given by $i_b = m_b L^2/3$. The orientation of the beam with respect to the $x_0$-axis is given by $\theta_b$ and the total length of the beam is 2L. The resulting beam dynamics are given by

$$M_b(x_b)\ddot{x}_b + c_b(x_b,\dot{x}_b) = C_{F_1}F_1 + C_{F2}F_2 + m_b a_g \tag{6}$$

where the gravitational acceleration vector is $a_g=[0\ {-}g\ 0]^T$. The complete dynamics for Eq (6) can be found in (Carignan and Olsson, 2004).
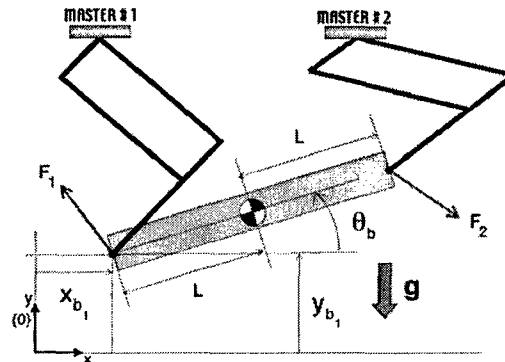


**Figure 10.** *Cooperative beam manipulation task.*

Three sets of experiments were performed to illustrate the cooperative beam manipulation task over the internet: admittance control with negligible delay, wave variable control for an actual internet test, and wave variable control for simulated internet roundtrip time delays of 0.5 and 1 sec. In all tests, the master controller had a bandwidth of 30 rad/sec and was critically damped yielding gains of $K_m=900$ N/m and $B_m=60$ N/m/s. The beam parameters were $m_b=10$ kg, L=0.15 m, and $i_b=0.075$ kg-m$^2$. A reduced gravitational acceleration of g=3 m/s$^2$ was used in order not to exceed the force capacity of the robot. Parameters could be changed by the operator using the graphical user interface shown previously in Figure 1.

In the first set of tests, the robots were colocated at the ISIS Center and the admittance control scheme of Figure 6 was used. The control and communication rates were 200 Hz, and the time delay within our own IP domain was only 0.15 msec. The beam starts out horizontally and then is lifted by the haptic master on the

left until it reaches the vertical position. Then the second haptic master raises the right side of the beam until it is again horizontal. The plot of the beam angle $\theta_b$ versus time is shown in Figure 11.

The plots of the commanded vertical forces on the beam (sensed master forces) are shown in Figure 12. $F_y$ for haptic master 1 is seen to go to zero when the beam reaches a vertical position while haptic master 2 sustains the full load of the beam. After master 2 raises its side of the beam, the force becomes equally distributed again. The desired versus actual velocities for master 1 (not shown) indicate very good tracking by the PD controller.
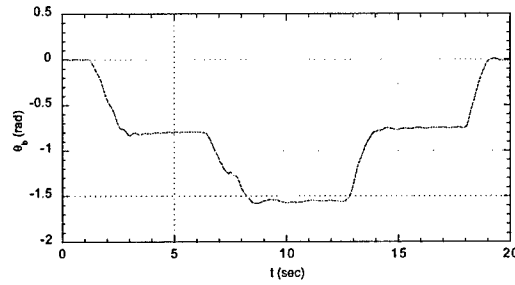


**Figure 11.** *Beam angle for zero time-delay test.*
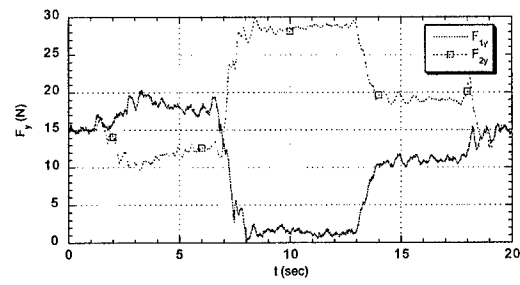


**Figure 12.** *Vertical force applied in zero delay test.*

In the second set of tests, the wave variable control scheme of Figure 7 was used. The controller rate was decreased to 100 Hz due to the bandwidth limitation of the communication process, and the wave impedance parameter b was set to 40 to compensate for the additional delay. The roundtrip internet time delay between Georgetown University and Cambridge, Mass. for this test varied between 35 and 110 msec and averaged about 50 msec. A 10 sec window was used to compute a moving average for the artificial delay $T_1$ to be applied to master 1.

The beam was manipulated in the same manner as before yielding the beam angle $\theta_b$ shown in Figure 13. The commanded master and slave forces in the y-direction for the two haptic masters are shown in Figure 14 and look remarkably similar to the zero-delay test. $F_y$ for both masters starts out equal and then goes to zero for master 1 when the beam reaches a vertical position and master 2 sustains the full load of the beam.
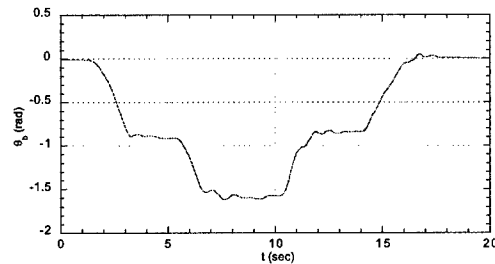


**Figure 13.** *Beam angle for internet test (b=40).*
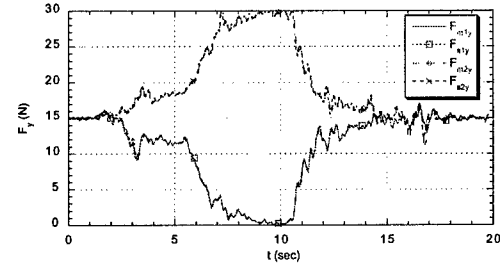


**Figure 14.** *Vertical force command for internet test.*

To demonstrate the feasibility of the wave variable approach for longer time delays, an internet delay simulator was used to generate 0.5 sec and 1 sec roundtrip time delays as shown in Figures 15 and 16, respectively. The decrease in system stiffness from the internet test is evidenced by the lower frequency oscillations. In addition, the apparent mass at the handle increases from approximately 0.5 kg for a 50 ms roundtrip delay to 10 kg and 20 kg for roundtrip delays of 0.5 and 1 sec, respectively. The heavier feel of the handle also made it more difficult for the operator to control contributing further to the degradation.
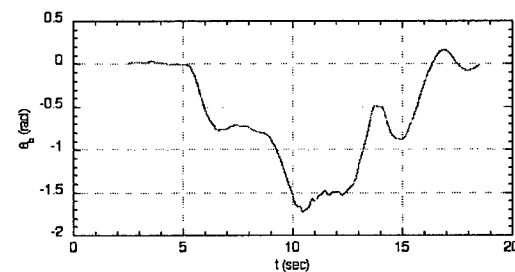


**Figure 15.** *Beam angle for 0.5 sec time delay test.*
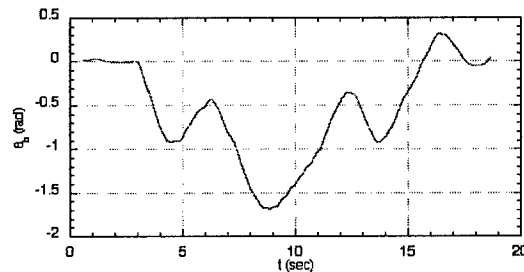


**Figure 16.** *Beam angle for 1 sec time delay test.*

# 6. CONCLUSIONS

Internet experiments conducted thus far indicate the feasibility of conducting both remote assessment and cooperative rehabilitation over the internet using robotic devices. During a cooperative internet task between robots 500 miles apart, time-delays of up to 110 ms produced borderline instability without compensation. However, under wave variable control, the system was robust to time-delays, and there was an almost imperceptible increase in the apparent mass of the handle. Packet loss was found to be less than 1% at transfer rates of 100 Hz when using UDP transmission.

We are currently testing even larger time-delays and examining several other cooperative tasks such as rowing and air hockey. We are also engaged in a cooperative effort with the National Rehabilitation Hospital in Washington, DC to test stroke patients over the internet and apply standard metrics for assessment. In addition, a head-mounted display and tracker are being integrated into the system to allow for more realistic simulations using 3D visualization. Coordination of the haptic and visual feedback in the simulator (stereopsis) is an area of ongoing research as are strategies for dealing with packet loss during less reliable transmission.

# 7. REFERENCES

R Adams and B Hannaford (1999), Stable haptic interaction with virtual environments, *IEEE Trans. on Robotics and Automation*, 15(3), pp 465-474.

G Burdea (1996), *Force And Touch Feedback For Virtual Reality*, John Wiley and Sons, New York.

C Carignan and K Cleary (2000), Closed-Loop Force Control for Haptic Simulation of Virtual Environments, *The Electronic Journal of Haptics Research* (http://www.haptics-e.org), 2(2), pp. 1-14.

C Carignan and P. Olsson (2004), Cooperative Control of Virtual Objects over the Internet using Force-Reflecting Master Arms, *Proc. IEEE Int. Conf. on Robotics and Automation*, New Orleans, pp. 1221-1226.

J Craig (1989), *Introduction to Robotics: Mechanics and Control, 2nd ed.*, Addison-Wesley, Reading, Mass.

T. Fisher (1999), Interactive Digital Filter Design, http://www-users.cs.york.ac.uk/~fisher/mkfilter/

I Goncharenko, M Svinin, S Matsumoto, S Hosoe and Y.Kanou (2003), Design and implementation of rehabilitation haptic simulators, *Proc. Intl. Workshop on Virtual Rehabilitation*, Rutgers, pp. 33-39.

R Howe and D Kontarinis (1992), Task performance with a dextrous teleoperated hand system, *Proc. of SPIE*, 1833: pp. 199-207

H I Krebs, N Hogan, W Hening, S Adamovich and H Poizner (2001), Procedural motor learning in parkinsons disease, *Experimental Brain Research*, 141: pp. 425-437.

C Lawn and B Hannaford (1993), Performance testing of passive communication and control in teleoperation with time delay, *Proc. IEEE Intl. Conf. on Robotics and Automation*, Atlanta, pp. 776 –783.

S Murphy and D Robertson (1994), Construction of a high-pass digital filter from a low-pass digital filter. *Journal of Applied Biomechanics*. 10: 374-381

G Niemeyer and J-J Slotine (1997), Designing force reflecting teleoperators with large time delays to appear as virtual tools, *Proc. IEEE Intl. Conf. on Robotics and Automation*, Albuquerque, pp. 2212-2218.

G Niemeyer and J-J Slotine (1997b), Using Wave Variables for System Analysis and Robot Control, *Proc. IEEE Intl. Conf. on Robotics and Automation*, Albuquerque, pp. 1619-1625.

G Niemeyer and J-J Slotine (1998), Towards force reflecting teleoperation over the internet, *Proc. IEEE Intl. Conf. on Robotics and Automation*, Leuven, pp. 1909-1915.

V Popescu, G Burdea, M Bouzit, and V Hentz (2000), A Virtual-Reality-Based Telerehabilitation System with Force Feedback. *IEEE Trans. on Information Technology in Biomedicine*, 4(1), pp. 45-51.

D Reinkensmeyer (2001), Java Therapy: A Web-Based System for Mass-Delivered Movement Rehabilitation After Stroke, *Proc. of the State of the Science Conf. On Telerehabilitation*, M. Rosen and D. Lauderdale, eds., pp. 70-73, Washington, D.C.

H Yano and H Iwata (1995), Cooperative work in virtual environment with force feedback, *Proc. 7th Intl. Conf. on Artifical Reality and Tele-existence (ICAT'97)*, pp. 203-210

# Robotic rehabilitation over the internet

Robots have been explored as possible rehabilitation aids in laboratory settings for well over a decade. These investigations have recently expanded into the field of 'teletherapy' whereby a clinician can interact with patients in remote locations. However, time-delays encountered in force feedback between remotely-located rehabilitation devices can cause instability in the system, and have so far prevented widespread application over the internet.

The ISIS Center at Georgetown University Medical Center has recently assembled a robot rehabilitation testbed consisting of a pair of InMotion2 robots[1] connected over the internet (see Figure 1). The specific aims of our research are twofold: to enable a clinician to assess the physical condition of a patient's arm using metrics such as strength, dexterity, range of motion, and spasticity; and to help a clinician perform cooperative rehabilitative tasks with a patient using a virtual environment intended to simulate active daily living (ADL) tasks.

An example of a cooperative rehabilitation task is depicted in Figure 2. The patient and therapist 'pick up' opposite ends of a virtual beam by grasping the handle at the end of the robot or 'master' arm.[2] The mass parameters of the object such as mass, length, and inertia can be adjusted to correspond to real-life objects using a graphical user interface (GUI) on the robot's computer. As the object is being 'lifted', the side that is lower will begin to feel more of the weight, thus stimulating the participants to maintain the beam in a horizontal position. Also, if one side tugs on the object,



Figure 1. A researcher engages in a game of air hockey on an InMotion2 robot.

the other side feels, it thus encouraging a cooperative strategy to lift.

Time-delay compensation is key to avoiding instabilities in force-feedback interaction over a distance. In our research, the wave-variable method emerged as the most natural approach for manipulating virtual objects over the internet.[3] Instead of sending force commands directly, an impedance 'wave' command is issued by the master and then subsequently reflected by the virtual object or 'slave'. How much of the wave is reflected depends upon the impedance of the virtual object: a compliant object will not reflect the incoming wave as greatly as a rigid wall.

The robots are controlled by computers running RT-Linux and connected to the internet as illustrated in Figure 3. When controlling a patient's robot directly, a client application on

that patient's computer connects to a server on their therapist's computer. User Datagram Protocol (UDP) enabled communication speeds of up to 100 16-byte datasets per second. A virtual object generator (VOG) calculates the motion of the object resulting from the force inputs from the patient and the therapist.[4] An artificial time delay ($T^1$ in Figure 3) is introduced between the VOG process and the local controller to maintain symmetry in communication between the VOG and the two robots.

To date, we have successfully conducted the virtual beam task between Georgetown University and Interactive Motion Technology in Cambridge, Massachusetts. Internet delays of up to 110ms were observed which caused borderline stability without compensation. The wave-variable controller was found to be robust to variations in time delay, and performance degraded only gradually with increasing delay. The degradation manifests itself as a higher perceived inertia at the handle which was still quite manageable even with artificially-induced delays of over 1s.

We are currently testing even larger time delays and examining the incorporation of sensed force into the wave-variable methodology to produce higher-bandwidth feedback to the clinician. In addition, a head-mounted display and tracker are being integrated into the system to allow for more realistic simulations using three-dimensional visualization. Coordination of the haptic and visual feedback in the simulator is an area of ongoing research.
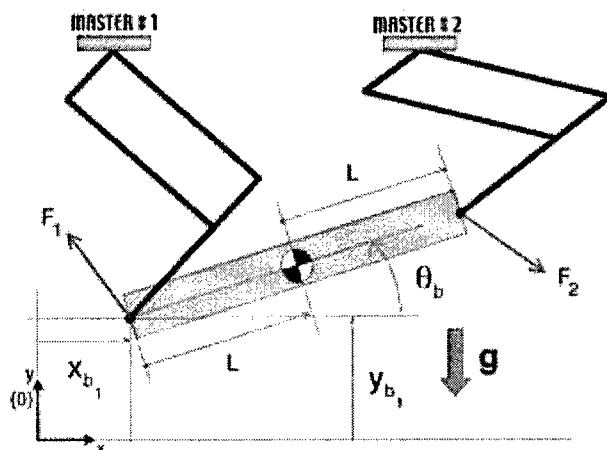
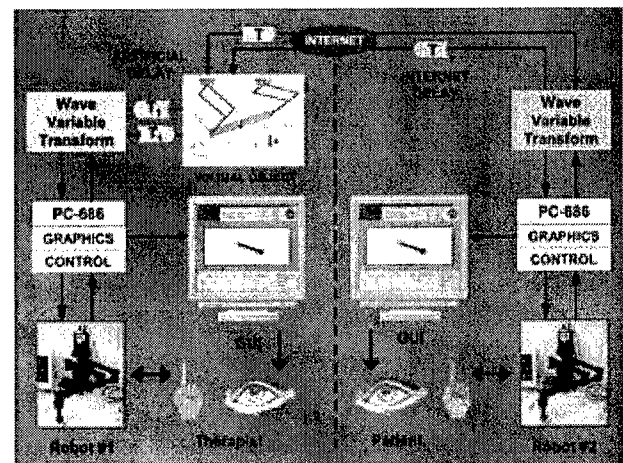Figure 2. A virtual beam task realized with two robot handles coincident with the ends of the beam.



Figure 3. System architecture for implementing a cooperative internet task.

# Enhanced haptic sensitivity in surgical telemanipulation

implementation of enhanced sensitivity in the desired stiffness range.

Figure 2 shows some experimental results, where an elastic rubber band was stretched using a one-dimensional teleoperation system. The position-force curve shows a changing slope, corresponding to a changing local stiffness. Thereby, two major areas can be assigned. At first, when the band is only slightly stretched, a stiffness of about 220N/m is detected. Further stretched, the stiffness drops to about 170N/m. The haptic device used shows clear Coulomb friction, which adds damping, but does not alter the local stiffness characteristics. The fact that the slopes of the curves in the two areas differ more at the master side than at the environment, shows how the stiffness difference between the two areas is 'blown up'. In fact, the difference is such that the areas easily can be distinguished. This enhancement of discriminability between tissues could enable surgeons to more securely define tumor boundaries, and have a higher confidence on whether crucial structures in the neighborhood are clean or in an infected zone. And, as surgeons are able to feel better, safety will increase.

**Gudrun De Gersem, Jos Vander Sloten, and Hendrik Van Brussel**
Department of Mechanical Engineering
Divisions PMA and BMGO
Katholieke Universiteit Leuven, Belgium
E-mail:
gudrun.degersem@mech.kuleuven.ac.be

**References**
1. R. Kumar, T. M. Goradia, A. C. Barnes, P. Jensen, L. L. Whitcomb, D. Stoianovici, L. M. Auer, and R. H. Taylor, *Performance of Robotic Augmentation in Microsurgery-Scale Motions,* **Springer-Verlag Lecture Notes in Computer Science 1679,** pp. 1108-1115, 1999.
2. S. E. Salcudean, S. Ku, and G. Bell, *Performance Measurement in Scaled Teleoperation for Microsurgery,* **Springer-Verlag Lecture Notes in Computer Science 1205,** pp. 789-798, 1997.
3. G. De Gersem, H. Van Brussel, and F. Tendick, *A new optimisation function for force feedback in teleoperation,* **Proc. Int'l Conf. on Computer Assisted Radiology and Surgery (CARS),** p. 1354, 2003.
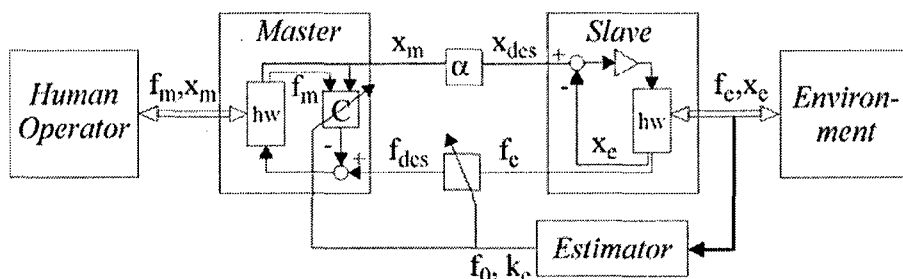


Figure 2. Experimental results on the interaction with a rubber band: the environment (grey), and the positions and forces at the interface to the human operator (black). The slope of the position-force curves denotes the local stiffness.

# Robotic rehabilitation over the internet

**Craig Carignan, A. Pontus Olsson*, and Jonathan Tang†**
Imaging Science and Information Systems (ISIS) Center
Department of Radiology
Georgetown University Medical Center
Washington, DC, USA
E-mail: {crc32, †jt96}@georgetown.edu,
*pontuso@kth.se
http://www.visualization.georgetown.edu/inmotion2.htm

**References**
1. H. I. Krebs, N. Hogan, W. Hening, S. Adamovich, and H. Poizner, *Procedural motor learning in parkinsons disease,* **Experimental Brain Research** (141), p 425-437, 2001.
2. C. R. Carignan and A. P. Olsson, *Cooperative Control of Virtual Objects over the Internet using Force-Reflecting Master Arms,* **Proc. IEEE Int'l Conf. on Robotics and Automation,** pp. 1221-1226, 2004.
3. G. Niemeyer and J. -J. Slotine, *Towards force reflecting teleoperation over the internet,* **Proc. IEEE Int'l Conf. on Robotics and Automation,** pp. 1909-1915, 1998.
4. I. Goncharenko, M. Svinin, S. Matsumoto, S. Hosoe, and Y.Kanou, *Design and implementation of rehabilitation haptic simulators,* **Proc. Int'l Workshop on Virtual Rehabilitation,** pp. 33-39, 2003.

---

# 2004   CALENDAR

submitted to American Society of Neuroradiology annual meeting,
Toronto, Canada, May 2005

## Bone Subtraction CTA Techniques for Skull Base Vascular Related Pathology: Initial Clinical Experience

Jae Choi, Dan Nguyen, and Kevin Cleary
Georgetown University Medical Center

### Purpose

Assessing bone subtraction CTA (bsCTA) technique in determining intracranial vascular pathology within and adjacent to skull base osseous structures.

### Approach/Methods

We selected patients who have possible vascular pathology at the skull base level to perform bsCTA. A non-contrast and contrast enhanced CT scans were sequentially performed with identical scanning protocols on a 4-slice Multidectector CT. A commercial software (Infinitt Rapidia , Seoul, Korea), was used to register and subtract these two acquired volumes resulting in generation of a third subtracted vessel-only volume. This subtracted volume was then imported into a dedicated 3D workstation (TeraRecon, California, U.S.A) for final multiple volumetric rendering viewings.

The bone subtraction CTA volume dataset was then compared to traditional digital subtraction angiography (DSA), the current gold standard, and 3D rotational DSA (rDSA) for image correlation.

### Findings

The appreciation of the aneurysm morphologies such overall size, neck origin, and neck size are better seen when bsCTA technique is applied to intracranial CTA. These important parameters show similar image correlation on bsCTA as they are on the 3D rDSA images.

### Conclusions

Traditional non-subtracted CTA is limited at the level of skull base where osseous structures are the predominant factor. The bsCTA technique enhances visualization of vascular pathology within this level. This subtraction technique is robust, operator non-dependent, and requires little additional post-processing effort. Most importantly, it adds additional diagnostic certainty to our noninvasive CTA armamentarium.

### Acknowledgements

**Title Page**

**Robotically Assisted Lung Biopsy under CT Fluoroscopy: Concept and Phantom Study**

**Authors:**

Kevin Cleary, PhD (corresponding author)
Filip Banovac, MD
David Lindisch, RT
Imaging Science and Information Systems (ISIS) Center
Department of Radiology
Georgetown University Medical Center
2115 Wisconsin Ave., Suite 603
Washington, DC 20007
Email: cleary@georgetown.edu
Telephone: (202) 687-8253
Fax: (202) 784-3479

Dan Stoianovici, PhD
Alexandru Patriciu, MS
Dumitru Mazilu, PhD
URobotics Laboratory
Brady Urological Institute
Johns Hopkins Medical Institutions
Baltimore, Maryland, USA

Sheng Xu, MS
Gabor Fichtinger, PhD
Russell Taylor, PhD
Engineering Research Center
Johns Hopkins University
Baltimore, Maryland, USA

Charles White, MD
Department of Radiology
University of Maryland Medical Center
Baltimore, Maryland, USA

## Abstract

**Rationale and Objectives.** To evaluate the feasibility of using a joystick-controlled robotic needle driver under CT fluoroscopy for lung biopsy in a phantom study.

**Materials and Methods.** A respiratory motion phantom incorporating cranial-caudal motion of a foam liver phantom was developed. Synthetic lesions of about 1.5 mm in diameter were created using an agar mix. CT fluoroscopy was used to visualize the motion of a lesion in and out of the scan plane. The phantom could be paused on demand for up to 30 seconds to simulate a breath hold. A joystick-controlled robotic needle driver was used by a radiologist experienced in lung biopsy to drive an 18 gauge needle on the scan plane toward the lesion.

**Results.** The radiologist was able to hit the lesion on all 20 attempts. The average time to drive the needle was 12.1 seconds with a standard deviation of 3.1 seconds. The average tube current-time product was 955 mAs with a standard deviation of 180 mAs. The average dose-length product was 92.5 mGycm with a standard deviation of 42 mGycm.

**Discussion.** A joystick-controlled robotic needle driver can be used to accurately target lesions in a respiring phantom under CT fluoroscopy. This technique may allow the radiologist to more precisely manipulate the needle with much less radiation exposure. Additional studies are planned to further automate this process and to investigate the role of robotic systems for lung biopsy in the clinical area.

# 1 Introduction

The use of CT for lung cancer screening is rapidly expanding. This screening has revealed a large number of small pulmonary nodules. Most of these nodules are benign and less than 1 cm in size. They are often dismissed as clinically irrelevant, sometimes inappropriately. Some recent reports suggest that a higher-than-previously-suspected portion of these small pulmonary nodules are malignant; for example, lung carcinoma rates of 58% were reported in a group of patients that had thoracoscopic biopsies of nodules less than 1 cm in diameter[1]. It is therefore becoming increasingly important to obtain a tissue-specific diagnosis of these small lesions.

The diagnostic accuracy of transthoracic needle biopsy (TNB) is not ideal. Yankelevitz et al. state that needle misplacement probably represents the single most common cause for a false-negative biopsy[2]. A needle trajectory misalignment of only 3 degrees over a distance of 10 cm will result in a deviation substantial enough to miss a 1 cm nodule[2]. In addition, the needle bevel causes the needle to deflect as it is advanced, and thus requires either anticipation of the degree of deviation, or repositioning of the needle placement. Although most patients with benign disease will be identified correctly, false negative diagnoses occur, usually due to sampling error[3]. Missing the lesion even by a fraction of a millimeter precludes adequate sampling[2]. Additionally, the diagnostic accuracy of TNB drops off precipitously for small nodules[4]. This problem reveals the importance of path planning under CT guidance as it is presently performed.

White et al. explain that a standard CT has several limitations that are a consequence of its lack of real-time visualization[5]. It may take multiple attempts to localize the nodule and achieve proper angulation of the needle toward the nodule. Additionally, respiratory motion may alter the anatomic relationships with respect to the nodule, and compensation can be difficult in the absence of real-time observation[5]. In the conventional CT gantry, the actual sampling of the lesion and the location of the needle tip are not observed in real-time[5], a factor that is essential for a successful biopsy[6]. Therefore, CT fluoroscopy, a relatively new modality, is gaining acceptance in image guidance for TNB.

The advent of CT fluoroscopy combines the advantages of both CT and fluoroscopy in that images can be viewed in nearly real-time[7]. Lesions with CT fluoroscopy can be accessed even if they lie in less favorable locations and are smaller in size. The procedure can also be performed more quickly and in less cooperative patients[8]. CT fluoroscopy's biggest advantage may be that the location of the needle tip can be precisely ascertained as the nodule is being aspirated, and thus, the number of needle passes can be reduced [7].

CT fluoroscopic guidance may facilitate placement of needles in the edge of larger lesions and thus avoid an equivocal biopsy of the necrotic center. Additionally, if real-time imaging in CT fluoroscopy is used, it is possible to see the needle push away the nodule (balloting) rather than pierce it. A modification in technique can be immediately

employed using a more rapid puncture to pierce the specimen[5]. There is promising preliminary experience using CT fluoroscopy for biopsies of nodules less than 1.5 cm in diameter, with diagnostic tissue obtained in 94% of the cases[5].

However, the use of CT fluoroscopy for lung biopsy and other procedures has not expanded as rapidly as one might expect. An important safety concern raised by this technology is the radiation that the radiologists' hands are exposed to during their attempts to redirect or reposition the needle[9]. Therefore, needle holders have been developed and their comparative use in CT fluoroscopy has been evaluated[10, 11]. Alternatively, another method of avoiding the primary beam is to use a surgical clamp to grasp and guide the needle in real-time[5]. However, none of these techniques would completely remove the radiologist from the ionizing radiation; moreover, manipulation and accurate alignment of a needle with an off-centered clamp or needle holder can be difficult.

To minimize the radiation exposure to the radiologist, and to provide a steady platform for needle guidance and placement, we have been experimenting with a joystick-controlled needle driver robot under CT fluoroscopy. This robot was originally developed by the Urology Robotics (URobotics) Laboratory at Johns Hopkins Medical Institutions for percutaneous renal access under fluoroscopy[12]. A more recent model of the robot was employed at Georgetown University Hospital for a clinical trial of spinal blocks[13]. A photograph of the robot is shown in Figure 1. The robot consists of a touch screen and joystick for control, a mechanical arm, a needle driver, and a mounting base[14].

This paper describes our initial investigations with this device under CT fluoroscopy in a phantom study. The purpose of the phantom study was to verify the ability of a radiologist to use the robotic needle driver to hit lesions in a synthetic lung. The long term goal of our work is to develop an integrated system for robotic lung biopsy.

## 2    Materials and Methods

The system concept is shown in Figure 2. The real-time CT fluoroscopy image is captured using a frame grabber card (Accustream 170, Foresight Imaging, Lowell, Massachusetts, USA). The frame grabber is a commercial product that occupies a spare slot in the computer backplane of the robot controller and allows the system to capture the CT images in real-time. This real-time image capture is essential for our long term goal of detecting the position of the target lesion automatically from the image. If the target lesion can be automatically detected, we can then command the robot to automatically drive the needle toward the lesion.

A picture of the experimental setup is shown in Figure 3. The study was done in the CT room at Georgetown University Medical Center using a Siemens Somatom Volume Zoom CT scanner. A custom-designed respiratory motion phantom incorporating a synthetic lung was developed for this study. The robotic needle driver was mounted on the CT table using a specially constructed mounting bracket. The bracket incorporated straps that ran under the CT table to hold the robot tight.

The respiratory motion phantom is shown in Figure 4. The phantom consists of a torso model, a rib cage taken from an anatomical bone model, a rubber like skin layer (Limbs and Things, Bristol, UK), and a synthetic lung. The synthetic lung was molded from a two-part flexible foam (FlexFoam II, Smooth-On, Easten, PA) using a plastic lung model. The respiratory motion phantom includes a one degree of freedom motion platform that simulates cranial-caudal motion and can be programmed from a laptop computer. The synthetic lung was attached to the radiolucent portion of the motion platform.

Synthetic lesions were created by mixing agar and injecting it into the lung using a syringe. This technique enabled us to control the size of the lesion with some precision. A lesion of about 1.5 cm was created as shown in Figure 5.

The robot was then positioned so that the needle was aligned with the CT scan plane (Figure 6). The respiratory motion phantom was positioned so that the lung lesion would move in and out of the scan plane. The respiratory motion phantom was activated with a respiratory rate of about 15 breaths per minute and an excursion distance of about 1.5 cm. The interventional radiologist (CW) activated the CT fluoroscopy imaging mode by stepping on the foot panel and watching the image on the in-room monitor (Figure 7). When the lung lesion moved into the scan plane, a button was pressed on the respiratory motion controller to pause the respiratory motion for up to 30 seconds, simulating a patient breath hold. The interventional radiologist then used the joystick to command the robot to drive the needle toward the lesion. A total of 20 trials were done.

## 3   Results

The results of the study are given in Table 1. The radiologist was able to hit the lesion on all 20 trials. The average time to drive the needle was 12.1 seconds with a standard deviation of 3.1 seconds. The average tube current-time product was 955 mAs with a standard deviation of 180 mAs. The average dose-length-product (DLP) as a measure for the applied radiation dose was 92.5 mGycm with a standard deviation of 42 mGycm. A CT fluoroscopy image showing the needle in the lung lesion is shown in Figure 8.

## Table 1: Study Results

| Trial number | Needle driving time  seconds | Recorded tube current  mAs | Recorded dose length product  mGycm |
|---|---|---|---|
| 1 | 22 | 1232 | 50 |
| 2 | 11.3 | 1369 | 150 |
| 3 | 14 | 1256 | 160 |
| 4 | 15 | 991 | 90 |
| 5 | 11 | 1008 | 200 |
| 6 | 13 | 1079 | 75 |
| 7 | 10.5 | 867 | 25 |
| 8 | 12 | 867 | 125 |
| 9 | 9.5 | 1085 | 75 |
| 10 | 14 | 961 | 100 |
| 11 | 8 | 743 | 50 |
| 12 | 12.5 | 932 | 70 |
| 13 | 12 | 1003 | 80 |
| 14 | 13 | 914 | 100 |
| 15 | 9 | 719 | 100 |
| 16 | 14 | 920 | 100 |
| 17 | 9 | 843 | 100 |
| 18 | 9 | 749 | 50 |
| 19 | 11 | 767 | 50 |
| 20 | 12 | 796 | 100 |
|  |  |  |  |
| Average | 12.1 | 955 | 92.5 |
| Standard deviation | 3.1 | 180 | 42 |

## 4    Discussion

Based on the study data reported here, it is feasible to use a radiologist-controlled robotic needle driver to accurately place needles during breath holds of a lung phantom with simulated respiratory motion. This discovery is a first step towards developing a fully automated robotic system for CT fluoroscopy guided lung biopsy. All 20 trials were completed without difficulty and no system failures were observed using the robot. The robot provides a steady and precise holder for the needle and is capable of keeping the needle on the CT scan plane so that the procedure can be readily visualized by the radiologist while minimizing his or her exposure to radiation.  The radiologist can view

the location and trajectory of the needle as it is directed toward the lesion in real-time, since the radiologist's hand is not near the path of the x-ray beam.

Other methods to aid in needle guidance have been proposed, such as needle holders and a CT-integrated stereotactic arm (PinPoint, Philips Medical Systems, Cleveland, Ohio). However, these methods do not give the same degree of precision and incremental motion as the actively driven robot tested here.

From the clinical perspective, the current approach to percutaneous lung biopsy procedures is largely empiric. The radiologist uses images from CT scanning to estimate the best approach to the lesion that avoids structures such as ribs and allows entrance into the lung lesion. If this estimate is incorrect and the lesion is missed, the needle tip may need to be readjusted, increasing procedure time and the risk of complications such as pneumothorax. The real-time feedback provided by CT-fluoroscopy is valuable in permitting quick adjustment of needle position but this advantage is somewhat mitigated by the need to avoid exposure of the operator's hands during the biopsy. Most radiologists currently use an "adjust and peek" approach to needle adjustment rather than directly visualizing needle movement with CT fluoroscopy. The joystick-controlled robotic needle driver obviates radiation to the radiologist and may facilitate real-time CT fluoroscopic biopsies.

The next step in our research program is to further automate the biopsy process. We have been developing an algorithm to automatically track a lesion under CT fluoroscopy and then command the robot to drive the needle to the lesion [15]. Phantom studies have been done using this algorithm and we have begun swine studies under an approved animal protocol.

## 5    Acknowledgements

## 6    References

1.    Munden, R.F., R.D. Pugatch, M.J. Liptay, D.J. Sugarbaker, and L.U. Le, *Small pulmonary lesions detected at CT: clinical importance.* Radiology, 1997. **202**(1): p. 105-10.

2.    Yankelevitz, D.F., M. Vazquez, and C.I. Henschke, *Special techniques in transthoracic needle biopsy of pulmonary nodules.* Radiol Clin North Am, 2000. **38**(2): p. 267-79.

3.  Afify, A. and R.M. Davila, *Pulmonary fine needle aspiration biopsy. Assessing the negative diagnosis.* Acta Cytol, 1999. **43**(4): p. 601-4.

4.  Yankelevitz, D.F. and C.I. Henschke, *Small solitary pulmonary nodules.* Radiol Clin North Am, 2000. **38**(3): p. 471-8.

5.  White, C.S., C.A. Meyer, and P.A. Templeton, *CT fluoroscopy for thoracic interventional procedures.* Radiol Clin North Am, 2000. **38**(2): p. 303-22, viii.

6.  Yankelevitz, D.F., C.I. Henschke, J.H. Koizumi, N.K. Altorki, and D. Libby, *CT-guided transthoracic needle biopsy of small solitary pulmonary nodules.* Clin Imaging, 1997. **21**(2): p. 107-10.

7.  Katada, K., R. Kato, H. Anno, Y. Ogura, S. Koga, Y. Ida, M. Sato, and K. Nonomura, *Guidance with real-time CT fluoroscopy: early clinical experience.* Radiology, 1996. **200**(3): p. 851-6.

8.  Shaham, D., *Semi-invasive and invasive procedures for the diagnosis and staging of lung cancer. I. Percutaneous transthoracic needle biopsy.* Radiol Clin North Am, 2000. **38**(3): p. 525-34.

9.  Kato, R., K. Katada, H. Anno, S. Suzuki, Y. Ida, and S. Koga, *Radiation dosimetry at CT fluoroscopy: physician's hand dose and development of needle holders.* Radiology, 1996. **201**(2): p. 576-8.

10. Daly, B., P.A. Templeton, T.L. Krebs, K. Carroll, and J.J. Wong-You-Cheong, *Evaluation of biopsy needles and prototypic needle guide devices for percutaneous biopsy with CT fluoroscopic guidance in simulated organ tissue.* Radiology, 1998. **209**(3): p. 850-5.

11. Irie, T., M. Kajitani, K. Matsueda, Y. Arai, Y. Inaba, Y. Kujiraoka, and Y. Itai, *Biopsy of Lung Nodules with Use of I-I Device Under Intermittent CT Fluoroscopic Guidance: Preliminary Clinical Study.* J Vasc Interv Radiol, 2001. **12**(2): p. 215-219.

12. Cadeddu, J.A., D. Stoianovici, R.N. Chen, R.G. Moore, and L.R. Kavoussi, *Stereotactic mechanical percutaneous renal access.* J Endourol, 1998. **12**(2): p. 121-5.

13. Cleary, K., V. Watson, D. Lindisch, A. Patriciu, D. Mazilu, and D. Stoianovici. *Robotically assisted interventions: clinical trial for spinal blocks.* in *Medical Image Computing and Computer-Assisted Intervention (MICCAI).* 2003.

14. Stoianovici, D., K. Cleary, A. Patriciu, D. Mazilu, A. Stanimir, N. Craciunoiu, V. Watson, and L.R. Kavoussi, *AcuBot: a robot for radiological interventions.* IEEE Transactions on Robotics and Automation, 2003. **19**(5): p. 927-930.

15. Xu, S., G. Fichtinger, R.H. Taylor, and K.R. Cleary. *3D motion tracking of pulmonary lesions using CT fluoroscopy images for robotically assisted lung biopsy.* in *Proc. SPIE Vol. 5367, p. 394-402, Medical Imaging 2004: Visualization, Image-Guided Procedures, and Display; Robert L. Galloway, Jr.; Eds.* 2004.

**Figure Captions**

Figure 1: Robot showing touch screen, translational mechanism, and needle driver end-effector

Figure 2: System concept for robotic lung biopsy

Figure 3: Experimental setup showing robot, phantom, and needle on scan plane

Figure 4: Respiratory motion phantom with motor at left end and lung at right end

Figure 5: Axial CT image of agar injection to create synthetic lesion in lung
(lesion size is 1.44 cm as measured on the screen)

Figure 6: Close-up view showing robot, phantom, and needle held on CT scan plane
(note red laser light from CT scanner)

Figure 7: Radiologist watching monitor and manipulating robot with joystick

Figure 8: Axial CT image of needle in lung lesion

**Figure 1: Robot showing touch screen, translational mechanism, and needle driver end-effector**



**Figure 2: System concept for robotic lung biopsy**

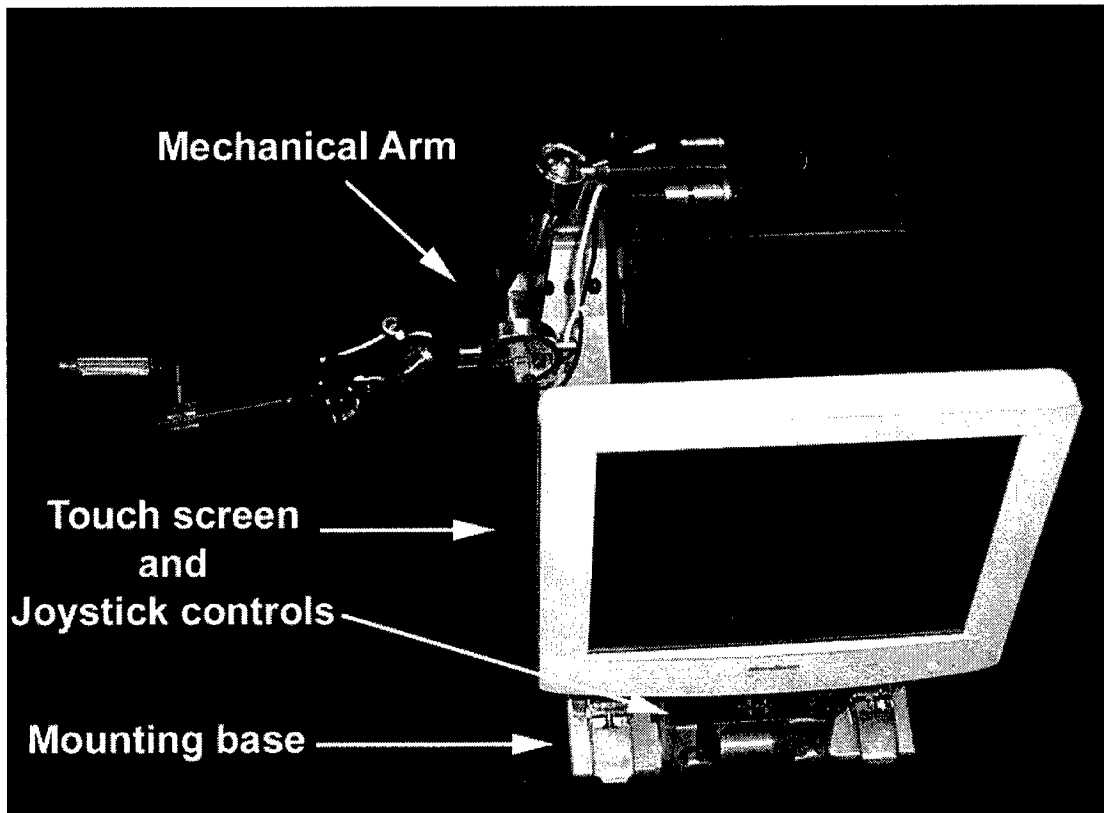**Figure 3: Experimental setup showing robot, phantom, and needle on scan plane**



**Figure 4: Respiratory motion phantom with motor at left end and lung at right end**

**Figure 5: Axial CT image of agar injection to create synthetic lesion in lung (lesion size is 1.44 cm as measured on the screen)**
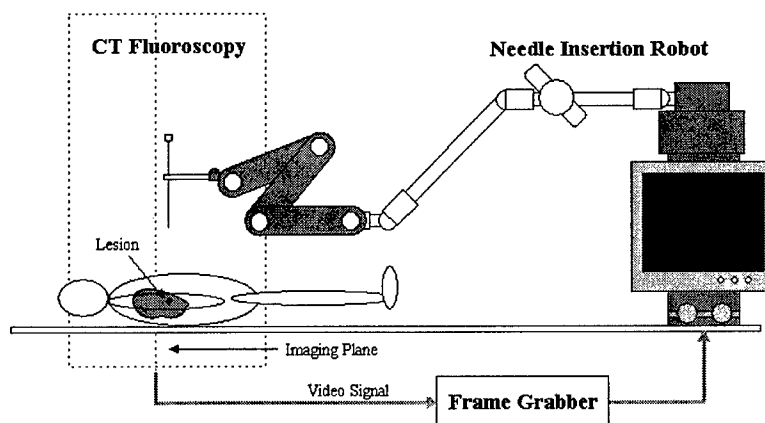


**Figure 6: Close-up view showing robot, phantom, and needle held on CT scan plane (note red laser light from CT scanner)**

**Figure 7: Radiologist watching monitor and manipulating robot with joystick**
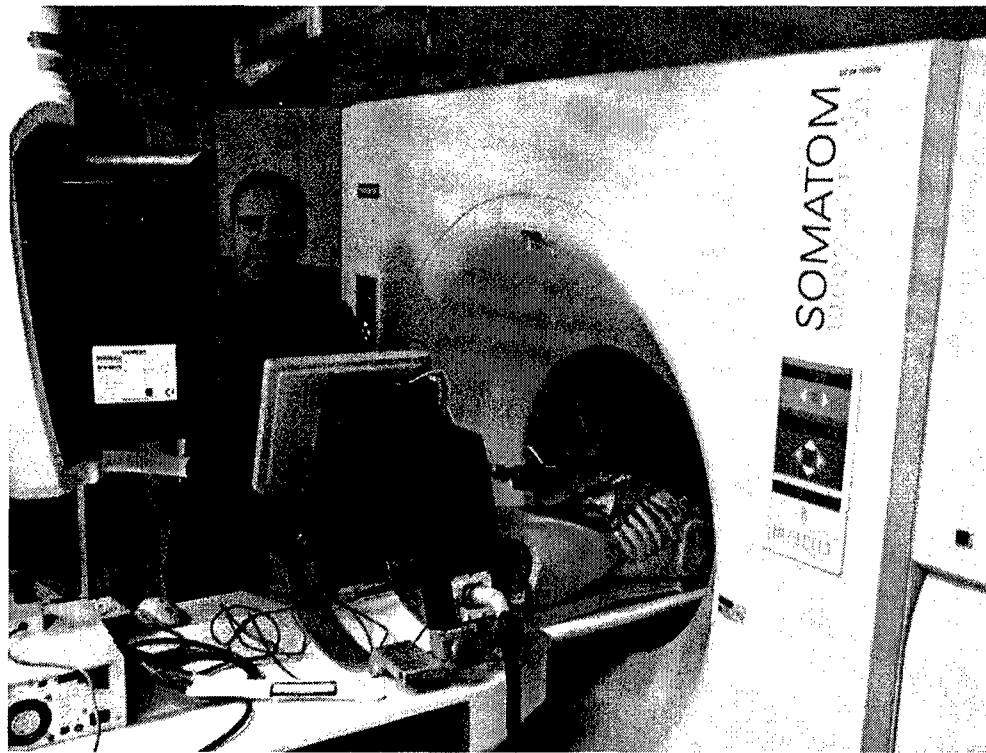


**Figure 8: Axial CT image of needle in lung lesion**

# Needle targeting under C-Arm fluoroscopy servoing

Cristian Mihăescu[a,c], Luis Ibanez[b], Mihai Mocanu[c], Kevin Cleary[a*]

[a]Imaging Science and Information Systems (ISIS) Center, Department of Radiology,
Georgetown University, Washington, D.C., USA
[b]Kitware Inc., Albany, NY, USA
[c]Software Engineering Department, University of Craiova, Romania

## ABSTRACT

This paper describes a method for translational and orientational alignment of a robotic needle driver based on image servoing and x-ray fluoroscopy. The translational process works by segmenting the needle in a frame-grabbed fluoroscopic image and then commanding the robot to automatically move the needle tip to the skin entry point. The orientational alignment is then completed based on five different positions of the needle tip. Previously reported fluoroscopy servoing methods use complex robot-image registration algorithms, fiducial markers, and two or more dissimilar views that included moving the fluoroscope. Our method aligns the needle using one setting of the fluoroscope so that it does not need to be moved during the alignment process. Sample results from both the translational and orientational steps are included.

Keywords: fluoroscopy servoing, needle driver robot, needle segmentation, medical robotics

## 1. INTRODUCTION

Minimally invasive procedures are becoming more widespread because they reduce patient trauma and improve recovery time. To successfully perform these procedures, physicians need as much visualization information as possible. This visualization is typically achieved through different imaging techniques, including ultrasound, fluoroscopy, MRI, and CT.

We have recently employed a robotic arm to assist physicians in needle placement for minimally invasive spine procedures.[1] The robot is controlled by the physician using a joystick and thus enables the physician to view a fluoroscopy image in real-time while manipulating a needle. The next step in further automating this procedure is to automatically align the needle with respect to the target based on feedback from the image.

This targeting technique is called "fluoroscopy servoing" and has been explored by just a few researchers. Previous methods have used complex algorithms for robot-image registration and two or more dissimilar views. Our approach is "uncalibrated" and uses a two-phase approach, one for translation and one for orientation. The goal of the translation stage is to place the tip of the needle on to the line of sight that passes through the target. After this step is accomplished, the needle is aligned with the line of sight that passes through the target. This paper presents a new technique for aligning the needle with the target.

Two related problems in visual servoing are robustness and stability, both of which are highly desirable in medical procedures. A lack of robustness results primarily from inappropriate detection or segmentation of the target or the interventional device, such as the surgical needle.

The stability of visual tracking is highly dependent on the ability of the algorithm to process the visual information quickly enough (in real-time). Often a dynamic system model of target motion is used to estimate the target location

---

* cleary@georgetown.edu; Telephone 1-202-687-8253; Fax 1-202-784-3479

within the image and a region of interest (ROI) is used to reduce the amount of image data processing. This technique has proven effective, provided the ROI is sufficiently large to detect the target and sufficiently small to be processed fast. The size of the ROI and the resolution of the ROI must be chosen in such a way to ensure that tracking is stable.

The main advantages of our new alignment method are speed and the fact that the C-Arm does not have to move during the alignment procedure. The speed comes from the fact that the inputs for the method are represented by five different positions of the head of the needle in one image plane. The procedure time is reduced since the C-Arm does not have to move during the alignment process.

The first attempts to perform visual servoing using X-ray fluoroscopy instead of CCD (charge-coupled device) cameras were done by Loser and Navab[2] and by Patriciu and Stoianovici.[3] All previously explored methods required at least two dissimilar views of the target. A more recent approach by Mocanu[4] required just one view for the alignment procedure. Due to the requirements of the clinical environment, these methods have to provide accuracy; usually, accurate 3D alignment of the tool with respect to an anatomic target is achieved and an estimate of the required insertion depth is offered. Also, a few earlier studies reported computer-assisted instrument targeting based on the development of specialized, complex robot-image registration algorithms. These methods involved fixed target locations and used static images of fiducial markers to estimate the robot-image coordinate mapping, which was then used for accurate targeting. In such techniques, planning paths provided satisfactory accuracy since there was no significant target position displacement. Such methods commonly used at least two images of a spatial radio-opaque marker of complex geometry or a series of one-dimensional marks distributed on a defined pattern.

All image-guided medical procedures, such as percutaneous needle access or radiofrequency ablation, require targeting of a specific instrument at an exact organ location, and the clinical outcome of these procedures relies on targeting accuracy. For this reason, fluoroscopy servoing and other automated techniques should continue to be developed for precision targeting applications. As the benefits of medical robotics become clearer, they may be more intensively used, in particular for minimally invasive procedures.

## 2. METHODS AND MATERIALS

The system described in this paper uses a needle driver robot and a camera. The robotic system consists of a radiolucent needle driver called PAKY (Percutaneous Access to the Kidney) and the RCM (Remote Center of Motion) robotic module.[5] The specialized design involved the addition of an active three degrees of freedom (3-DOF) translational stage, mounted on a bridge-like support, linked to the RCM robot by a 7-DOF passive positioning arm, and equipped with a central braking system, which can be easily manipulated at desired locations and firmly locked in a desired position.[6]

The camera simulates the C-Arm imager from the clinical environment. This system is a typical example of an image-based servoing system. Images from the camera are frame-grabbed and processed in real time on the robot controller, where all of the image processing and robot commands take place.

The whole process consists of two phases: translation and alignment. The translation process will place the tip of the needle on the line of sight that passes through the target. The alignment stage will orient the needle until it is parallel to the line of sight between the anatomical target and the projection of the target on the fluoroscopic image.

### 2.1. Translation stage

At the beginning of the translation stage, there is an arbitrary angle between the needle and the plane of the fluoroscopic image. The anatomical target is visible in the image field of view and the needle tip is located at an arbitrary distance from the anatomical target. The distance between the needle tip and the target is nevertheless expected to be small, in the range of a couple centimeters, to be precise.

The initial geometrical configuration of the system is illustrated in Figure 1. The coordinates (x,y) define the plane in which the robot arm can be translated. The coordinates (x',y') define the reference system of the fluoroscopic image

after it is acquired by the image grabber. The translation stage is used to bring the needle tip in contact with the line of sight between the anatomical target and its projection in the fluoroscopic image plane, as illustrated in Figure 2.
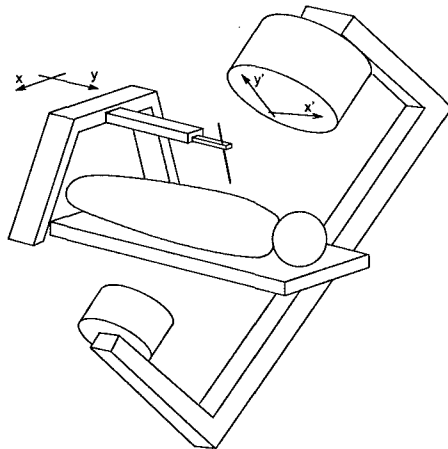


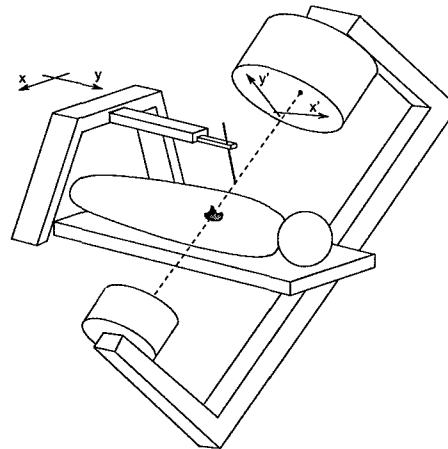Figure 1. Initial geometrical configuration        Figure 2. Configuration at the end of alignment

From the fluoroscopic image point of view, the needle tip will be in contact with the line of sight to the target when the tip is seen as overlapping the target on the image plane (Figure 2). On the other hand, when the needle tip is not touching the line of sight, this position will be seen in the fluoroscopic image as the tip being at a certain distance from the anatomical target (Figure 1), and therefore, there will be a vector **v'** relating the positions of the needle tip and the target in the (x',y') space.

In order to bring the needle into contact with the line of sight, the robot arm must be displaced in the plane (x,y). We must therefore convert the vector **v'** from the image space (x',y') into a vector **v** in the robot space (x,y). We must then find a transformation suitable for mapping (x',y') coordinates into (x,y) coordinates. In this particular geometrical configuration, that transformation can be approximated by a 2D affine transform if we ignore the perspective effect on the formation of the X-Ray image. The error introduced by this approximation is lower when the distance from the needle tip to the line of sight is small, and when the needle tip is far from the X-Ray source. A two-dimensional affine transform is fully specified by 6 coefficients. Therefore, if we know the (x,y) and (x',y') coordinates of the needle tip in at least 6 different positions, we are able to estimate the parameters of the 2D affine transform. Once we have the affine transform, we can use it in order to map the vector **v'** from the image plane into a displacement **v** in the robot plane (x,y), and to move the robot arm by the amount required to put the needle tip in contact with the line of sight.

Figure 3 illustrates the properties of the robot coordinate system (x,y) when it is mapped into the fluoroscopic image coordinate system (x',y'). An affine transform maps straight lines from (x,y) into straight lines in (x',y'). Angles from the (x,y) space are not conserved when mapped into the (x',y') space because the image plane and the robot plane are not parallel. Figure 4 illustrates the selection of 6 positions used to estimate the coefficients of the 2D affine transform. These positions are obtained by moving the robot arm in the (x,y) space by known amounts. Translations of the robot used here can be controlled with at least 0.1 mm precision. The locations of the 6 points are all obtained relative to an arbitrary origin by applying robot translations of 12 millimeters each time. Thus, we acquire 7 positions and use one of them as the coordinate system origin.

Figure 3. Robot coordinate system (x,y) projected
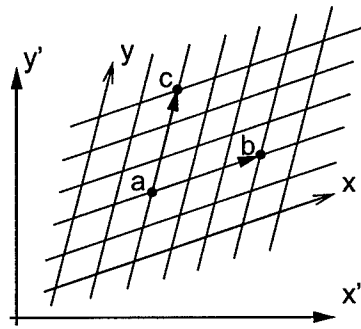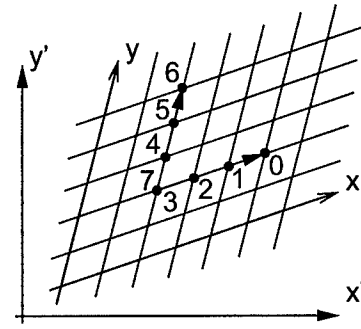onto fluoroscopic image space (x',y')



Figure 4. Positions used for affine
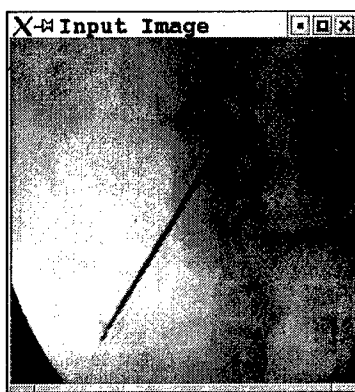transform estimation
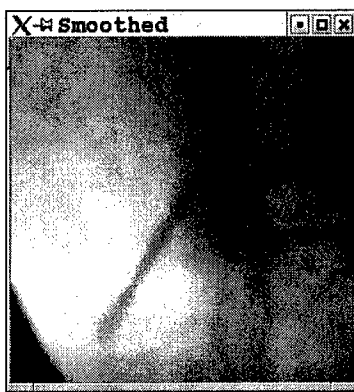


Figure 5. Input fluoroscopic image
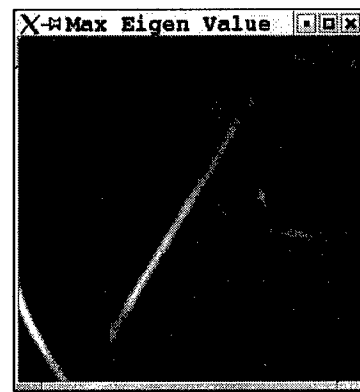


Figure 6. Gaussian smoothed
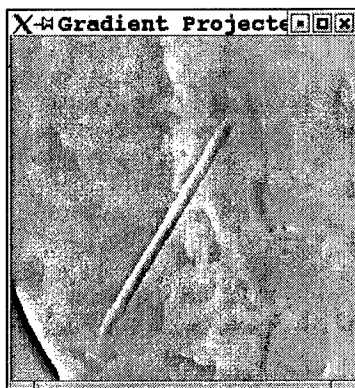


Figure 7. Maximum Eigen value



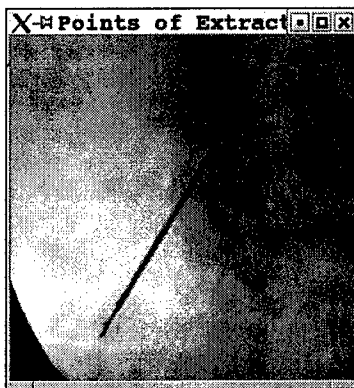Figure 8. Projection of gradient
onto the maximum Eigen vector



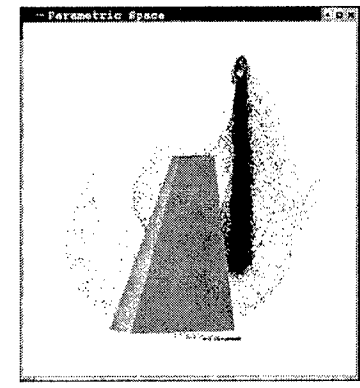Figure 9. Population of ridge
points detected



Figure 10. Parametric space for
detecting ridge points.

The positions of the needle tip in the image plane are found by segmenting the needle from the fluoroscopic images. A typical fluoroscopic image is presented in Figure 5, where the needle overlaps a section of the patient's spine.

The process used for segmenting the needle is illustrated in Figure 11. The essential aspect of this segmentation process is the detection of intensity ridge points on the fluoroscopic image. This method was implemented following the approach described in Eberly 2000[7] and Aylward 2002[8]. The image is first blurred using a Gaussian filter that produces the result shown in Figure 6. From this blurred image, first and second derivatives are computed. The matrix containing all the second derivatives of intensities at one point corresponds to the Hessian matrix of the intensity at that particular location. An Eigen analysis of the Hessian matrix leads to the detection of the direction along which the second derivative has a maximum value, as well as the value of such second derivative. This value appears as the maximum Eigen value of the Hessian matrix as illustrated in Figure 7. The scalar product of the image gradient with the principal eigenvector provides a measure of how far every pixel is from the medial line of the ridge, as illustrated in Figure 8.

A statistical pattern recognition approach is implemented by first building a 3D parametric space where a point is placed for every pixel in the image. The coordinates of the point in the parametric space are respectively the values of the pixel in the blurred image, the maximum Eigen value image, and the gradient projection image. The population of points in this parametric space is illustrated in Figure 10. Points belonging to a ridge tend to cluster together in the region represented with a green pyramid. When the image pixels associated with points in that region are highlighted in the original image, we obtain a set of ridge points, as illustrated in Figure 9. A connected components analysis is performed for this set of points with the aim of eliminating small sections of ridges that are commonly found in anatomical structures such as vertebrae. With the points belonging to the largest connected component, a line Hough transform is computed with the aim of finding the parameters of a straight line parallel to the needle in the image. This parametric line equation allows further elimination of any outliers. The remaining points are used to compute the position of the needle tip.



Figure 11. Flow diagram of the segmentation method and needle tip position estimation.

The segmentation process described above is applied 7 times in order to find each one of the needle positions illustrated in Figure 4. From those seven segmentations, six relative positions are computed and used for estimating the 2D affine transform capable of mapping the robot space (x,y) into the image space (x',y') and vice versa. The affine transform is used for converting the vector v' from the image into the vector v that must be applied to the robot arm in order to place the needle tip in contact with the line of sight as illustrated in Figure 2. After applying such translation in the robot arm, the tip of the needle coincides with the target as it is seen in the fluoroscopic image.

## 2.2. Alignment stage

In this stage, the physician positions the C-Arm to obtain a good view of the target. In this image, the tip of the needle is on the line of sight that passes through the target (as described in Section 2.1). From this point, only the orientation stage of the robot is used, to provide a remote center of motion capability. This ensures that the tip of the needle is fixed in 3D and the needle can be moved in two planes defined by the kinematics of the orientation stage. The method of aligning the needle relies on a few basic concepts.
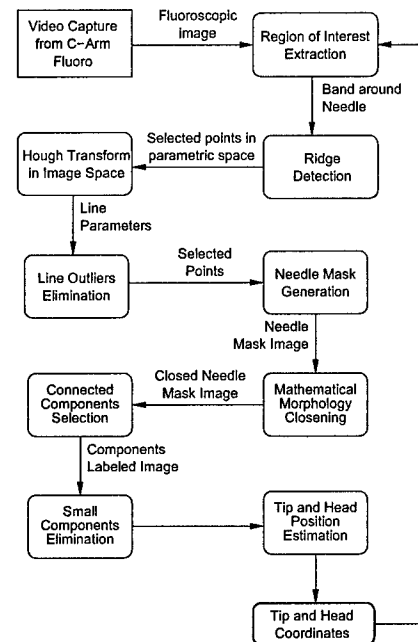
Let us consider the needle rotation in a plane around its tip, as illustrated in Figure 12. If the image plane is parallel to the rotation plane, then the trajectory of the needle head is a circle in the image plane (plane A in Figure 12). If the planes are not parallel, then the needle head creates an ellipse in the image (plane B in Figure 12).
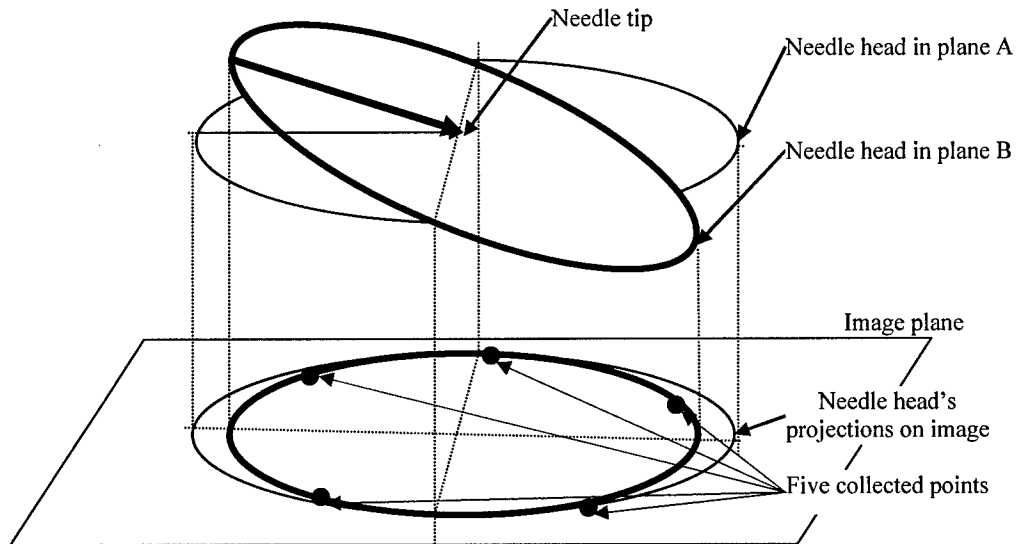
Figure 12. Needle rotation in two planes

During the alignment procedure, we have access only to the data that the image plane provides. Consequently, estimation of this ellipse is a critical to the needle alignment procedure presented here. In order to obtain the ellipse's points, the coefficients A, B, C, D, E, and F from the following general second degree quadratic equation should be estimated.

$$A*x^2 + B*x*y + C*y^2 + D*x + E*y + F = 0$$

To estimate these coefficients, five points on the ellipse are needed. These points are obtained with some human assistance, meaning the physician has to click on the needle head in the image five times. The orientation stage of the robot is used to move the needle head to five different positions in a plane. After each move, the physician must identify the needle head by selecting it in the image with the computer mouse. In the future, an automatic procedure for tracking the needle head would be desirable. The success of the parameter's estimation is strongly based on the distribution of the five points that are used for fitting the ellipse. These points should be evenly distributed. If they are too close, the fitting algorithm may not estimate the parameters precisely enough.

This procedure produces the coefficients of the second degree quadratic equation. With these coefficients, all the other points of the ellipse can be easily computed. Each estimated point serves as an input for the next phase of the procedure. For each of the estimated points, the following steps are taken:

1) Having the point on the ellipse in the image plane, the position of the needle's head in space may be estimated;

2) Having the position of the needle's head in space, the circle described by the head when rotating in the second plane of the RCM may be estimated.

3) The projection of the circle obtained in Step 2 is also an ellipse that may be estimated. If this ellipse represents a particular case representing a line, it means that the ellipse's point from the Step 1 is the one we are looking for.

The alignment method described above also takes into account the fact that the orientation stage of the robot can rotate the needle in two planes that have between them 99.3 degrees (fixed by design of the orientation stage). The alignment method consists of two steps as illustrated in Figure 13.

1) Rotate the needle in one plane (R0 plane) into a position that makes the second plane (R1 plane) perpendicular to the image plane. If the needle is moved in the second plane after this step, the needle head's trajectory is a line that represents the projection of the needle on the image plane.

2) Move the needle in the second plane so that it becomes a point in the image plane. After this step, the needle is aligned along the line of sight that passes through the target.
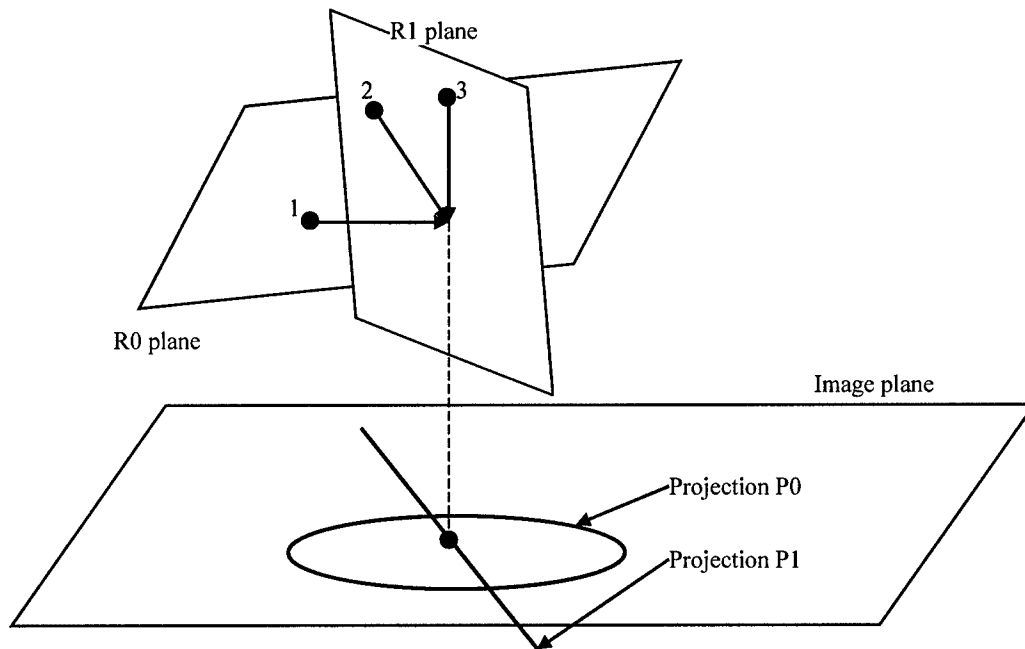


Figure 13. Alignment process

In Figure 13, three positions of the needle are shown. The needle head is first rotated in the R0 plane from position 1 to position 2. In the image plane, the projection P0 of the needle head that corresponds to a rotation in R0 plane is shown. If the plane R0 is parallel to the image plane, then the projection P0 would be a circle. Generally speaking, these planes are not parallel, and consequently the projection P0 is an ellipse. The best initial robot configuration makes the R0 plane as parallel as possible to the image plane so that the ellipse fitting is more numerically stable. If the R0 plane is nearly perpendicular to the image plane, then the projection P0 will become a degenerated ellipse and close to a line segment. This configuration would only work if the R0 plane is almost perfectly perpendicular to the image plane, so that needle alignment could be accomplished by rotation in the R0 plane only. However, we prefer to avoid this situation because it may lead to inconsistent results in the alignment process.

The purpose of rotating the needle in the R0 plane from position 1 to position 2 is to make the R1 plane perpendicular to the image plane. If this positioning is accomplished, then the projection P1 of the needle head that corresponds to a rotation in the R1 plane will be a line segment. A rotation in plane R1 from position 2 to position 3 will then make the needle perpendicular to the image plane so that it becomes a point in the image. The needle will then be aligned with the target and the procedure is complete.

The algorithm has been implemented in a C++ class called EllipseEstimator. This work was initially done as part of a project to develop an image-guided surgery software toolkit. The code was archived in a CVS repository and automatically built nightly on multiple platforms. This environment ensures that the code can be checked out, compiled, and built at any time. A testing infrastructure was also created for this class. Almost each public method has a testing procedure that makes sure the code performs as intended. Tests also run every night to help ensure the robustness and quality of the code.

The whole procedure may be described by the following sequence:
1) The patient is positioned on the procedure table.
2) The robot is positioned on the table over the patient so that the tip of the needle is in the vicinity of the skin entry point.
3) An anterior/posterior fluoroscopic image is obtained such that the target can be clearly seen and the whole needle is in the image.
4) The translational alignment procedure described in Section 2.1 is performed. The procedure segments and tracks the needle and moves the needle to the precise skin entry point.
5) The orientational alignment procedure described in Section 2.2 is performed.
6) Once the needle is aligned, a lateral fluoroscopic image is used to control the depth of insertion.

## 3. RESULTS

The translation procedure was run in the lab and in the clinical environment with good results.[9] The alignment procedure was tested in the laboratory environment using a standard video camera and a frame grabber. The orientation stage was moved to five different positions, and after each move the position of the needle tip in the image was obtained by selecting it with the mouse. These five points represent the input data for the EllipseEstimator class. As output, the class produces the coefficients A, B, C, D, E, F from the general 2nd degree equation. With these parameters, we computed the coordinates of points that belong to the ellipse at the pixel level and plotted all these points on the screen.

A sample result is shown in Figure 14. In this figure, the R0 plane of the RCM is almost parallel to the image plane, so the projection on the image plane is almost a circle.

A second example is shown in Figure 15. In this figure, more of an ellipse can be seen, as the R0 plane of the RCM is not as parallel to the image plane.

Both tests followed the standard protocol. The alignment process started with the tip of the needle coinciding with the target marked by physician. The needle was automatically positioned in five different spots using the R0 stage of the RCM, and needle head positions were taken. The ellipse parameters and the points that belong to the ellipse were estimated and plotted on the screen with red dots, as can be seen in Figures 14 and 15.
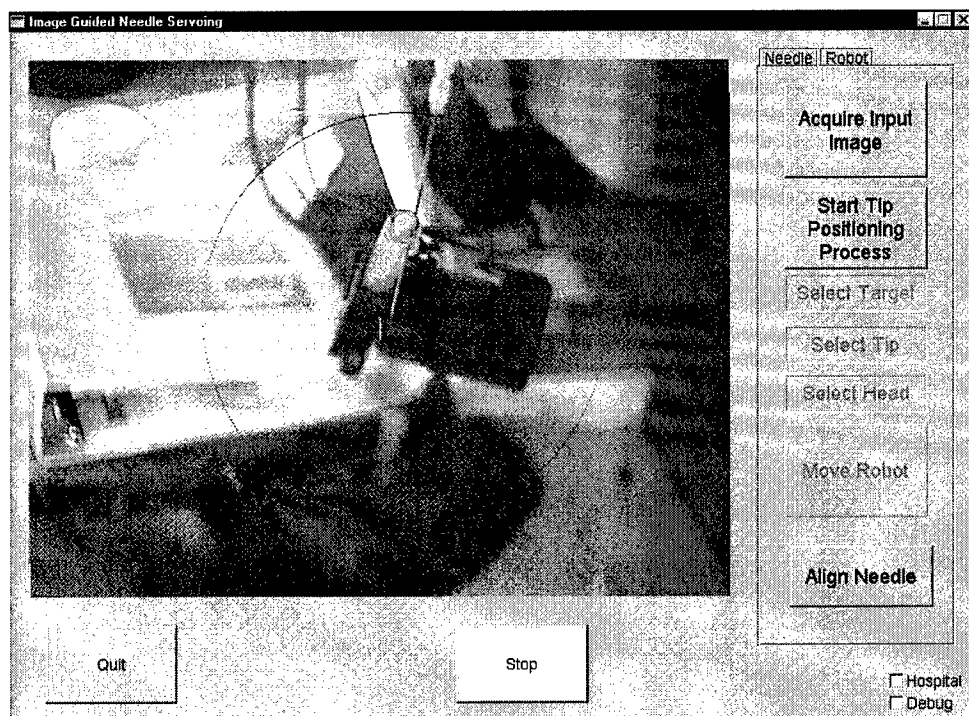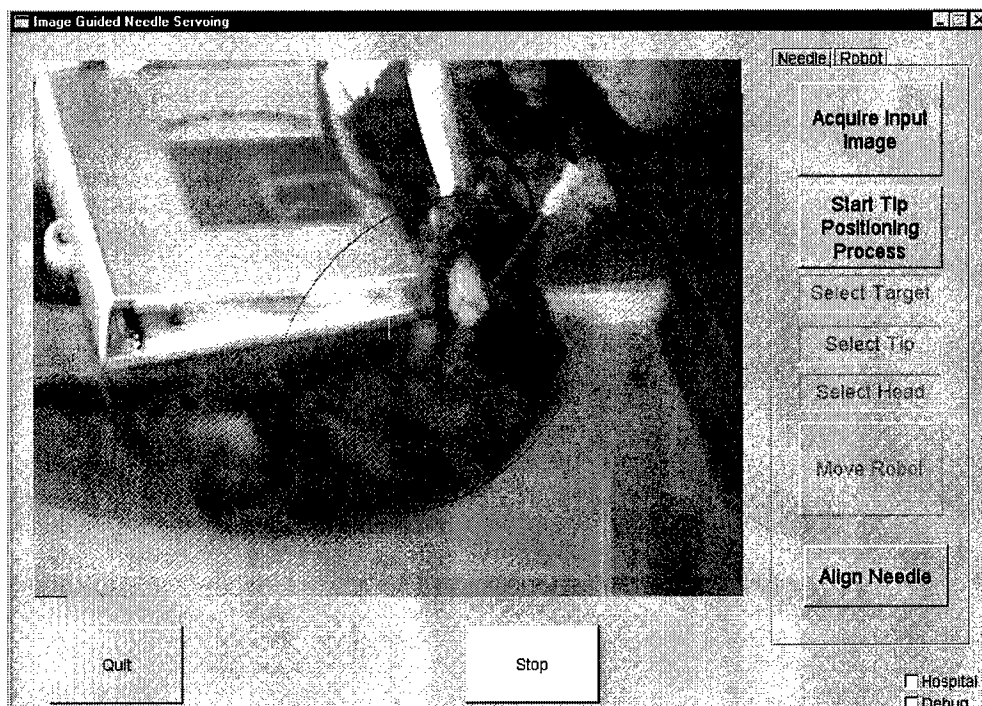
Figure 14. Sample Result #1



Figure 15. Sample Result #2

A human observer evaluated the results and determined that the needle head accurately followed the plotted points when rotated using R0 stage of RCM. We also noted that the needle tip remained stationary at the center of the estimated ellipse. Therefore, we believe this method can accurately position the needle.

## 4. CONCLUSIONS

A targeting method for fluoroscopy servoing based on a new alignment procedure has been presented. The alignment method requires only a single C-arm view and only five input points. Initial laboratory tests showed good qualitative results. The next step would be to do phantom testing in the interventional suite and verify that the method could be used for accurate needle placement under fluoroscopy.

The new method is fast and has several other advantages. There is no need for pre-operative registration, bi-planar X-ray images, or calibration of the system prior to use. Currently, the method is semi-automatic, since the physician selects the needle head in the images. This problem can be solved by placing a marker that will be segmented to locate the needle tip. The fact that the method uses the principles of projective geometry makes it simple and accurate, requiring little human interaction.

## ACKNOWLEDGMENTS

## REFERENCES

1. Cleary K., Watson V., Lindisch D., Patriciu A., Mazilu D., Stoianovici D. "Robotically Assisted Interventions: Clinical Trial for Spinal Blocks." *Medical Image Computing and Computer-Assisted Intervention - MICCAI 2003*, Springer, 963-964.
2. Loser M. H., Navab N., Bascle B., Taylor R.H. (2000). "Visual servoing for automatic and uncalibrated percutaneous procedures." *Proceedings of the SPIE - The International Society for Optical Engineering 3976*, (2000), San Diego, CA, USA, 271-280.
3. Patriciu A., Stoianovici D., Whitcomb L.L., Jarrett T., Mazilu D., Stanimir A., Iordachita I., Anderson J., Taylow R.H., Kavoussi L.R. "Motion-Based Robotic Instrument Targeting Under C-Arm Fluoroscopy." *MICCAI 2000*, Springer-Verlag, 988-998.
4. Mocanu M., Patriciu A., Stoianovici D., Mazilu D., Lindisch D., Corral G., Gruionu L., Cleary K. "Fluoroscopy servoing using translation/rotation decoupling in an A/P view." *Medical Imaging 2003: Visualization, Image-Guided Procedures, and Display*; Robert L. Galloway, Jr.; Eds. Proc. SPIE Vol. 5029, 161-165.
5. Stoianovici D., Whitcomb L.L., Anderson J.,Taylor R., Kavoussi L. "A Modular Surgical Robotic System For Image Guided Percutaneous Procedures." *MICCAI 1998*, Springer, 404-410.
6. Stoianovici D, Cleary K, Patriciu A, Mazilu D, Stanimir A, Craciunoiu N, Watson V, Kavoussi L. "AcuBot: A Robot for Radiological Interventions." *IEEE Transactions on Robotics and Automation*, Vol. 19, No. 5, (Oct. 2003), 927-930,
7. Eberly, D., "Ridges in Image and Data Analysis." *Kluwer Academic Publishers*, Dordrecht, 1996.
8. Aylward, S., Bullitt, E. "Initialization, noise, singularities, and scale in height ridge traversal for tubular object centerline extraction." *IEEE Transactions on Medical Imaging*, Vol. 21, 2002, 61–75.
9. Corral G, Ibanez L, Nguyen C, Stoianovici D, Navab N, Cleary K. "Robot control by fluoroscopic guidance for minimally invasive spine procedures." *Computer Aided Radiology and Surgery (CARS 2004)*, Elsevier, 509-514.

# Prediction of 3D internal organ position from skin surface motion: results from electromagnetic tracking studies

Kenneth H. Wong[*a], Jonathan Tang[a], Hui Zhang[a], Emmanuel Varghese[a,b], Kevin Cleary[a]

[a]Imaging Science and Information Systems (ISIS) Center, Department of Radiology, Georgetown University, 2115 Wisconsin Avenue NW #603, Washington, DC 20057;
[b]Department of Biomedical Engineering, The Catholic University of America, 620 Michigan Avenue NE, Washington DC 20064

## ABSTRACT

An effective treatment method for organs that move with respiration (such as the lungs, pancreas, and liver) is a major goal of radiation medicine. In order to treat such tumors, we need (1) real-time knowledge of the location of the tumor, and (2) the ability to adapt the radiation delivery system to follow this constantly changing location. In this study, we used electromagnetic tracking in a swine model to address the first challenge, and to determine if movement of a marker attached to the skin could accurately predict movement of an internal marker embedded in an organ. Under an approved animal research protocol, an electromagnetically tracked needle was inserted into a swine liver and an electromagnetically tracked guidewire was taped to the abdominal skin of the animal. The Aurora (Northern Digital Inc., Waterloo, Canada) electromagnetic tracking system was then used to monitor the position of both of these sensors every 40 msec. Position data from the sensors were then analyzed to see if any of the movements showed correlation. The strongest correlations were observed between external anterior-posterior motion and internal inferior-superior motion, with many other axes exhibiting only weak correlation. We also used these data to build a predictive model of internal motion by taking segments from the data and using them to derive a general functional relationship between the internal needle and the external guidewire. For the axis with the strongest correlation, this model enabled us to predict internal organ motion to within 1 mm.

**Keywords:** respiratory motion, radiotherapy, radiosurgery, image guidance, electromagnetic tracking

## 1. INTRODUCTION

An effective treatment method for organs that move with respiration (such as the lung, pancreas, and liver) is a major goal of radiation medicine. Tumors in these organs have typically been treated using a variety of methods to account for respiratory motion. The first and simplest of these methods is to irradiate the tumor plus a large surrounding area (margin) in order to ensure that the moving tumor remains within the region of prescribed dose at all times[1]. Although this method ensures sufficient dose to the tumor[2], it also tends to irradiate a large amount of healthy normal tissue, increasing the likelihood of complications or the creation of secondary cancers from radiation damage. Another possible approach is to control patient respiration, either with voluntary breath-holding[3,4] or through a mechanical device that regulates airflow into and out of the lungs[5]. In this case, the treatment beam is switched on once breathing has stopped and the tumor is stationary. This method can significantly reduce the margins around the tumor, but requires a high level of patient compliance and may not be practical for patients with compromised lung capacity. Furthermore, breath-holding tends to significantly extend the time required for patient treatment. A third approach is to actively monitor the respiration and turn the treatment beam on during a particular portion of the respiratory cycle[6,7,8]. This method requires less patient compliance than breath-holding and has similar advantages in terms of the ability to reduce tumor margins; however, it also requires a much longer treatment time since the beam is only on for a short fraction of the respiratory cycle. The fourth approach is to monitor the respiration and actively steer the radiation beam to follow the tumor as it moves[9,10]. Although this method is by far the most technically demanding, active steering can

---

[*] wong@isis.imac.georgetown.edu; phone 1 202 784-1521; fax 1 202 784-3479; www.isis.georgetown.edu

potentially achieve the tightly conformal margins of gating or breath-holding without significantly extending the treatment time, thus creating an optimal solution for respiratory motion compensation.

The active steering approach to respiratory motion compensation requires that we have (1) real-time knowledge of the location of the tumor, and (2) the ability to adapt the radiation delivery system to follow this constantly changing location. Although a variety of imaging modalities could potentially be used to follow the tumor location, most of them are not practical in the radiotherapy/radiosurgery environment. Ultrasound cannot effectively penetrate airspaces within the body (such as the lungs) and also requires a skilled operator, who obviously cannot be standing next to the patient during treatment. Magnetic resonance imaging (MRI) systems are generally too confined to allow much access to the patient, and the strong magnetic fields would likely disrupt the operation of the treatment machine. Computed tomography (CT) has similar geometric limitations to MRI, although they are not quite as prohibitive since the CT scanner tends to be slightly smaller. Onishi *et al.* reported on the use of CT in a radiation therapy environment[11], although this implementation was used to improve patient breath-holding as opposed to active tumor tracking. Fluoroscopy has a fairly small footprint and can generate images at video rates (roughly 30 Hz), and has been successfully used for respiratory-gated radiotherapy[8,12]. However, CT and fluoroscopy both place an additional radiation dose burden on the patient.

Since none of these imaging techniques are truly optimal, there has been much interest in defining some other means to track the tumor position in real-time. Much of the work in this area has focused on the use of optical tracking to measure the motion of skin on the abdomen or thorax, which can then potentially be used as a surrogate signal for internal tumor motion. Optical tracking is an excellent means of following respiration because it is non-invasive, has very high accuracy/precision, is relatively inexpensive, and can easily provide real-time results. However, since optical tracking methods depend on having a line-of-sight to the target, the true motion of the internal target must be obtained through some other means and then correlated to the skin motion. Some investigators have used fluoroscopy with fiducial markers implanted near the tumor and on the skin surface, so that a single fluoroscopy image measures both internal and external locations[9,13,14], whereas others have obtained similar data using MRI[15]. These studies showed that for some cases, a strong correlation existed between internal tumor motion and external skin motion. However, for other cases, the correlation was rather weak or was negatively affected by phase differences between the two motions. Furthermore, both fluoroscopy and MRI have important limitations. Fluoroscopy is inherently limited to two-dimensional projections and thus cannot measure three-dimensional motion (although three-dimensional motion can be obtained from multiple simultaneous projections). Although MRI is volumetric, the volume is typically acquired slice-by-slice, so there is always the potential for a shift in the anatomy between slices. Even with a respiratory-gated pulse sequence, one cannot be certain that the anatomy always returns to the same position during the next acquisition.

In this paper, we report on the use of electromagnetic tracking in an animal model to obtain data on the correlation between external motion and internal motion. Although electromagnetic tracking is not an imaging modality and is limited to following discrete points in a three-dimensional space, it has distinct advantages over other methods. First, it does not use ionizing radiation, and thus can be active for long periods of time without any adverse effects on the patient. Second, it tracks continuously and in three dimensions, so we are able to capture the complete temporal and spatial characteristics of the motion. Third, the system itself is physically compact, and thus is easily able to be integrated into a radiotherapy/radiosurgery environment. Finally, unlike optical tracking systems, it is not limited to line-of-sight operation. Because of these last two properties, electromagnetic tracking could conceivably be used to directly monitor internal tumor motion; we have an active research effort in this area.

## 2. METHODOLOGY

### 2.1. Electromagnetic tracking system

For this study, we used the Aurora (Northern Digital Inc., Waterloo, Ontario, Canada) electromagnetic tracking system. The system consists of three parts, as illustrated in Figure 1:

(1) a tetrahedon-shaped generator that creates a rapidly switching magnetic field,
(2) specially constructed needles, guidewires, catheters, or other tools containing tiny wire coils,
(3) a control unit and sensor interface units that measure currents induced in the coils by the changing field.
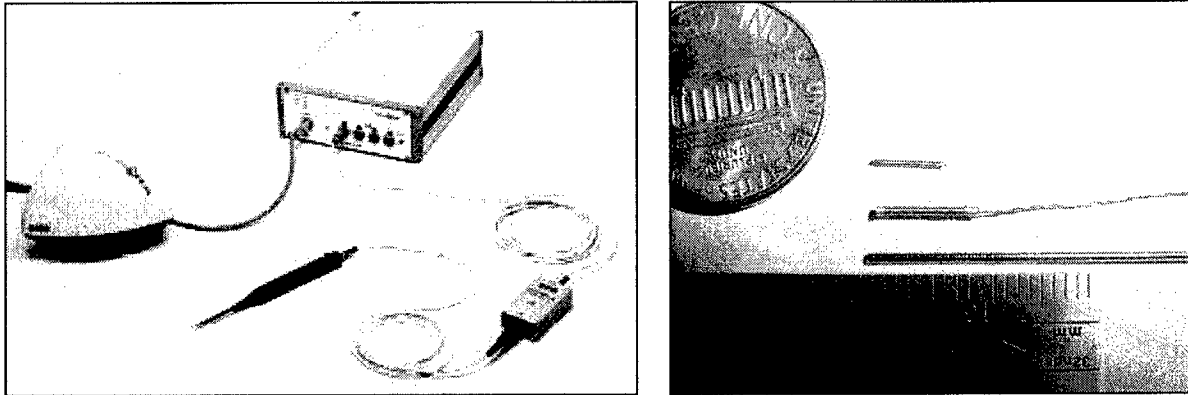
Figure 1: Left half of figure shows the Aurora System from Northern Digital Inc. (field generator on left, control unit in top middle, sensor interface unit on right side, and electromagnetically tracked probe in bottom middle). Right half of the figure shows sensor coils and tools developed and manufactured by Traxtal. Figures courtesy of Northern Digital and Traxtal.

The needles and guidewires for this study were designed and manufactured by Traxtal (Bellaire, TX, USA). Needles were 18 gauge (0.838 mm nominal outer diameter) and the guidewires were 0.89 mm diameter (approximately 3 French). Once the system is activated, it continuously reports both the position and orientation of the tools/probes that are plugged into the interface units. In-house software is used to poll the Aurora and read out position/orientation data. The overall readout frequency is between 10 and 25 Hz depending on the number of tools that are plugged into the control box.

## 2.2. Experimental procedures

All research in this study was carried out under an institutionally-approved animal protocol. Small (between 50 and 70 pounds) swine were anesthetized and positioned supine (ventral side up) on an interventional radiology table. The table is made from carbon fiber and thus is radiolucent and nonmagnetic while still providing excellent structural strength. The swine were positioned inside a custom-made wooden frame that kept their body orientation fixed and allowed them to be more easily positioned on the table. The table was positioned so that a region around the liver would be visible to the biplane fluoroscopy system in the room (Neurostar, Siemens Medical Solutions, Malvern, PA, USA), and the Aurora field generator was clamped to a positioning arm and positioned over the abdomen of the animal.

The first step of the study was to register the internal Aurora coordinate system to 'animal-centric' coordinates (left-right, superior-inferior, anterior-posterior). This registration was accomplished by placing a calibration frame on a separate positioning arm just above the animal's chest, as shown in Figure 2. The frame is a piece of plastic with several holes drilled into it. These holes have a known spacing and orientation. One axis of the frame is aligned with the animal's superior-inferior (head-tail) axis, and the frame is leveled so that the plane formed by the superior-inferior and left-right axes is parallel to the table surface. An electromagnetically tracked needle is then placed into each of the holes of the calibration frame and its position/orientation is recorded for 10 seconds. Once readings have been obtained from all of the holes in the frame, we have sufficient data to calculate an affine transformation between the two coordinate systems.
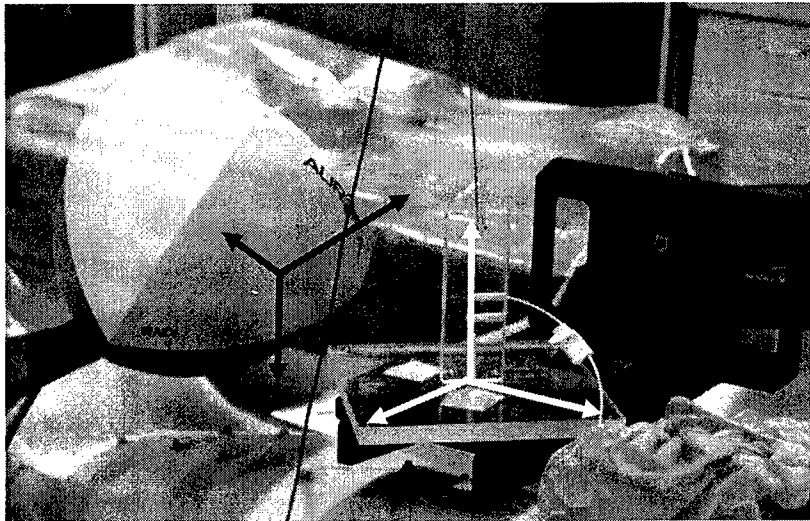
Figure 2: Aurora electromagnetic tracking system and calibration frame positioned over the animal. The frame has several holes drilled into it with known spacing. The electromagnetically tracked needle can be placed into the holes in order to register the Aurora coordinate system (illustrated by the black arrows) to an animal-centric coordinate system (illustrated by the white arrows).

Once the calibration step is complete, the electromagnetically tracked needle is percutaneously implanted in the liver. The needle position is confirmed using biplane fluoroscopy. One or more guidewires are then taped to the skin surface. The guidewire position was not specified by anatomical landmarks; rather, we tried to place it on regions of the skin that showed the most motion. Likewise, the specific location in the liver for the needle was not specified, but we always confirmed that it was in the liver tissue and not a large blood vessel. The setup for recording respiratory motion is shown in Figure 3.
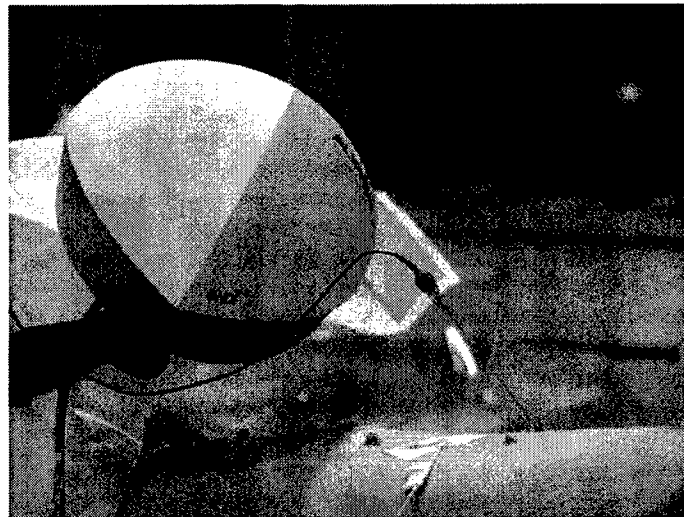


Figure 3: Aurora electromagnetic tracking system set up for respiratory tracking. The needle is inserted percutaneously into the liver, and the guidewire is taped to the skin.

We then recorded data from the needle and guidewire(s) for 10 to 20 minutes. During the study, the breathing rate varied slightly from animal to animal but was generally around 11 breaths per minute.

## 3. DATA ANALYSIS

Log files from the Aurora were processed using Excel or Matlab. Respiratory motion data were first transformed into animal-centric coordinates using the data from the calibration frame measurements. Because the Aurora reads each sensor sequentially rather than in parallel, we interpolated the data so that the internal needle and any other guidewires had the same timebase as the first external guidewire. This gave us a series of (x,y,z) coordinates for each time point. Plots of internal versus external coordinates were created and used to determine the level of correlation between different axes of motion (for example, external left-right motion and internal left-right motion).

We also examined the hypothesis that the position of the external guidewire could reliably predict the position of the internal needle using a linear model. First, we used the entire data set to obtain linear fits between internal and external axes of motion (for example: $m$ * external left-right + $b$ = internal left-right). Such an equation essentially represents a theoretically optimal predictor, because it is based on all of the data from a given animal. Using these equations, we attempted to predict internal motion based on external motion and evaluated the results. Next, we chose a small subset of the data by selecting either a short time segment (25 seconds) from the beginning of the recording or a short time segment from another random location within the recording. This approach reflects a more realistic predictor; in radiotherapy/radiosurgery situations, a model of respiratory motion might be calculated from an initial observation of the patient's breathing and then used to carry out the remainder of the treatment. Data from this subset was again parameterized using a linear fitting, and the fitting coefficients were applied to the external guidewire coordinates to generate predicted internal needle positions. These predicted positions were then compared to the actual recorded positions from the experiment by calculating the root-mean-square value of (*predicted - actual*), which is defined as

$$RMS = \frac{\sqrt{\sum |(predicted - actual)|^2}}{\sqrt{n}},$$

where $n$ is the number of compared values.

## 4. RESULTS

Figure 4 shows a nine-way correlation plot from one of the experimental animals. Each subplot represents the correlation between one external axis (the abscissa) and one internal axis (the ordinate), so this represents an overview of the correlation between external and internal motion. In this figure, the strongest correlation (r=0.938) is observed between external posterior-anterior motion and internal inferior-superior motion (bottom row middle). By contrast, the weakest correlation (r=0.485) is between external left-right and internal posterior-anterior motion (top row right). In general, the external posterior-anterior motion is the largest component of external motion and seems to have the most significant effect on internal position, whereas the effects of external left-right motion and external inferior-superior motion are relatively small.

These results agree well with previously published data from fluoroscopy studies[9,13] and with our own anecdotal experience with respiratory motion. Diaphragmatic movement in the inferior direction is usually accompanied by an expansion of the abdominal region, so these results are also physiologically sensible.

Using the data shown in Figure 4, we calculated linear fits for each of the subplots. For example, the bottom row middle subplot yields:

internal inferior-superior = (-0.4993)(external posterior-anterior)-28.95     fit based on all data
internal inferior-superior = (-0.5218)(external posterior-anterior)-30.56     fit based on first 25 seconds
internal inferior-superior = (-0.5066)(external posterior-anterior)-29.45     fit based on random 25 second segment

Figures 5 and 6 show plots of the actual internal inferior-superior motion vs. the predicted internal inferior-superior motion. Since the correlation from the bottom row middle subplot was high, the prediction ability in these cases is very good, and prediction based on a short segment of the data is nearly as good as prediction based on the entire data set. Active steering of a radiation beam based on these data should be quite successful.

By contrast, if we repeat this fitting on the top row right subplot, we obtain:

internal posterior-anterior = (-0.7440)(external left-right)-50.96        fit based on all data
internal posterior-anterior = (-0.5198)(external left-right)-61.96        fit based on first 25 seconds
internal posterior-anterior = (-0.8045)(external left-right)-47.93        fit based on random 25 second segment

Figure 7 shows the actual internal posterior-anterior motion versus predicted internal posterior-anterior motion. In this case, the correlation from the top row right subplot was poor, so it is not surprising that the prediction ability is also poor. However, because the magnitude of internal posterior-anterior motion is much less than the magnitude of internal inferior-superior motion, the RMS error of (predicted-actual) is still relatively small. This result has an interesting and practical implication for respiratory motion compensation using active steering: if the motion along a particular axis is small, our inability to exactly predict that motion may not have a significant effect on the final radiation dose distribution.
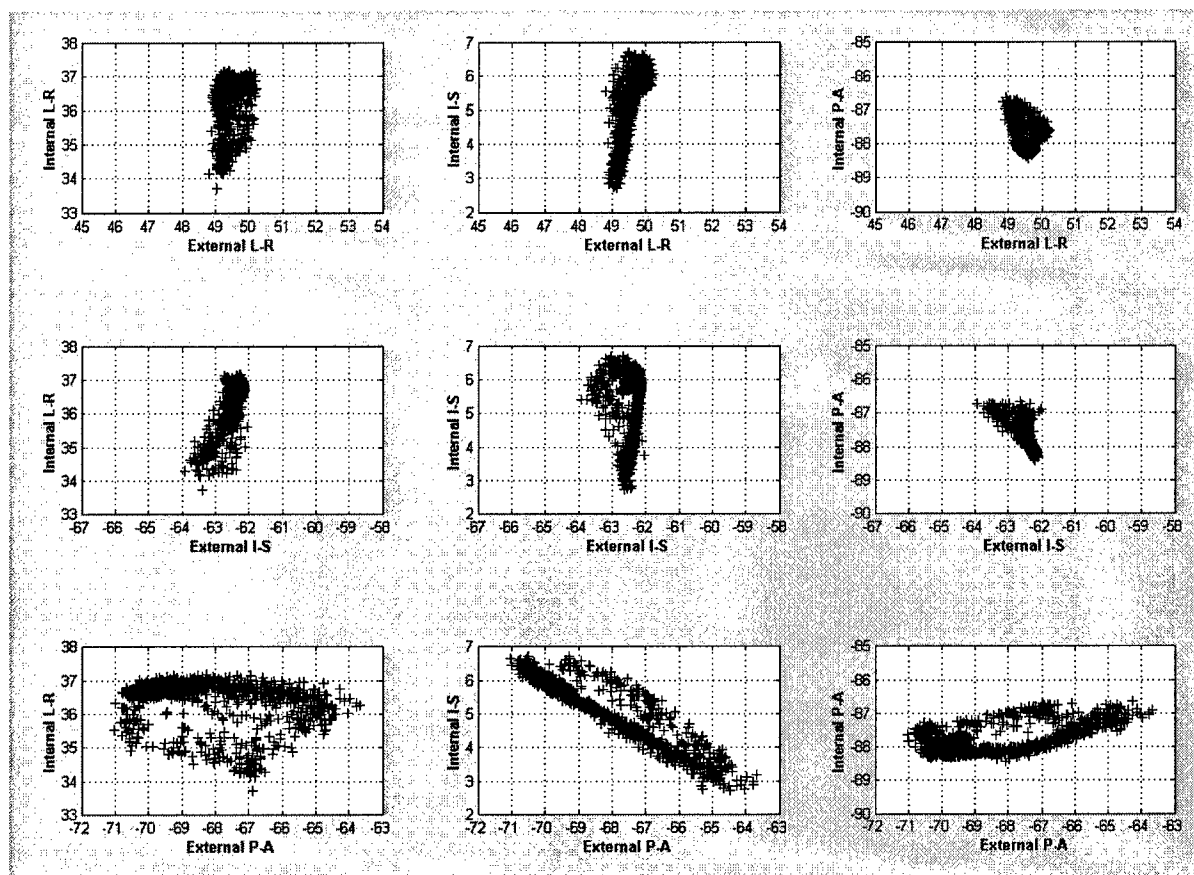


Figure 4: Plot showing the overall relationship between external motion and internal motion. Each subplot displays the correlation between one external axis and one internal axis. The scale for all axes is in mm.
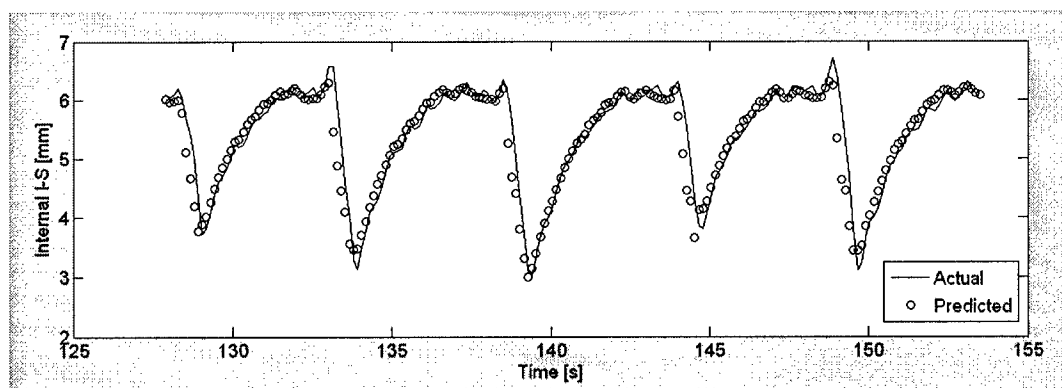
Figure 5: Plot illustrating prediction of internal I-S motion based on all data. Solid line represents the actual recorded internal motion, open circles represent the predicted internal motion based on external skin data The RMS error of (predicted - actual) is 0.3053 mm.
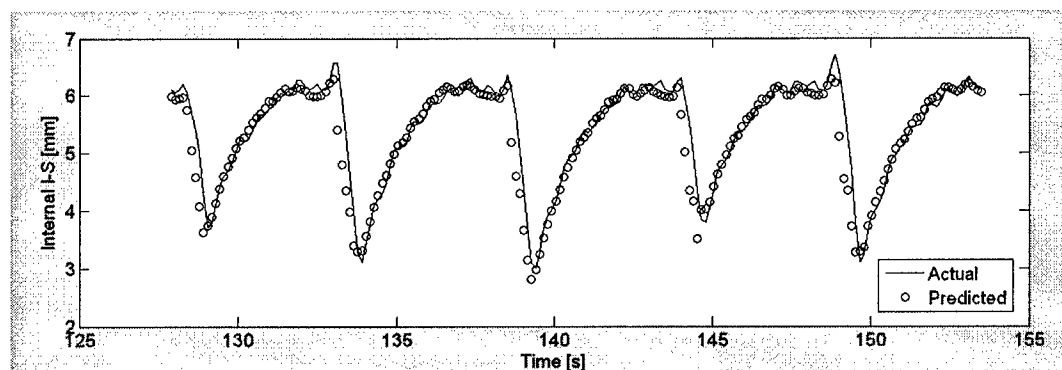


Figure 6: Plot illustrating prediction of internal I-S motion based on the first 25 seconds of the data. Solid line represents the actual recorded internal motion, open circles represent the predicted internal motion based on external skin data. The RMS error of (predicted - actual) is 0.3280 mm.
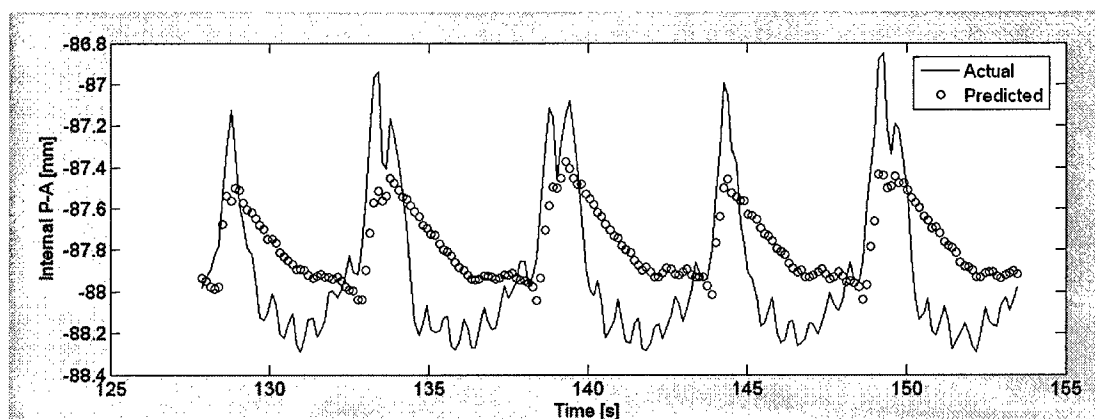


Figure 7: Plot illustrating prediction of internal P-A motion based on all correlation data. Solid line represents the actual recorded internal motion, open circles represent the predicted internal motion based on external skin data. The prediction here is clearly not as good as the previous two figures. However, since the overall P-A motion is much smaller than the overall I-S motion, the RMS error of (predicted - actual) is still quite small at 0.3038 mm.

## 5. CONCLUSIONS

To our knowledge, this is the first study that has used electromagnetic tracking to simultaneously monitor internal and external motion, and the first study that has examined the predictive ability of skin motion based on such data. Electromagnetic tracking offers key advantages in this type of study. First, it has the capability to monitor both internal and external motion, unlike optical tracking. Second, by using the electromagnetic tracking system for both motions, we eliminate sources of error that stem from needing to synchronize or register multiple separate tracking or imaging systems. Only a coordinate transformation is necessary to map the Aurora coordinates into a more natural coordinate system for analyzing breathing motion. Third, electromagnetic tracking uses no ionizing radiation, and therefore can be operated over a large number of breathing cycles. Finally, electromagnetic tracking is not adversely affected by intervening layers of tissue and does not require a clear line-of-sight to operate. This last property could eventually provide a means to move beyond predictive models of internal motion to tracking internal targets directly, which would further improve the accuracy of respiratory motion compensation through active beam steering.

Based on the results of this study, we conclude that it is possible to accurately model a portion of internal organ motion by tracking the position of markers on the external skin, at least in the experimental animals studied here. The accuracy of this prediction, computed as the RMS of (predicted - actual) is less than 1 mm. Although this study looked at the motions by comparing single axes against each other, we are currently developing a fully three-dimensional method for studying the correlation and predictability in a more comprehensive way.

It is, of course, important to recognize some inherent limitations to this study. First and foremost is that the animals in this study were under general anesthesia and were mechanically ventilated. Thus, their breathing patterns were quite regular and not the same as if they were breathing naturally. In some ways, this test therefore represents a 'best-case' scenario because some of the irregularity and complexity of normal breathing was removed by the ventilator. Second, given that the study required inserting needles into the liver, it may be difficult to transition this technique into human patients, especially normal healthy volunteers. However, continuous advancement in the miniaturization of electromagnetically trackable tools and probes leads us to believe that we will eventually be able to move this technology into a clinical trial in a radiotherapy or radiosurgery environment.

## 6. ACKNOWLEDGEMENTS

## 7. REFERENCES

1.  L. Ekberg, O. Holmberg, L. Wittgren, G. Bjelkengren, and T. Landberg, "What margins should be added to the clinical target volume in radiotherapy treatment planning for lung cancer?" Radiother Oncol 48 (1), 71-77, 1998.
2.  J. Mechalakos, E. Yorke, G. S. Mageras, A. Hertanto, A. Jackson, C. Obcemea, K. Rosenzweig, and C. Clifton Ling, "Dosimetric effect of respiratory motion in external beam radiotherapy of the lung", Radiother Oncol 71 (2), 191-200, 2004.
3.  D. J. Kim, B. R. Murray, R. Halperin, and W. H. Roa, "Held-breath self-gating technique for radiotherapy of non-small-cell lung cancer: a feasibility study", Int J Radiat Oncol Biol Phys 49 (1), 43-49, 2001.
4.  M. J. Murphy, D. Martin, R. Whyte, J. Hai, C. Ozhasoglu, and Q. T. Le, "The effectiveness of breath-holding to stabilize lung and pancreas tumors during radiosurgery", Int J Radiat Oncol Biol Phys 53 (2), 475-482, 2002.
5.  J. W. Wong, M. B. Sharpe, D. A. Jaffray, V. R. Kini, J. M. Robertson, J. S. Stromberg, and A. A. Martinez, "The use of active breathing control (ABC) to reduce margin for breathing motion", Int J Radiat Oncol Biol Phys 44 (4), 911-919, 1999.

6.      K. Ohara, T. Okumura, M. Akisada, T. Inada, T. Mori, H. Yokota, and M. J. Calaguas, "Irradiation synchronized with respiration gate", Int J Radiat Oncol Biol Phys 17 (4), 853-857, 1989.

7.      H. D. Kubo and B. C. Hill, "Respiration gated radiotherapy treatment: a technical study", Phys Med Biol 41 (1), 83-91, 1996.

8.      H. Shirato, S. Shimizu, T. Kunieda, K. Kitamura, M. van Herk, K. Kagei, T. Nishioka, S. Hashimoto, K. Fujita, H. Aoyama, K. Tsuchiya, K. Kudo, and K. Miyasaka, "Physical aspects of a real-time tumor-tracking system for gated radiotherapy", Int J Radiat Oncol Biol Phys 48 (4), 1187-1195, 2000.

9.      A. Schweikard, G. Glosser, M. Bodduluri, M. J. Murphy, and J. R. Adler, "Robotic motion compensation for respiratory movement during radiosurgery", Comput Aided Surg 5 (4), 263-277, 2000.

10.     A. Schweikard, H. Shiomi, and J. Adler, "Respiration tracking in radiosurgery", Med Phys 31 (10), 2738-2741, 2004.

11.     H. Onishi, K. Kuriyama, T. Komiyama, S. Tanaka, N. Sano, Y. Aikawa, Y. Tateda, T. Araki, S. Ikenaga, and M. Uematsu, "A new irradiation system for lung cancer combining linear accelerator, computed tomography, patient self-breath-holding, and patient-directed beam-control without respiratory monitoring devices", Int J Radiat Oncol Biol Phys 56 (1), 14-20, 2003.

12.     H. Shirato, S. Shimizu, K. Kitamura, T. Nishioka, K. Kagei, S. Hashimoto, H. Aoyama, T. Kunieda, N. Shinohara, H. Dosaka-Akita, and K. Miyasaka, "Four-dimensional treatment planning and fluoroscopic real-time tumor tracking radiotherapy for moving tumor", Int J Radiat Oncol Biol Phys 48 (2), 435-442, 2000.

13.     C. Ozhasoglu and M. J. Murphy, "Issues in respiratory motion compensation during external-beam radiotherapy", Int J Radiat Oncol Biol Phys 52 (5), 1389-1399, 2002.

14.     J. D. Hoisak, K. E. Sixel, R. Tirona, P. C. Cheung, and J. P. Pignol, "Correlation of lung tumor motion with external surrogate indicators of respiration", Int J Radiat Oncol Biol Phys 60 (4), 1298-1306, 2004.

15.     N. Koch, H. H. Liu, G. Starkschall, M. Jacobson, K. Forster, Z. Liao, R. Komaki, and C. W. Stevens, "Evaluation of internal lung motion for respiratory-gated radiotherapy using MRI: Part I--correlating internal lung motion with skin fiducial motion", Int J Radiat Oncol Biol Phys 60 (5), 1459-1472, 2004.

# Respiratory Motion Compensation Studies Using a 3D Robotic Motion Simulator and Optical/Electromagnetic Tracking Technologies

Kenneth H. Wong, Jonathan Tang, Sonja Dieterich, Hui Zhang, Tong Zhou, and Kevin Cleary

*Abstract*-- Respiratory motion can degrade the quality of nuclear medicine images, especially when attempting to identify small abnormalities, make quantitative estimates of activity concentration, or track the time-varying location of a tumor. Thus, we are developing methods for respiratory motion compensation and testing these methods using robotic devices. The testing device is a computer controlled 3-axis motion simulator that can hold activity-filled phantoms or spheres and move them along pre-programmed paths to simulate respiratory motion. The motion of the platform is programmed in advance and can also be monitored using an optical tracking system, thus providing a solid ground truth for the time-dependent activity concentration. Registration between the coordinate space of the PET or SPET scanner and the optical tracker coordinate system is based on a set of common points (mapped out using the motion simulator) that are visible to both systems. We have also used electromagnetic tracking and optical tracking to obtain realistic respiratory motion data from patients and animal models. These data can be transformed into motion simulator paths, thus providing us with breathing patterns that accurately reflect the nonstationary and variable nature of human respiration. The simulator thus provides a highly useful tool for repeatably testing different approaches to motion-compensated image reconstruction or gated acquisition schemes.

## I. INTRODUCTION

FUNCTIONAL imaging studies such PET and SPET have many uses in diagnosing and staging human disease. However, respiration can be a severely complicating factor in these studies, as many organs move and deform during normal breathing. Given that most PET and SPET studies require the patient to be imaged for approximately 30 to 60 minutes, the organs of interest cannot be considered to be stationary or even to be moving in a perfectly periodic fashion. Furthermore, the magnitude of respiratory-induced motion is typically larger than the resolution of the detector. The combination of these factors can alter the apparent volume and activity concentration of an abnormality and may even render small objects invisible against the noisy background found in many nuclear medicine studies.

Since patients obviously cannot hold their breath for the entire length of the study, it is imperative to develop methods for respiratory motion compensation. Although a simple respiratory gating approach (analogous to ECG gating in cardiac nuclear medicine) could be attempted, this would likely increase the noise in the image since the detector counts would have to be split into several bins through the respiratory cycle. A better approach would be to synchronously record the time-varying respiratory motion of the patient with the events in the detector, and to use all of the resulting data for the reconstruction.

Our research group has therefore developed a 3D robotic motion simulator system that can be used in the development and verification of reconstruction algorithms that include motion compensation. Whereas patients typically have highly variable breathing patterns that cannot be predicted, the simulator hardware can be programmed in advance, thus providing a known time-varying activity distribution. Respiratory motion paths in the simulator can be purely periodic to provide simple test cases, or can reflect a more realistic variable breathing pattern. This device thus fulfills two important purposes. First, it gives us a platform for testing the acquisition methods for respiratory compensated PET/SPET (e.g. what type of tracking system should be used, and what spatial/temporal accuracy is necessary). Second, it provides a 'ground truth' for experimental testing of reconstruction methods that use motion compensation; since we know the activity concentration as a function of time, we can more readily make rigorous, quantitative assessments of the reconstruction.

## II. ENGINEERING DESIGN OF THE SIMULATOR

The motion simulator is a 3-axis motion platform using orthogonal linear slides (Velmex, Bloomfield, NY) linked to lead screws and motors (Maxon, Burlingame, CA), as shown in Figure 1. Arms constructed of aluminum, Delrin, and

plexiglass can be attached to one of the slides, which allows a test pattern or phantom to be moved within the field of view of a PET or SPET gantry. The robot is controlled by a PC through an Ethernet-addressable motion controller board (Galil, Rocklin, CA) which drives the motors and monitors their position using feedback from rotary encoders. Accuracy tests of a previous version of the simulator showed that individual axis error was ±0.03 to ±0.08 mm, with an overall system accuracy of ± 0.1 mm [1]. The maximum speed of the slides is several cm/second, which is far in excess of the speeds of typical respiratory motion. Move commands are processed every 64 or 128 msec, so the motion appears continuous. The range of motion of the slides varies depending on the particular axis configuration, but is at least 6 cm, which allows for the full range of respiratory motion as reported in the literature [2-3].

The simulator can be given a periodic (sinusoidal) motion path in one, two, or three axes using a combination of Matlab and C++ programs written with the Galil WSDK (Windows Software Developers Kit). Amplitude, frequency, and phase can be set to any value within the range of motion of the slides and the motor's maximum speed. We have also developed display tools for playing back motion commands so that they can be easily visualized. A complex periodic 3D motion path built from three orthogonal sinusoidal paths is shown in Figure 2.

The simulator axes can be registered to the coordinate space of an imaging scanner (such as a PET or SPET system) by attaching a radioactive marker (as illustrated in Figure 3) to the arm and running a calibration program that moves each axis independently, thus mapping out 3 known lines in the coordinate system of the simulator. The resultant emission image can then be analyzed to determine the orientation of these lines in imaging space, which allows us to derive a transformation between the scanner coordinate system and the respiratory motion simulator coordinate system. We have previously used the simulator in this way to imitate breathing motion artifacts in SPET [4].

## III. ACQUISITION OF REALISTIC RESPIRATORY MOTION DATA

An important characteristic of respiratory motion is that it is highly variable and can change over long and short timescales. Furthermore, accurate prediction of breathing patterns from *a priori* anatomical data such as a static CT or MRI scan is extremely challenging. Thus, we have devoted much of our recent efforts into building up a database of recorded respiratory motion and robot command files -- our interface software can be given a contour of arbitrary 3D points in time and will reproduce that path as closely as possible. These data provide for realistic yet repeatable studies over a wide range of respiratory conditions, and will hopefully serve as the starting point for a larger public repository of dynamic or "4D" images. We are currently

making use of both electromagnetic and optical tracking to gather these data. All studies were performed under approved human or animal research protocols.

### A. Electromagnetic Tracking

Figure 4 shows the Aurora (Northern Digital, Waterloo, ON) electromagnetic tracking system set up for recording respiratory motion in a swine animal model. Electromagnetic tracking provides a method for continuous tracking of needles, guidewires, and other implantable markers/probes. A field generator (the white tetrahedron-shaped object) creates an oscillating magnetic field, which induces current in pickup coils in the probes. These currents are then used to compute a position and orientation for the probe. Magnetic tracking has the key advantage of being able to track through solid objects (which allows monitoring of internal organs) and is capable of recording at > 10 Hz over long periods of time, thus enabling us to observe high-frequency periodicity and low-frequency shifts in breathing patterns, such as anatomical settling or drift.

### B. Optical Tracking

We have recorded skin surface motion from patients using both passive (Polaris, Northern Digital, Waterloo, ON) and active (Flashpoint, Image Guided Technologies, Boulder, CO; Optotrak, Northern Digital, Waterloo, ON) optical tracking systems. These studies were first reported in [5] and are continuing as an integral part of Cyberknife radiosurgery treatments at our institution. Optical tracking is completely non-invasive, has sub-millimeter position accuracy, can track continuously over long periods of time, and can operate over 3-4 meters range as long as line-of-sight is preserved. Typical sampling rates with optical tracking are > 20 Hz, which is more than sufficient for measuring respiratory motion. Active markers can be tracked more reliably than passive markers, but are more expensive and are not currently available in wireless form. Figure 5 shows a sample Polaris recording from a patient, demonstrating a somewhat steady-state breathing pattern with intermittent deviations. We are currently seeking institutional approval to begin using this tracking system on patients scheduled for PET and SPET scans.

## IV. CONCLUSIONS

The respiratory motion simulator provides a means for quantitatively examining the effects of patient movement during radionuclide imaging. A key advantage of the system is its flexibility; it can be programmed to generate motion paths of any size and shape. This flexibility allows us to easily simulate different types of motion (breathing, cardiac, patient fidgeting, etc...) so that we can study their effects. Furthermore, while the system has great flexibility, its motion is also highly repeatable due to the precision of the motors and sliders. We are gathering data on realistic respiratory

motion patterns and creating an excellent test bed for evaluating respiratory motion compensation methods and reconstruction algorithms.

The simulator is therefore a unique and valuable tool for the development and testing of methods to compensate for motion-induced blurring in PET and SPET. We are currently implementing optical tracking of skin motion in our SPET and PET scanners, and will use this tracking with the motion simulator to help develop reconstruction algorithms that compensate for respiratory motion. We are also investigating "4D" PET and SPET imaging for determining the time-dependent position of a "hotspot" on functional imaging. Such information will be vital in the development of interventional radiology and radiosurgery therapies that include motion compensation, as motion data will enable a new level of precision for image-guided therapy.



Fig. 2. Sample complex path for the 3D respiratory motion simulator. Axis units are in mm, with the longest axis (range of -10 to 10) representing the inferior-superior axis on the patient. By adjusting phase, frequency, and amplitude, both simple and complex periodic motion paths can be obtained.



Fig. 3. Motion simulator arm shown with radioactivity-filled spheres attached for calibration, which allows the simulator coordinate space to be matched to the imaging system coordinate space.
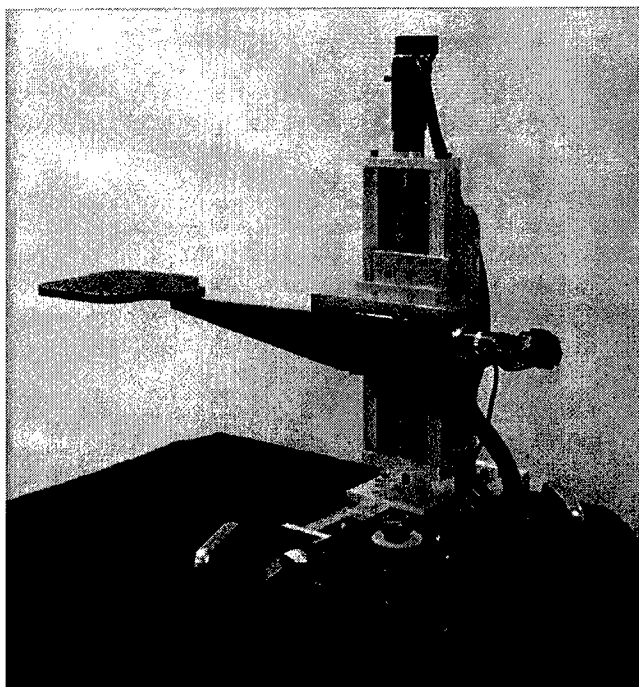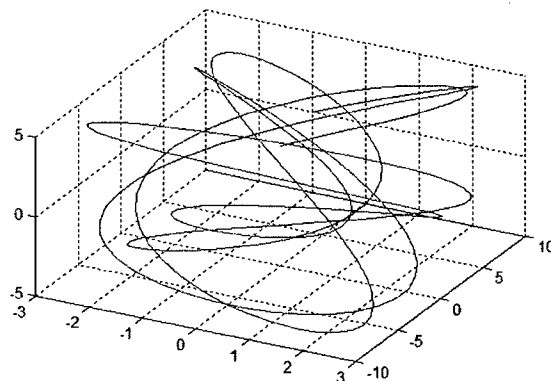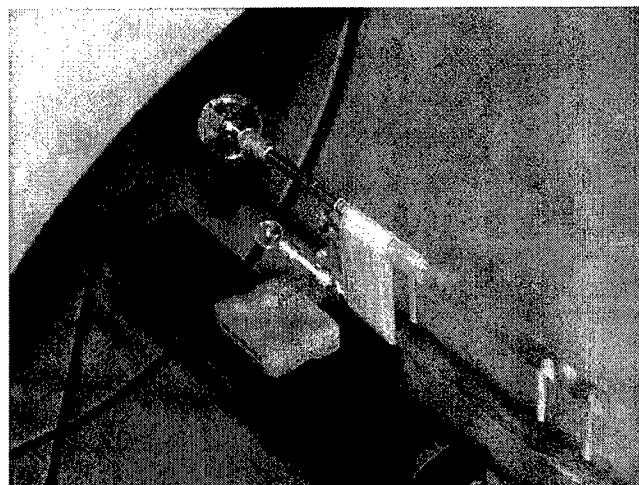


Fig. 1. Picture of the 3D robotic motion simulator. The straight extension arm extends out from the linear stages to allow a test pattern or phantom to be placed inside the active area of the scanner.
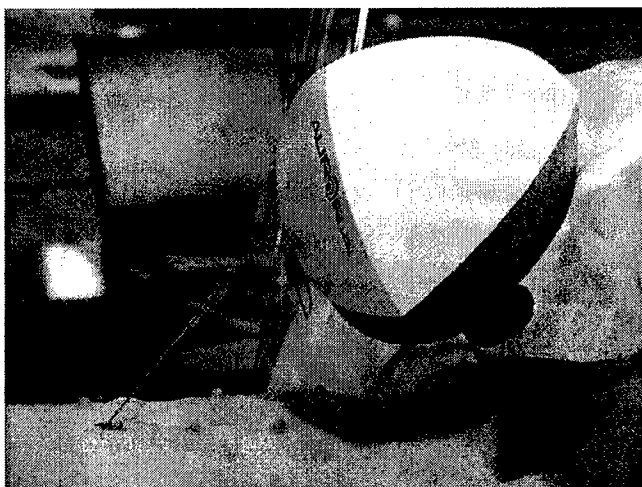
Fig. 4. Setup for electromagnetic tracking experiments in swine model. The white tetrahedron is the magnetic field generator. Induced currents are measured from a coil at the end of the needle (which has been implanted into the liver) and a guidewire (taped to the skin surface just to the right of the needle insertion point).
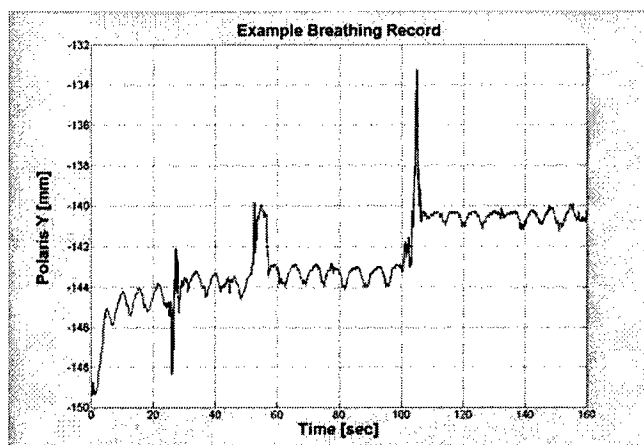


Fig. 5. Respiratory motion from skin recorded by Polaris optical tracking system. Short-term periodicity and larger, intermittent jumps in the position are both evident in this recording.

## V. REFERENCES

[1] T. Zhou, J. Tang, S. Dieterich, K. Cleary, "A robotic 3-D motion simulator for enhanced accuracy in CyberKnife stereotactic radiosurgery," published in *Computer Assisted Radiology and Surgery 2004: Proceedings of the 18th International Congress and Exhibition.*

[2] M.A. Clifford, F. Banovac, E. Levy, K. Cleary, "Assessment of hepatic motion secondary to respiration for computer assisted interventions," *Computer Aided Surgery* 7(5):291-9, 2002.

[3] H. Shirato, Y. Seppenwoolde, K. Kitamura, R. Onimura, S. Shimizu, "Intrafractional tumor motion: Lung and liver," *Seminars in Radiation Oncology* 14(1):10-8, January 2004.

[4] K.H. Wong, J. Tang, S. Dieterich, T. Zhou, K. Cleary, "Applications of a programmable respiratory motion simulator for PET and SPECT," presented at the Annual Meeting of the Society of Nuclear Medicine, Philadelphia, PA, 2004.

[5] S. Dieterich, J. Tang, J. Rodgers, K. Cleary, "Skin respiratory motion tracking for stereotactic radiosurgery using the Cyberknife." *Computer Assisted Radiology and Surgery 2003: Proceedings of the 17th*

presented in Computer Assisted Radiology and Surgery (CARS) 2004

# MRI for modeling of liver and skin respiratory motion

K.H. Wong[a,*], J.W. VanMeter[b], S.T Fricke[b],

C.R. Maurer Jr.[c], K. Cleary[a]

[a]*Imaging Science and Information Systems (ISIS) Center, Department of Radiology, Georgetown University*
[b]*Center for Functional and Molecular Imaging, Department of Neuroscience, Georgetown University*
[c]*Image Guidance Laboratories, Department of Neurosurgery, Stanford University School of Medicine*

...

**Abstract.** The motion of internal organ targets represents a major challenge for image-guided therapy. However, in many clinical situations, the internal organ motion cannot be observed directly, so it is necessary to find a surrogate signal that is both easily observable in the therapy setting and predictive of internal organ motion. We are therefore studying the relationship between skin motion and internal organ motion using dynamic magnetic resonance imaging (MRI), in order to determine the feasibility of using an MRI-based model to perform respiratory motion compensation in image-guided therapies. In this paper, we report (1) testing of different dynamic MRI pulse sequences and which ones appear most suitable for respiratory motion modeling, and (2) results from quantitative analysis of skin and liver motion. This study will provide the groundwork for future experiments that will directly test the validity of using skin motion to predict complex internal target motions.

*Keywords:* Magnetic Resonance Imaging; motion tracking; respiration; image-guided therapy

## 1. Introduction

Modern interventional radiology techniques, coupled with advanced therapeutic methods (e.g. radiofrequency ablation, high frequency ultrasound) have enabled a new generation of image-guided therapies. Similarly, the advent of intensity modulated radiotherapy (IMRT) and highly adaptable radiosurgery accelerators such as the Cyberknife® (Accuray, Sunnyvale, CA) have increased the accuracy and precision of radiation medicine treatments. A crucial challenge for future image-guided interventions is the ability to either monitor or predict the position of internal organ targets during a procedure. This ability is especially important for procedures in the thorax and abdomen, where respiration creates significant involuntary organ motion.

---

*
Corresponding author. *E-mail address:* wong@isis.imac.georgetown.edu.

In an ideal situation, one would monitor the internal organ target directly and steer the therapy based on that data. Although some technologies such as fluoroscopy or interventional MRI allow for the direct monitoring of internal targets during therapy, these technologies are not feasible for every image-guided procedure and also have significant disadvantages. For example, fluoroscopy is typically limited to two-dimensional projections, and necessitates lengthy exposures to ionizing radiation. Interventional MRI requires an extensive infrastructure of highly specialized and costly equipment and cannot be implemented in a radiotherapy environment because of magnetic and radiofrequency interference. Thus, since our ability to directly observe the internal target is limited, we must instead develop methods for predicting its position.

Skin motion is mechanically linked to the movement of the underlying rib cage, diaphragm, and abdominal muscles, and thus it should in principle be related to the motion of the organs in the torso. Existing studies of this relationship using fiducial markers and fluoroscopy have shown encouraging results [1-2]. Furthermore, skin motion can be readily monitored using mechanical devices (e.g. bellows, stretch transducers) or optical/infrared tracking cameras such as the Polaris® (Northern Digital, Waterloo, Canada) system. For these reasons, our laboratory is developing methods for measuring, analyzing, and simulating respiratory-induced skin and organ motion, with a focus on applications in interventional radiology and Cyberknife radiosurgical therapies. This particular project focuses on developing suitable dynamic MRI techniques for imaging/modeling the simultaneous respiratory motion of the liver and the skin surface. Ultimately, we plan to use these data to determine if a surrogate signal -- motion of the skin -- can be predictive of internal target motion.

## 2. Methods

Volunteers for the study were recruited under an IRB-approved human subjects protocol. This protocol recruited only normal patients with no history of liver disease, since we were focusing on the liver as the internal organ of interest. Volunteers were scanned in either a 1.5T General Electric MRI system in the Department of Radiology at Georgetown University Hospital/Medstar Health or a 3T Siemens MRI system at the Georgetown University Center for Functional and Molecular Imaging. Patients were positioned on the imaging table and a respiratory bellows was placed around their thorax or abdomen to monitor their breathing. The 1.5 T system used a surface coil as the receiver, whereas the 3T system used the general-purpose body coil as the receiver since no surface coils were available.

We tested four potential MR pulse sequences: (a) T1 weighted in- and out-of-phase images, (b) T2 weighted half-Fourier single shot turbo spin-echo (HASTE), (c) T2/T1 weighted fast imaging with steady-state precession (trueFISP), and (d) 3D fast-acquisition multi-echo (FAME).

Breath-hold coronal and axial images were acquired at end-inspiration and end-expiration using both T1 and T2 weighted sequences. Once the breath-hold images were completed, coronal and axial images were acquired under free breathing, again using both T1 and T2 weighted sequences. For some patients, we tested prospective respiratory gating based on the respiratory bellows to ensure that the images were derived from known points in the respiratory cycle. We also tested prospective

respiratory gating using navigator pulses centered on the liver-right lung border. The navigator pulse is essentially a very fast 1D MRI image along the inferior-superior axis; it determines the respiratory phase by monitoring the movement of the diaphragm.

Images from the different MRI pulse sequences were evaluated subjectively for noise, contrast, and the presence of motion artefacts. Although the goal of the MRI study is not to produce images for disease diagnosis, the images should still have sufficient detail to make out organ borders, the skin surface, and key internal structures.

Breath-hold and prospectively gated images were analyzed by a semi-automatic routine for extracting the outline of the skin from each axial slice and then combining these outlines into a surface map. The outline of the liver was obtained through manual segmentation to create a volume. The liver position and orientation were compared between end-inspiration and end-expiration, and changes in the skin position were also measured.

The non-gated images acquired under free breathing (trueFISP) were first pre-processed to sort the files according to their acquisition time, so that we could bin the slices into their approximate location in the respiratory cycle. This binning generated 4-6 image sets reflecting the anatomy at different time points. Analysis of these images then proceeded as with the breath-hold images.

## 3. Results

For breath-hold images, the T1 weighted in/out-of-phase images generally produced the clearest contrast of internal organ boundaries since this pulse sequence is specifically designed to accentuate soft tissue borders. However, attempting this sequence under free breathing produced significant motion artefacts. The 3D FAME sequence provides more isotropic spatial resolution than the other sequences, but it was also severely affected by respiratory motion blurring since it required phase encoding in two directions.

The T2 weighted HASTE and the T2/T1 weighted trueFISP sequence could both be applied under free breathing. Respiratory gating was not available for the trueFISP sequence, so these images were rebinned manually. For the T2 weighted HASTE sequence, prospectively gated images using navigator pulses had very similar image quality to those taken with breath holding, and the protocol was much easier on the patients. Sample T2 weighted HASTE images are shown in Figure 1.
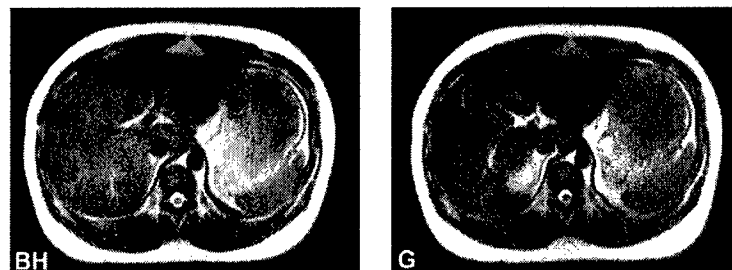


Fig. 1. Comparison of T2 weighted HASTE images. Image on the left is acquired during a breath hold, whereas the image on the right is acquired using navigator gating during free breathing.

Images from the trueFISP sequence produced good soft tissue contrast and were generally less noisy than the HASTE images. Sample T2/T1 weighted trueFISP images are shown in Figure 2.
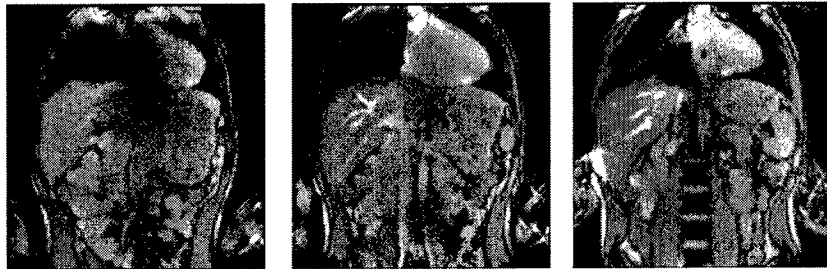
Fig. 2. Coronal T2/T1 weighted trueFISP images of the liver (different coronal planes) acquired during free breathing. Respiratory gating was not available with the trueFISP sequence, so the images were acquired at subsecond time intervals and then manually binned into different points of the respiratory cycle.

The breath-hold images are useful because they show the maximum range of internal organ motion and thereby provide a "baseline" for comparison against the images taken during normal breathing. However, the range of motion seen between end-inspiration and end-expiration tends to be larger than that seen under normal breathing, since patients usually inhale quite deeply before the breath hold. Conversely, prospective respiratory gating is much less difficult for the research subjects, but also is less of a 'snapshot' of the anatomy because each slice is acquired during a separate respiratory cycle. This lengthens the total imaging time and also can create slice mismatches if the anatomy does not return to the exact same position during each breathing cycle.

The semi-automated routine developed for determining the outline of the skin is illustrated in Figure 3. Rays are drawn on axial slices, and the skin surface is identified by detecting large changes in the pixel value along the raypath. The ensemble of these points outlines the skin surface on that slice, and these outlines are then combined to form a surface map of the skin.
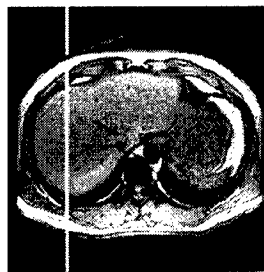
Fig. 3: Illustration of semi-automated method for detecting skin surface, showing an anterior-posterior raypath across the image and the intersection of the raypath and the skin surface.

This method was generally reliable, and only required manual editing for about 1-2% of the detected skin surface points.

Manual segmentation of the liver was generally straightforward, although occasional guidance from a radiologist was helpful when the border became indistinct. A sample liver volume is shown in Figure 4.
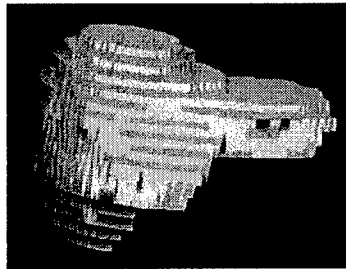


Fig. 4. Surface rendered model of the liver derived from manually segmented MRI data.

Movement of the skin varied depending on the individual and the anatomical location, and ranged between 0 and 1.6 cm. Liver motion was most significant in the cranio-caudal direction; displacements as large as 4.4 cm were observed in breath-hold images, whereas under free breathing the largest displacement was 3.2 cm.

## 4. Discussion

MRI can be a valuable tool for exploring the respiratory-induced movement of organs and skin. Because no ionizing radiation is used, it is possible to perform this study on volunteers with very low risk and to image them over many respiratory cycles, which is essential for testing the repeatability and reliability of matching skin motion to internal organ motion. Specific absorption rate (SAR) limitations are naturally an important concern, especially when imaging in a 3T magnet, but can often be addressed by changing the parameters of the pulse sequence, such as the flip angle.

This study extends the results of previous MRI studies of liver motion secondary to respiration. Rohlfing et al. [3] investigated liver motion modeling using MRI imaging with prospective gating, but found that the gating created impractically long imaging times. Conversely, Blackall [4] employed a protocol where volunteers were asked to hold their breath at different points in the respiratory cycle (e.g. end-inspiration, end-expiration, midway through the cycle, etc.) but reported that patients could not reliably hold their breath at arbitrary points in mid-cycle; the majority of the breath holds were very similar to end-exhalation. Neither approach was therefore optimal. However, since our ultimate goal is to track and treat a moving internal target while the patient breathes, the gating approach is more reflective of the clinical task. Fortunately, current state-of-the-art MRI technology has enabled significant decreases in the imaging time, so that a single prospectively gated set of MRI images can be acquired in less than three minutes.

Nevertheless, there are areas for potential improvement in the future. The first is that the 2D MRI sequences image only one slice at a time, so even if the slices can be read

out in rapid succession, they are not truly simultaneous in the way that slices from a multirow CT scan would be. However, the advent of multichannel receiver coils and parallel imaging techniques should help to address this issue. We expect to install an eight-channel torso coil in the very near future, which should improve both speed and image quality.

The second potential area for improvement is in the gating. Although the prospective gating works well, a more efficient use of the imaging time would be to record the respiratory phase (either with respiratory bellows or continuous navigator imaging) during trueFISP imaging and use those data to retrospectively gate the images to different parts of the respiratory cycle. The current software does not allow us to separately record the raw data from the respiratory bellows or to continuously record navigator images, but we hope to develop such techniques during the coming months. We are also investigating the potential for retrospectively gated 3D MRI sequences.

## 5. Conclusion

MRI is a very useful tool for simultaneously observing skin and internal organ motion. We have tested several different imaging sequences, identified ones that will be well-suited to the task of modeling liver motion, and developed methods for quantitative analysis of the MRI images. In the next phase of this project, we will examine the relationship between skin motion and liver motion in greater detail, in order to test the hypothesis that the skin motion can be used to predict the motion of internal targets, thereby allowing us to track and treat them effectively.

## Acknowledgements

## References

[1] Schweikard A, Glosser G, Bodduluri M, Murphy MJ, Adler JR. Robotic motion compensation for respiratory movement during radiosurgery. Comput Aided Surg 2000; 5(4), 263-277.
[2] Ozhasoglu C, Murphy MJ. Issues in respiratory Motion Compensation during External Beam Radiotherapy. Int. J. Radiation Oncology Biol. Phys. 2002; 52(5):1389-1399.
[3] Rohlfing T, Maurer Jr CR, O'Dell WG, Zhong J. Modeling liver motion and deformation during the respiratory cycle using intensity-based nonrigid registration of gated MR images. Medical Physics 2004; 31(3), 427-432.
[4] Blackall, JM. Respiratory Motion in Image-Guided Interventions of the Liver. Doctoral Thesis, King's College, London, 2002.
[5] Clifford MA, Banovac F, Levy E, Cleary K. Assessment of hepatic motion secondary to respiration for computer assisted interventions. Comput Aided Surg 2002; 7(5), 291-299.

# Electromagnetically tracked guidewires for interventional procedures

Bradford J. Wood [a,*], Dave Lindisch[b], Sohan Ranjan[b], Neil Glossop[c],
Kevin Cleary[b]

[a]*Clinical Center, National Institutes of Health, Bethesda, MD, USA*
[b]*Imaging Science and Information Systems Center, Department of Radiology,*
*Georgetown University Medical Center, Washington, DC, USA*
[c]*Traxtal Technologies, LLC, Bellaire, TX, USA*

## 1. Introduction

We have prototyped and tested an electromagnetically tracked guidewire for interventional procedures. Electromagnetic tracking of instruments in the interventional suite enables image overlay of preoperative CT scans and provides multimodality guidance while decreasing x-ray dose. An electromagnetically tracked guidewire was manipulated in a swine model with co-display of CT and angiographic images.

## 2. Methods and Results

To evaluate electromagnetic tracking (AURORA™, Northern Digital, Inc.) in the interventional suite, we developed an image-guided surgery system. The system was developed using open source software components including FLTK for the user interface, VTK for visualization, and ITK for image processing.

The study was done under an approved animal care protocol. An enhanced CT scan of a swine chest and abdomen was obtained. A rigid body registration was carried out by identifying the points on the CT scan and in electromagnetic space. The guidewire was then initially moved in free air over the abdominal area of the swine to verify that the registration software was working and that is could be tracked.

The internal jugular vein and right carotid artery were percutaneously accessed using ultrasound guidance and modified Seldinger technique with a 21 gauge needle and an .018 inch guidewire. As the guidewire was advanced down the aorta, the corresponding axial CT scan was displayed simultaneously with the real-time angiographic x-ray image. The system provided good qualitative agreement in the opinion of the experienced interventional radiologist manipulating the guidewire. As the guidewire was advanced into the selected vessel, the image-guided system was able to actively track the guidewire and display axial, coronal, and sagittal CT scans at the same level, using the electromagnetically tracked sensor position to select the slice location.

## Acknowledgements

---

*
Corresponding author. *E-mail address*: cleary@georgetown.edu

published in Computer Assisted Radiology and Surgery (CARS) 2004

# A robotic 3-D motion simulator for enhanced accuracy in CyberKnife stereotactic radiosurgery

T. Zhou[a,*], J. Tang[a], S. Dieterich[b], and K. Cleary[a]

[a]*Imaging Science and Information Systems (ISIS) Center, Department of Radiology, Georgetown University, 2115 Wisconsin Ave. NW, Suite 603, Washington, DC, USA 20057*
[b]*Georgetown University Hospital, 3800 Reservoir Road NW, Washington, DC, USA 20007*

**Abstract.** The purpose of this study was to develop a respiratory motion simulator and evaluate its accuracy. The simulator is intended for use in the CyberKnife radiosurgery suite for phantom treatments, dose verifications, and future technical developments. CyberKnife is a radiation treatment system that incorporates a robotic arm to precisely position a linear accelerator. For enhanced accuracy in the treatments of a tumor in an internal organ that is subject to a patient's respiratory motion, the CyberKnife robot must be commanded to move the radiation beam in real-time to compensate for such motion. The motion simulator described in this study was specifically developed to serve the CyberKnife technical requirements for better treatment accuracies. The motion simulator consists of two platforms that may be programmed independently to reproduce different three-dimensional respiratory motions at both the skin over the patient's abdomen and at the internal tumor site. The simulator meets the spatial restrictions of the CyberKnife suite with a position accuracy better than ±0.1 mm.

*Keywords:* respiratory motion, robotic motion simulator, stereotactic radiosurgery, CyberKnife

## 1. Introduction

The CyberKnife® stereotactic radiosurgery system (Accuray, Inc.) incorporates a 6 MeV linear accelerator mounted on a robotic arm to deliver multiple crossfire beams of radiation to destroy a lesion while sparing surrounding healthy tissue and critical structures [1, 2]. In addition, this system can correct for patient movement during treatment through the use of skeletal landmarks or small implanted fiducials. In August 2001, CyberKnife was cleared by the Food and Drug Administration for tumor treatments anywhere in the body, and since that date, thousands of treatments have been completed successfully.

About 85% of current CyberKnife treatments are for brain and spine tumors, which do not move significantly with patients' respiration. However, for many internal organs, respiratory motion does cause significant movement of the tumors, such as lung tumors as reported in [3]. To address this issue, Accuray developed the Synchrony technology with the goal of compensating for tumor motion due to respiration.

---

*
Corresponding author. *E-mail address:* tong.zhou@utoronto.ca.

With Synchrony, a correlation model between the skin motion and a given internal organ motion is established by simultaneously taking x-ray images to track internal fiducials and using infrared trackers attached to the skin. This correlation model is established and verified during treatment. The CyberKnife robot follows the internal organ motion based on the prediction from the skin motion [4]. To quantify and validate this technology, a programmable respiratory motion simulator is required. The simulator must precisely simulate the three-dimensional respiratory motion at both the skin on the patient's abdomen and at the tumor site in the internal organ. This paper presents our simulator design and initial accuracy experiments.

Figure 1 shows the CyberKnife Suite in the Department of Radiation Medicine at Georgetown University Hospital. The robot arm has a full six degrees of freedom. Two orthogonal x-ray cameras with corresponding amorphous silicon detectors allow on-line verification of the patient's position for necessary correction. A fixed theoretical point, named iso-center, is located in the middle of the cross section of the two x-ray beams. During treatment, the targeted tumor is located at the iso-center through which all the radiation treatment beams pass. Figure 1(c) shows this center represented by the tip of a calibration post.



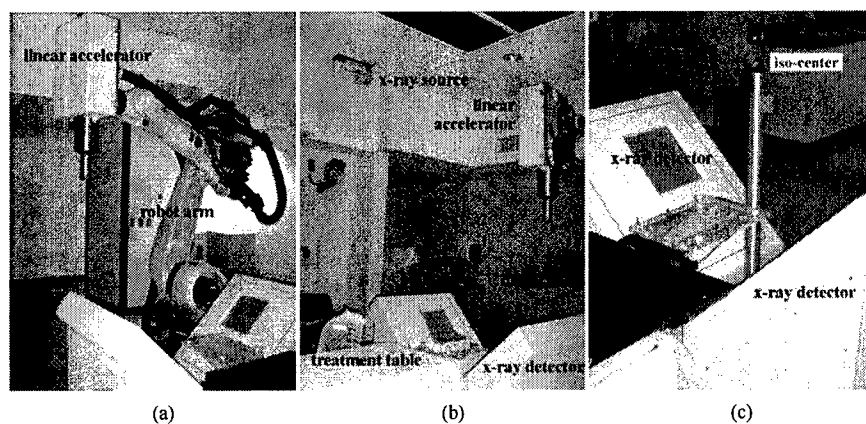|         (a)          |          (b)           |         (c)          |

Fig. 1. CyberKnife Suite at Georgetown University Hospital

## 2. Methods

The respiratory motion simulator (RMS) consists of two independent, programmable robotic three-dimensional (3-D) motion platforms. The platforms are called a Skin-Motion Simulator (SMS) and a Tumor-Motion Simulator (TMS). The RMS was built completely with off-the-shelf components. Wiring, assembly and software development were completed in-house at Georgetown University Medical Center. The components were selected based on the technical requirements of motion amplitude and frequency, which were established from real patient data taken at Georgetown University Hospital (SMS) [5] and published data (TMS) [3]. External loads, as well as the weight of the components themselves, were also considered in the motor calculation.

The SMS consists of three high-precision orthogonally-mounted linear slides (Velmex, Inc.), and the TMS consists of two such linear slides and one vertically-mounted linear piston actuator (Ultra Motion, LLC). Each stage includes a high-performance servo motor, an integrated gearhead at the motor output shaft, and an optical rotary encoder mounted on the motor back shaft (Maxon Precision Motors, Inc.). The platforms are controlled by a PC through an Ethernet-addressable motion control board (Galil Motion Control, Inc.) that utilizes feedback from the encoders.

A major challenge in designing the simulator was the unique geometry requirements of the CyberKnife system. As mentioned in Section 1, the CyberKnife uses two orthogonal x-ray beams to track internal fiducials. Therefore, only radio-lucent materials (i.e., non-metallic materials) may present in the paths of these x-ray beams. This no-metal zone limits the size of slides and motors that may be used. In addition, the iso-center is located directly in the middle of this no-metal zone where phantoms or film box for dose verification must be located. Considerations must also be taken to ensure collision-free movements between the CyberKnife robot and the simulator, as well as between the two platforms. To correctly select and design the components of the simulator, a 3-D computer-aided design (CAD) method was adopted using the software Alibre Design (Alibre, Inc.). Figure 2 shows the design results from a CAD model, and the actual simulator in the CyberKnife Suite.
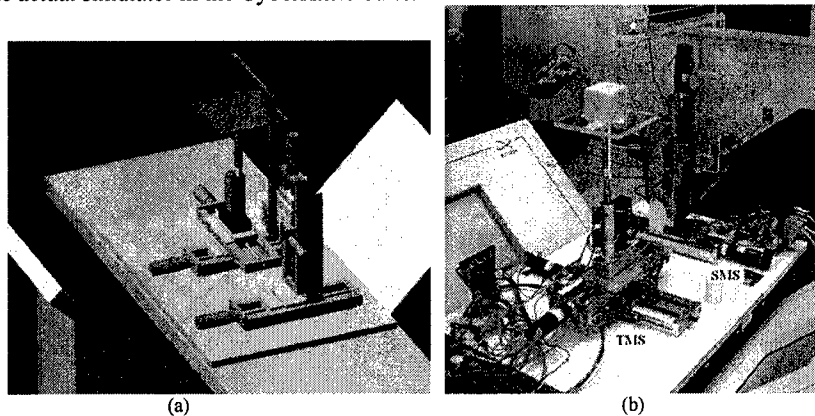


(a)                                                    (b)

Fig. 2. Respiratory Motion Simulator

## 3. In-situ verification and accuracy tests

After assembly, the simulator was tested to verify its capability at in-situ condition as well as its accuracy in reproducing both sinusoidal waves and human respiratory motions. The accuracy tests were conducted in the Computer Integrated Surgical Systems and Technology (CISST) Lab at Johns Hopkins University using an Optotrak to evaluate the simulated motions. The Optotrak (Northern Digital, Inc.) is an optical high-precision 3-D motion measurement system that can achieve a resolution of 0.01 mm and an accuracy of 0.1 mm (root-mean-square or rms), both at a 2.25 m distance from the object (http://www.ndigital.com/optotrak.html). This is sufficient for the qualification purpose of the simulator since only the relative position movement is concerned.

### 3.1  In-situ tests for dimension and dose verification

The motion simulator was tested in the CyberKnife Suite at Georgetown University Hospital under radiosurgery treatment conditions. The simulator was placed on the treatment table with the electronics placed on the floor about 2 m away from the iso-center to prevent the 6MeV x-ray beams from passing directly through any electronic components (see Figure 2b). The RMS was linked through a 30 m Ethernet cable to a PC outside of the treatment vault. A film cube with two GaFchromic films was placed perpendicularly on the TMS top platform. Six metal fiducial markers in the film cube were used to track its position. The TMS was then moved in sinusoidal motions with 7.5 mm amplitude in the craniocaudal direction and 5 mm in both the anterior-posterior and the left-right directions.

It has been verified that the RMS fits the physical space and no collision will occur between the CyberKnife robot and the RMS, or between the SMS and the TMS. The CyberKnife x-ray image system confirmed that no metal parts interfered with fiducial tracking of the film cube on the TMS platform. Ionizing radiation did not interfere with the operation of the RMS.

The RMS was also used to demonstrate the distortions of the dose distribution in a tumor under uncompensated breathing motion. Three treatments with a maximum dose of 3000 cGy were delivered. For the first treatment, the TMS was not moved, so the ideal dose distribution was obtained (Figure 3a). For the second treatment, the TMS was driven by the sinusoidal motions, but no position corrections were performed. The CyberKnife treatment was applied as if the film block would have remained in the initial position. This dose distribution would simulate an IMRT treatment under free breathing conditions. Treatment two showed an elongated dose distribution in the direction of the largest motion amplitude (Figure 3b). In addition, the peak dose was smeared out. The center of the distribution was also offset, which demonstrated the respiratory motion effect relative to a treatment plan done on a breath-hold CT scan. For the third treatment, two x-ray images were taken before every radiation beam for position correction. This treatment also showed a smeared out dose distribution, but the distribution was more circular than for the second treatment (Figure 3c). It should be noted there is a significant time delay between taking the x-ray images and firing the treatment beams, so position correction based on x-ray images cannot completely compensate the respiratory motion in real time.



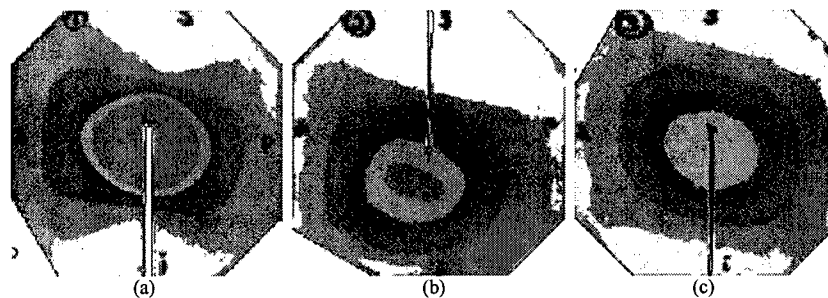(a)                    (b)                    (c)

Fig. 3. Digitized films of radiation dose distribution

### 3.2 Accuracy evaluation tests

To verify the accuracy of the RMS, tests were carried out using the Optotrak, which was placed about 2 m from the simulator. For each test, two sets of data were collected: one set measured the motion at the top stage of the simulator in Optotrak's coordinates, the other measured the commanded motion to each slide in the simulator's coordinates. A registration method was applied to convert the Optotrak results into the simulator's coordinates for comparison. Figure 4 shows the system setup of the accuracy tests.

First, the simulator was driven with sinusoidal waves at individual stages, which resulted in 1-D motions along each axis of the simulator. These sinusoidal waves show a frequency of 0.2 Hz and peak-to-peak amplitudes ranging from 7.5 mm to 15 mm. Next, the simulator was tested with the same waves at all stages simultaneously, thus providing a 3-D motion at the top stage. Finally, a segment of about 60 seconds of real human 3-D respiratory motion recorded at the chest skin was used to drive both the SMS and the TMS. This set of data contains about eight breathing cycles with an average amplitude of 10 mm and one deep breath of 17 mm in total (see Figure 5).
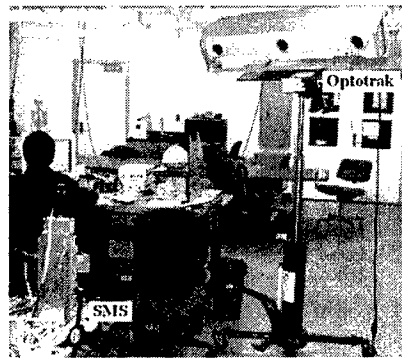
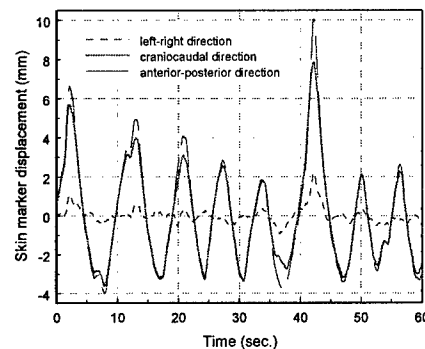

Fig. 4. Test setup for RMS accuracy evaluation



Fig. 5. Human 3-D respiratory motions

The comparisons show that both the SMS and the TMS can achieve an accuracy of ±0.1 mm in simulating both sinusoidal waves and human respiratory motion. This accuracy is a combination of all three axes. For each individual axis, the accuracy is even better, ranging from ±0.03 mm to ±0.08 mm (e.g., Figure 6). Random errors of ±0.02 mm were detected even when the simulators remained motionless. This is due primarily to the resolution of the Optotrak system and possibly to some nearby disturbances that caused slight vibration in the system setup.

It is evident the position error depends heavily on motion amplitude and frequency; that is, larger motion amplitude or higher frequency are predictably correlated with larger position error. Moreover, the total error is normally a superposition of two distinct frequencies – a low frequency part equivalent to the nominal motion frequency, and one or more much higher frequency components that correspond to the natural frequencies of the simulator (see Figure 6a). This is due to dynamic forces during the movement that cause deflection and vibration in the structure. Therefore, structural stiffness should be improved further for better accuracy.
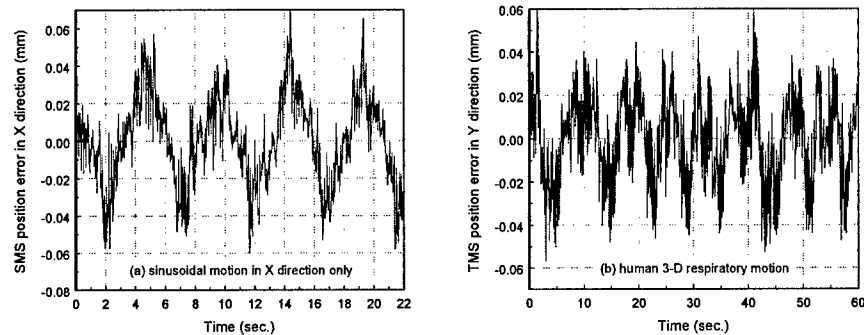
Fig. 6. Sample results of accuracy tests

## 4. Conclusions

In this study, a robotic RMS has been developed. It consists of two platforms, namely SMS and TMS, and both platforms may be programmed independently to simulate different 3-D motions. It has been demonstrated that the RMS is able to reproduce human respiratory skin and tumor motions with a precision better than ±0.1 mm. The RMS fits the physical space and no-metal zone requirements for the CyberKnife Suite. The basic hardware design fulfilled our expectation. Further improvements, e.g., better structural stiffness for less vibration and user-friendly software interface, will be conducted. We anticipate the simulator will be a valuable tool in the CyberKnife Suite for phantom treatments, dose verifications of Synchrony technology and future technical developments.

## Acknowledgments

## References

[1] Adler Jr JR, Murphy MJ, Chang SD, Hancock SL. Image-guided Robotic Radiosurgery. Neurosurgery 1999; 44(6):1299-1307.

[2] Gerszten PC, Ozhasoglu C, Burton SA, et al. CyberKnife frameless single-fraction stereotactic radiosurgery for tumors of the sacrum. Neurosurgical Focus 2003; 15(2):Article 7.

[3] Giraud P, Rycke YD, Dubray B, et al. Conformal radiotherapy planning for lung cancer: Analysis of intrathoracic organ motion during extreme phases of breathing. Int. J. Radiation Oncology Biol. Phys. 2001; 51(4):1081-1092.

[4] Ozhasoglu C, Murphy MJ. Issues in respiratory Motion Compensation during External Beam Radiotherapy. Int. J. Radiation Oncology Biol. Phys. 2002; 52(5):1389-1399.

[5] Dieterich S, Tang J, Rodgers J, Cleary K. Skin respiratory motion tracking for stereotactic radiosurgery using the CyberKnife. In: Lemke HU, Vannier MW, Inamura K, Farman AG, Doi K, Reiber JHC, editors. Proceedings of CARS 2003. Amsterdam: Elsevier Publisher, 2003, 130-136.